



Title	Structure-function relationship of ice-binding proteins from cold-adapted organisms
Author(s)	山内, 彩加林
Citation	北海道大学. 博士(生命科学) 甲第14664号
Issue Date	2021-09-24
DOI	10.14943/doctoral.k14664
Doc URL	http://hdl.handle.net/2115/83599
Type	theses (doctoral)
File Information	Akari_Yamauchi.pdf



[Instructions for use](#)

Structure-function relationship of ice-binding proteins from cold-adapted organisms

(低温適応生物由来氷結晶結合蛋白質の構造機能相関)

by

Akari Yamauchi

A thesis submitted to the Division of Life Science,

Graduate School of Life Science, Hokkaido University

In conformity with the requirement for the degree of Doctor of Philosophy

Hokkaido University

Sapporo, Hokkaido, Japan

(September, 2021)

Copyright © Akari Yamauchi, 2021

CONTENTS

List of abbreviations	3
Chapter 1: General introduction	6
1.1. Organism in cold environments	7
1.2. Ice-binding proteins (IBPs)	7
1.3. Water freezing	8
1.4. Ice crystal	8
1.5. Determination of IBP-bound ice planes	11
1.6. Ice-shaping properties of IBPs	13
1.7. Function of IBPs	13
1.8. Physiological function	18
1.9. Structures of IBPs	21
1.10. Ice-binding mechanism of IBPs	30
1.11. Purpose and scope of this dissertation	31
Chapter 2: Elucidation of ice-binding mechanism of microbial <i>AnpIBP</i>	33
2.1. Abstract	34
2.2. Introduction	35
2.3. Materials and methods	39
2.4. Results and Discussion	45
Chapter 3: Discovery of hyperactive IBP from <i>Dourcus hopei binodulosus</i>	63
3.1. Abstract	64
3.2. Introduction	65
3.3. Materials and methods	70
3.4. Results and Discussion	76
Chapter 4: General discussion	97
4.1. Summary in this study	98
4.2. Ice-binding mechanism of moderately active <i>AnpIBP</i> vs hyperactive <i>DhbIBP</i>	99
4.3. Difference of antifreeze activities of <i>AnpIBP</i> and <i>DhbIBP</i>	101
4.4. Evolutionary mechanism of <i>AnpIBP</i> and <i>DhbIBP</i>	101
4.5. Conclusions	104

References	105
Acknowledgements	120

LIST OF ABBREVIATIONS

ACW	anchored clathrate water
Adap	adaptor
AFP	antifreeze protein
AFGP	antifreeze glycoprotein
AnpIBP	IBP from <i>Antarctomyces psychrotrophicus</i>
bp	base pairs
BW	bound water
CCD	charge coupled device
CD	circular dichroism
cDNA	complementary DNA
ColIBP	IBP from <i>Colwellia</i> sp. strain SLW05
CfIBP (SbwIBP)	IBP from spruce budworm, <i>Choristoneura fumiferana</i>
DcIBP (DIBP)	IBP from <i>Daucus carota</i>
DcIBP (DIBP)	IBP from <i>Dendroides canadensis</i>
DEPC	diethylpyrocarbonate
Dhb	<i>Dorcus hopei binodulosus</i>
DhbIBP	IBP from <i>Dorcus hopei binodulosus</i>
DNA	deoxyribonucleic acid
Drr	<i>Dorcus rectus rectus</i>
DrrIBP	IBP from <i>Dorcus rectus rectus</i>
DUF	domain of unknown function
E.coli	<i>Escherichia coli</i>
EfcIBP	IBP from <i>Euplotes focardii</i> bacterial consortium
FIPA	fluorescence-based ice plane affinity
FfIBP	IBP from <i>Flavobacterium frigoris</i> PS1.
GrIBP	IBP from <i>Granisotoma rainieri</i>
HGT	horizontal gene transfer
IBP	ice-binding protein
Ih	unit structure of a single ice crystal at 1 atmosphere
IBP	ice-binding protein
IBPv	IBP from a bacterium within the family <i>Flavobacteriaceae</i> (isolate3519-10) in the Vostok Ice Core
IBS	ice-binding site

IRI	ice recrystallization inhibition
IwIBP	IBP from inchworm, <i>Campaea perlata</i>
LpIBP	IBP from <i>Lolium perenne</i>
LpIBP	IBP from longsnout poacher, <i>Brachyosis rostratus</i>
LeIBP	IBP from <i>Leucosporidium</i> sp. AY30
LB	lysogeny broth/luria-bertani
LN ₂	liquid nitrogen
MpIBP	IBP from <i>Marinomonas primoryensis</i>
mRNA	messenger RNA
mtDNA	mitochondrial DNA
Mw	molecular weight
NCBI	national center for biotechnology information
NfeIBP	type III IBP from notched-fin eelpout, <i>Zoarces elongatus Kner</i>
OD	optical density
PCR	polymerase chain reaction
PDB	protein data bank
pI	isoelectric point
Poly (A)	poly adenine
<i>P. pastoris</i>	<i>Pichia pastoris</i>
PPII	poly-proline type II
PVC	polyvinyl chloride
rDhbIBP	recombinant <i>DhbIBP</i>
RiIBP	IBP from <i>Rhagium inquisitor</i>
RNA	ribonucleic acid
RNase	ribonuclease
rRNA	ribosomal RNA
SDS-PAGE	sodium dodecyl sulfate-polyacrylamide gel electrophoresis
SfiIBP	IBP from snow flea, <i>Hypogastrura harveyi</i>
SfiIBP	IBP from <i>Shewanella frigidimarina</i>
ss-cDNA	single strand cDNA
TH	thermal hysteresis
THP	thermal hysteresis protein
TisIBP	IBP from <i>Typhula ishikariensis</i>
Tf	freezing point
Tm	melting point
Tm	<i>Tenebrio molitor</i>

TmIBP	IBP from <i>Tenebrio molitor</i>
Tris	tris(hydroxymethyl)aminomethane
Trx	thioredoxin
UTR	untranslated region
UV	ultraviolet
WfIBP	IBP from winter flounder, <i>Pseudopleuronectes americanus</i>

Chapter 1: General introduction

1.1. Organisms in cold environments

Approximately 70% of a surface area of earth is occupied by waters. Most of biosphere of the earth, approximately 80% of biosphere, exposed to temperature below 5°C [1,2]. Organism living with water needs to overcome the problems caused by winter temperature like nutrient limitation, low fluidity of lipid membrane and high osmotic pressure. In such cold environment, water exists as a frozen state seasonally or constantly. Examples are as follows: sea ice, freshwater ice, snow cover, glaciers, ice sheets and soli ice [3]. Ice formation or complete freezing is known to cause damages to biological system, which leads to disrupt cell structure and denature proteins of organisms. Nevertheless, some organisms are known to tolerate such cold environment [4]. As a molecular adaptation, cold adapted organisms are known to produce some cryoprotectants like salts, glycerol, polyalcohols, sugars, fatty acid, and ice-binding proteins [5–7]. In this study, we focused on ice-binding protein.

1.2. Ice-binding proteins (IBPs)

Ice-binding proteins (IBPs), also called as antifreeze proteins (AFPs) or thermal hysteresis proteins (THPs), are extraordinary macromolecules produced by cold-adapted organisms [4,8]. IBPs inhibit single ice crystal growth through their adsorbing on ice surface, leading to depress the freezing point of water. IBP was first discovered from the blood of Antarctic Notothenioid fishes in 1969 as antifreeze glycoprotein (AFGP) [9]. Until now, other IBPs have been found from various organisms including fish, insects, plants and microorganisms that survive cold environment [4]. IBPs are divided into several types consisting of different amino acid sequence and tertiary structure. IBPs are characterized by ice-binding properties reflecting unique structure (i.e., IBP bound ice planes, ice crystal morphologies, thermal hysteresis activity and ice recrystallization inhibition activity).

1.3. Water freezing

To understand the basic of water freezing is indispensable to consider the function of IBP. When we cooled water, it is not frozen at 0°C or subzero temperature (Figure 1.1.A). Below 0°C, single ice crystals are thought to be generated in water [10,11]. The lower temperature induces more generation of ice crystals and make their size larger. This phenomenon is called supercooling, where the supercooled water seems to undergo no change under photomicroscope. When they reach supersaturation state with further temperature lowering, supercooled water is frozen and general ice crystals are observed. The transition temperature from supercooled water to frozen state (ice) is defined as a freezing point (T_f °C). Since a uniform nucleation needs to be occurred in pure water, water does not freeze until at approximately -40°C. A heterogeneous nucleation occurs in water in the presence of microparticles, substances, dust and fluff, resulting in water freezing at 0°C. General water freezes at 0°C due to the presence of such various ice nuclei around us. IBPs inhibit growth of the single ice crystals generated in supercooled water so that they depress freezing point of water (Figure 1.1.B). IBPs are thought to play a role to stabilize supercooled state.

1.4. Ice crystal

The ligand of IBPs is a single ice crystal. General ice is composed of assembly of single ice crystals. In the unit structure of a single ice crystal, water molecules are systematically organized into a hexagonal arrangement under one atmospheric pressure (Figure 1.2.A). The hexagonal ice (denoted I_h) is created by three equivalent a -axes (a_1 - a_3) perpendicular to the c -axis [12]. The single ice crystal is composed of several ice planes constructed by differently aligned water molecules [13]. Each ice plane is identified by using the Miller-Bravais indices [14,15]. The basal plane lies perpendicular to the c -axis and parallel to the a -axis (Figure 1.2.B),

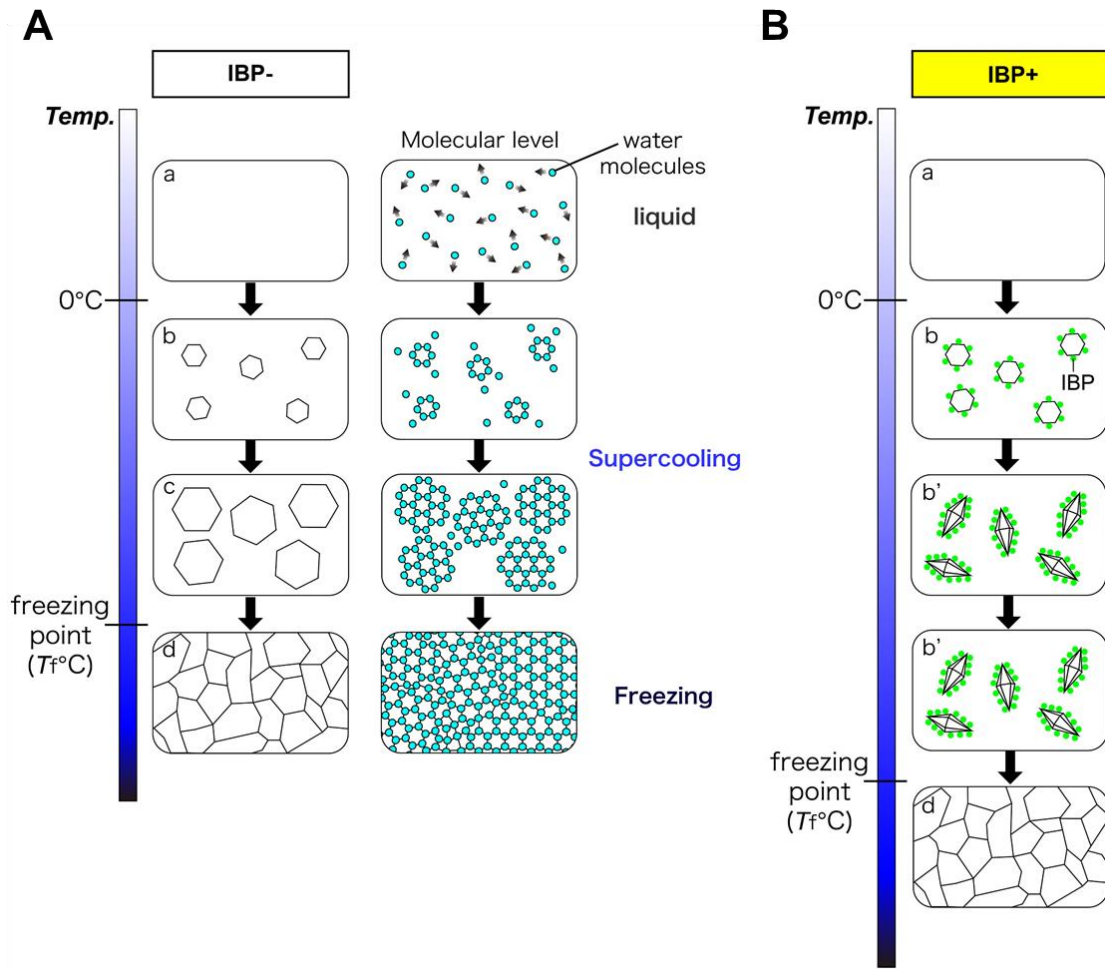


Figure 1.1. Schematic diagram of water freezing.

(A) Illustration of water freezing process in the absence of IBPs. A right column shows image of water freezing (left column) in molecular level. When water (a) is cooled below 0°C , embryo ice crystals are generated in there (b). Embryo ice crystals are more generated and increasing in size depending on cooling (c). When the ice crystals become supersaturated state, water freezing and general ice formation occur (d). Transition temperature from supersaturation state to ice is defined as a freezing point ($T_f^{\circ}\text{C}$). The state of (b) and (c) is called supercooling state. (B) Illustration of water freezing in the presence of IBP. IBPs (green spheres) bind to embryo ice crystals (b) and inhibit their growth (b'). IBPs are thought to stabilize supercooling state of water through maintaining the state (b'), which inhibits the transition from (b') to (d).

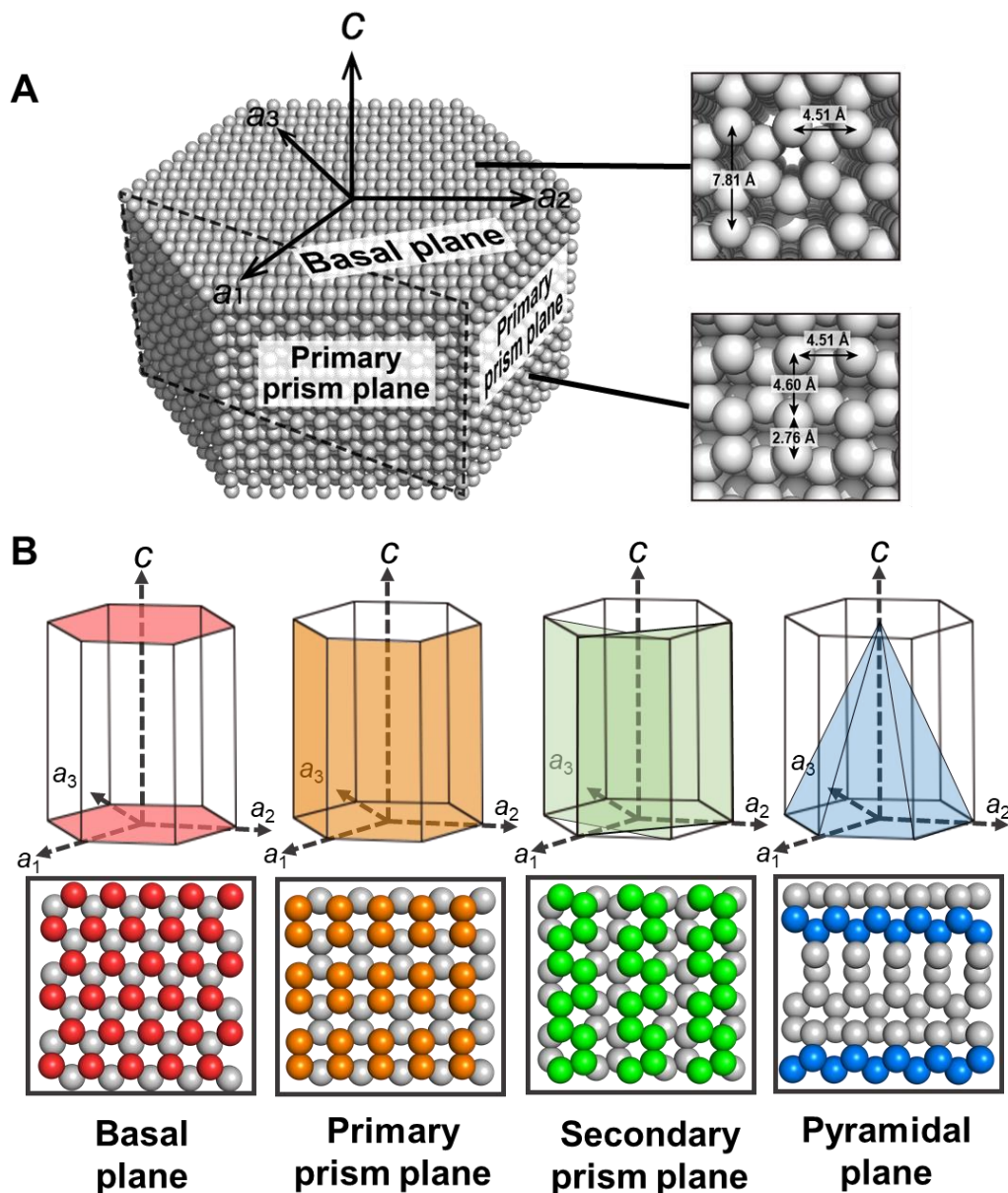


Figure 1.2. Unit structure of a single ice crystal.

(A) Hexagonal unit of single ice crystal (I_h) under one atmospheric pressure. Spheres show oxygen atoms of water molecules. Oxygen atom distances on basal plane (top box) and primary prism plane (bottom box). There are differences of oxygen atom distances on each ice plane. (B) Positions of each ice planes in I_h and whose oxygen atom arrangements are shown in boxes. Illustration indicates basal plane (red), primary prism plane (orange), secondary prism plane (green) and pyramidal plane (blue). The bottom illustrations show oxygen atoms characterized in each ice plane. All structures are created by PyMOL.

which looks like honeycomb structure when viewed from the top. The prism planes lie parallel and perpendicular to the a -axes, respectively. The side planes of the hexagonal ice are primary prism plane, also called as first prism plane along the c -axis. The diagonal plane is secondary prism plane along the c -axis. Other inclined planes between the basal and prism planes are defined as pyramidal planes. A snowflake is an example of a hexagonal single ice crystal.

1.5. Determination of IBP-bound ice planes

IBPs are thought to recognize the spacing between the different oxygen atoms of waters to bind to ice crystal. A handling technique for single ice crystals was first developed by Knight, C.A. *et al.* and denoted ice-etching technique in 1991 [16], which allows us to confirm to which ice planes IBP binds. Recently, the modified method utilizing fluorescence-labeled IBP is developed [17], whose protocol is called fluorescence-based ice plane affinity (FIPA) analysis. For the FIPA analysis, a single ice crystal hemisphere in 3–4 cm diameter is created by utilizing a polyvinyl chloride (PVC) pipe and a cooling bath. We can determine the a - and c -axes of the single ice crystal using a polarizer, where its earth-axis corresponds to the c -axis of I_h . Such an ice hemisphere is mounted on a cold finger with desired orientation (Figure 1.3.A). The single ice hemisphere is soaked into the fluorescence-labeled IBP solution to induce crystal growth (Figure 1.3.B). A FIPA pattern of the IBP appears on the surface of ice hemisphere under ultraviolet (UV) light (Figure 1.3.C) [18]. Based on the illuminated area on the single ice hemisphere, one can correlate the FIPA patterns and the ice planes constructing the hexagonal single ice crystal (Figure 1.3.D). For example, the FIPA pattern observed at the polar region of a single ice crystal hemisphere implies the basal-plane binding of an IBP. When illumination was observed entirely, it suggests whole-plane binding. Since each IBP recognize different ice planes, there are various FIPA patterns [19].

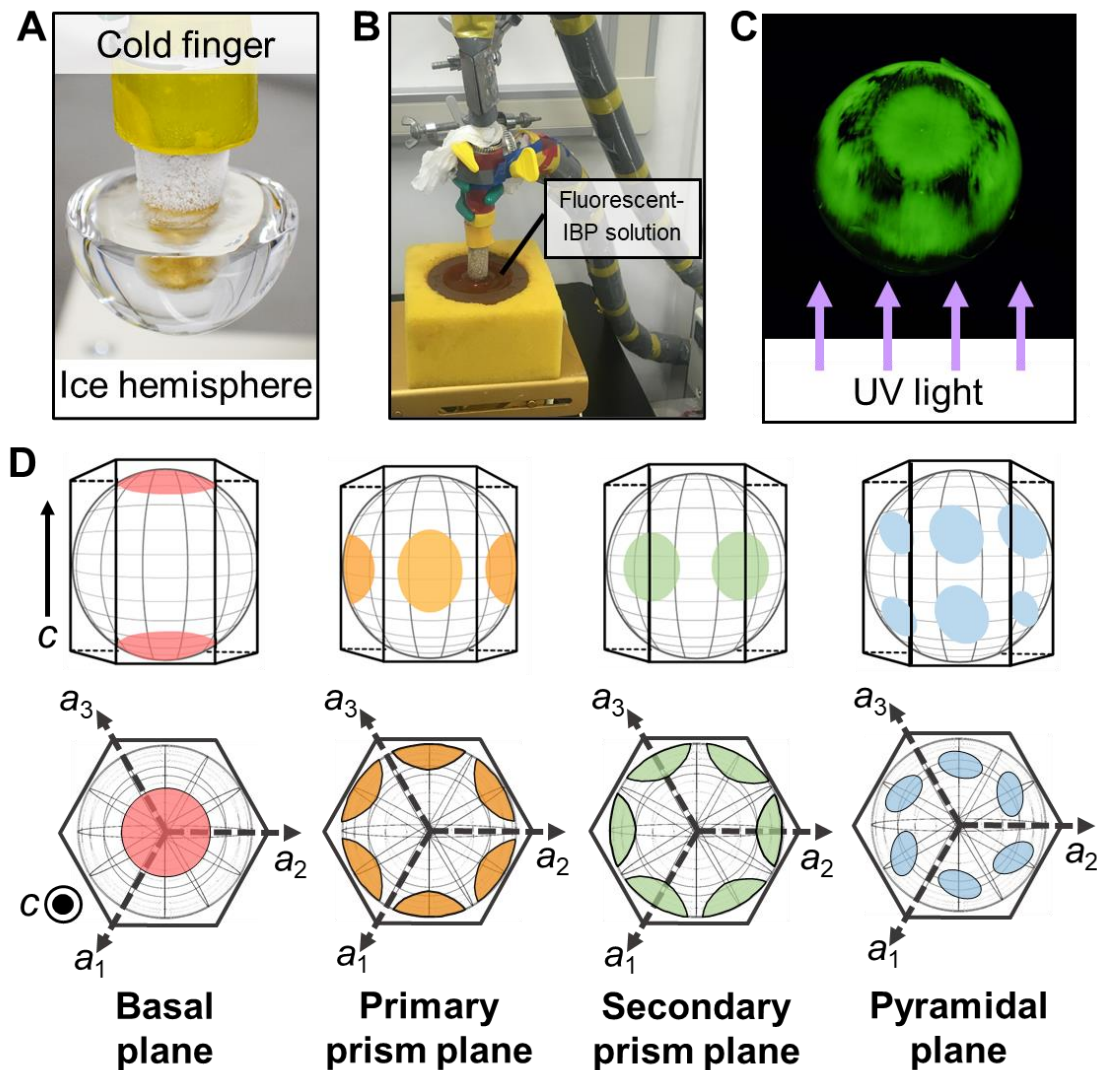


Figure 1.3. Analysis of fluorescence-based ice plane affinity (FIPA).

(A) Photographs of a single ice hemisphere attached onto cold finger. (B) The single ice hemisphere soaked into fluorescent-labelled IBP solution to induce crystal growth. (C) FIPA pattern observed under UV light. (D) Correlation between the FIPA patterns (color patches) and IBP-bound ice planes constructing the hexagonal single ice crystal. When illuminations are observed in polar region of ice hemisphere, it suggests that the IBP binds to basal plane (red). FIPA patterns of six patches indicate that the IBP binds to prism plane (primary prism plane: orange, secondary prism plane: green). The illuminations between polar region and equator regions indicate that the IBP binds to pyramidal plane (blue).

1.6. Ice-shaping properties of IBPs

IBPs modify single ice crystal in shape through its binding. A schematic diagram shows ice-shaping process in absence or presence of IBP (Figure 1.4.A). The single ice crystal is generated in supercooled water, it shows round disk shape under photomicroscope. The reason why the shape is not hexagonal is thought due to energetically stable. The single ice crystal grows approximately 100 times faster toward the a -axis than that toward the c -axis (basal plane) [20]. Thus, the basal plane of single ice crystal grows after the prism planes growing, piled up in the direction of c -axis. In the presence of IBP, it is reported that varieties of single ice crystal morphologies are observed in supercooled water under photomicroscope (Figure 1.4.B) [18,21,22]. IBP modifies ice crystal into a unique shape through its binding to specific ice planes. Upper illustration shows that specific binding type of IBP inhibit only growth from prism plane or pyramidal plane of single ice crystal. When IBPs bind to ice crystal, hexagonal disk-shaped ice crystal is generated. A new disk is formed perpendicular to the c -axis by further binding of IBP to ice plate [23]. IBP constantly modified new disk into a hexagon during cycles that ice crystal grows and new disk generates. As a consequence, bipyramidal ice crystal is constructed in supercooled water [21]. When IBP binds to multiple ice planes including basal plane (Figure 1.4.B, bottom illustration), it shaped into more round lemon-like ice crystal [22].

1.7. Function of IBPs

1.7.1. Thermal hysteresis

IBPs adsorb onto ice plane, leading to depress freezing point of water. In the absence of IBP, the ice crystal grows along with lowering temperature (Figure 1.5.). Their freezing point (T_f) and melting point (T_m) is same temperature. IBPs control ice crystal growth by an adsorption-inhibition mechanism (Figure 1.6.) [8]. When IBPs adsorbed onto ice crystal surface, the interface

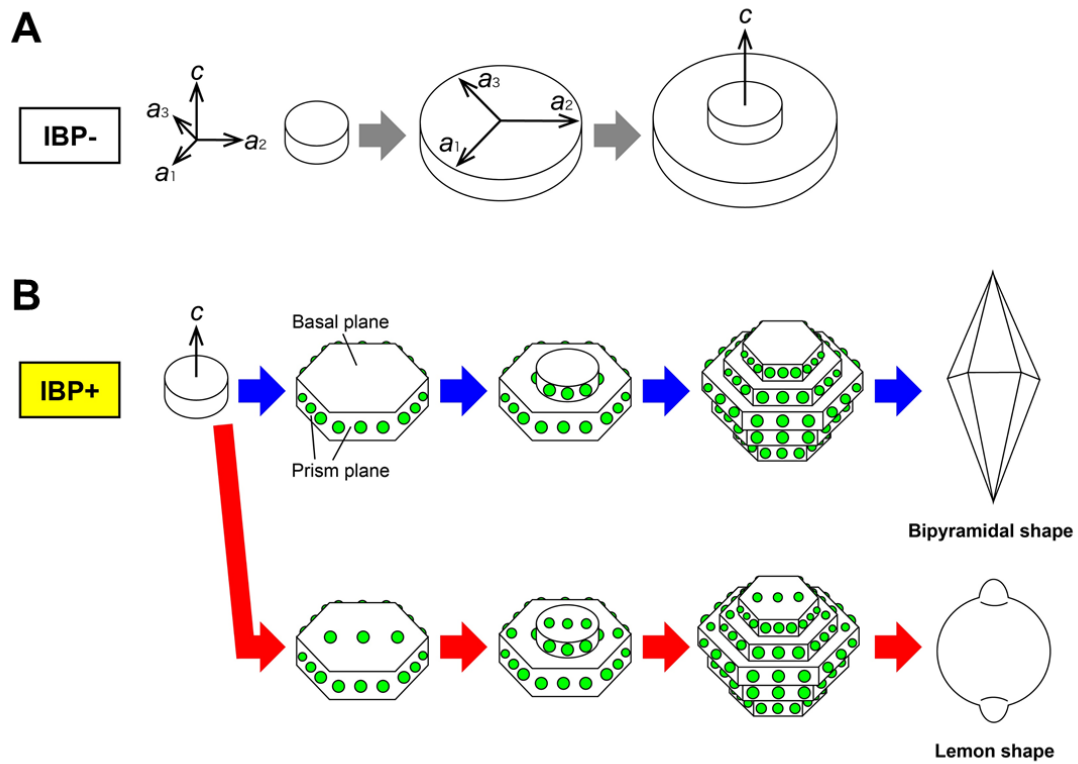


Figure 1.4. Schematic diagram of shaping of single ice crystal.

(A) The ice crystal forms a round disk shape in absence of IBPs under photomicroscope. The single ice crystal first grows toward the a -axis and next do toward the c -axis. (B) Illustration of process of ice-shaping in the presence of IBP. A green sphere shows an IBP. Moderately active IBP binds to prism planes or pyramidal planes (top), and modified ice crystal into hexagonal. Further additions of IBPs generate a new disk on hexagonal plate. Moderately active IBP generates bipyramidal shaped ice crystal. Hyperactive IBP from insect IBP adsorbs onto whole plane including basal plane and shapes ice crystal into lemon-like morphology (bottom).

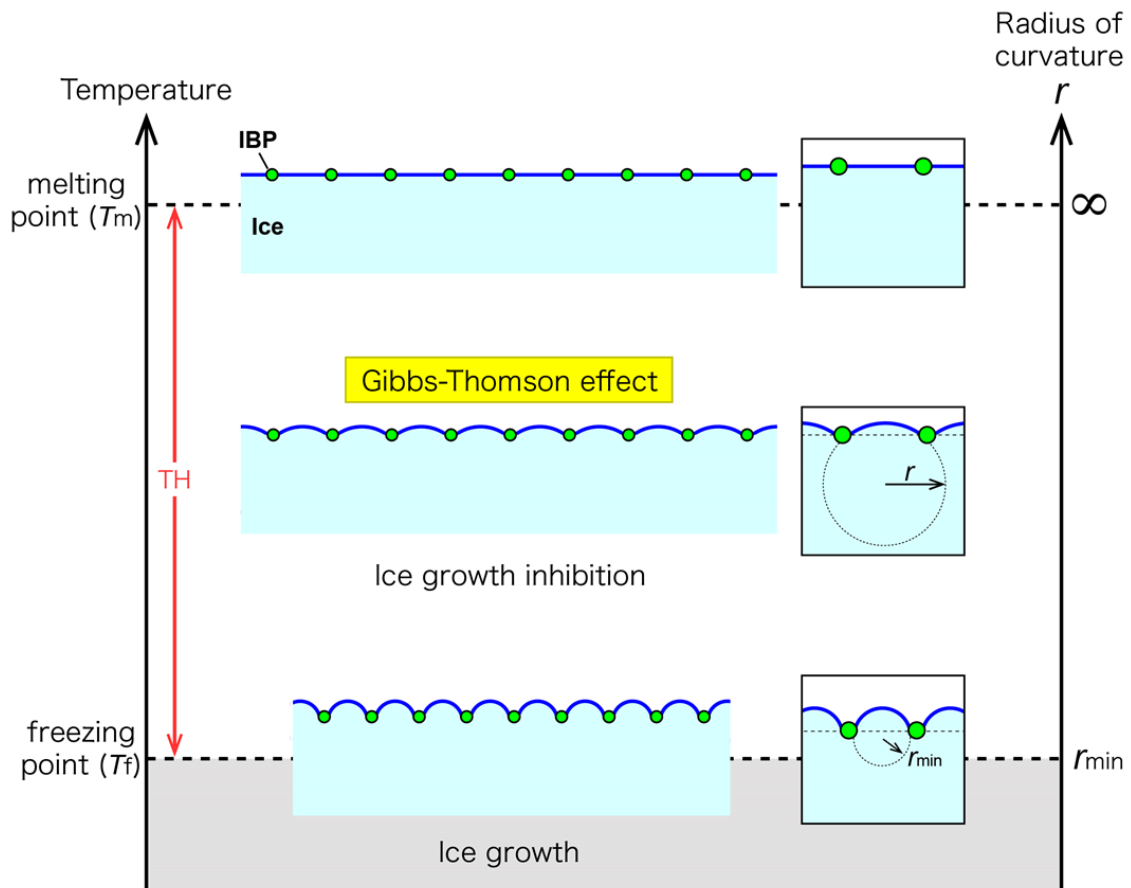


Figure 1.6. Schematic diagram of an adsorption-inhibition mechanism.

IBPs (green spheres) adsorb onto ice at the T_m , where ice-water interface between different IBP molecules is thought to be flat (top). During cooling state, the further ice growth is inhibited depending on radius (r) between IBP molecules, resulting in a depression of the T_f of the solution (middle). This is called as a Gibbs-Thomson effect. When the radius of curvature reaches less than half distance between two IBP molecules, the ice crystal bursting occurs (bottom).

between two adsorbed IBP molecules protrudes in the front and form micro curvature [24]. The water molecules incorporated into the ice-crystal because of local growth being energetically unfavorable (Kelvin effect) [25]. As the growth of ice crystal, the curvature between IBP molecules increases, resulting in a depression of the freezing point (T_f) of the solution (Gibbs-Thomson effect) [16,26,27]. The rapid growth of ice (bursting) occurs when the radius of curvature is less than half distance between two IBPs. This bursting temperature of ice crystal is defined T_f . IBP depress noncolligatively freezing point of the solution and slightly elevate the melting point [22,28,29]. Thermal hysteresis (TH) was the difference between T_f and T_m . TH activity is commonly used as index of antifreeze activity of IBPs [22,28,30,31].

IBPs are classified into two groups, moderately active IBP and hyperactive IBP, depending on its TH activity (Figure 1.5.) [22]. Moderately active IBP is known to bind to only specific ice planes and inhibit growth of ice crystal with modifying into hexagonal bipyramid shaped [18]. Moderately active IBPs show less than 2°C of TH at millimolar concentration, which is identified from fish and plant. Hyperactive IBP is reported to bind to multiple ice planes including basal plane and shape ice crystal into, for example, lemon-like morphology [22]. Hyperactive IBPs, usually identified from insect and microorganism, exhibit TH activity of 2-7°C at micromolar concentration.

1.7.2. Ice recrystallization inhibition (IRI)

The ice is an aggregation of many single ice crystal with uneven size. With passage of time, large ice crystals form at the expense of smaller ones by a mechanism known as LSW theory or Ostward ripening (Figure 1.7.) [32,33]. Ice recrystallization is the expansion of the ice grains and their uniting process with keeping total amount of ice. Boundaries between ice grains have a tendency to be strained and unstable [34]. A considerable amount of liquid around the ice grains

act to recrystallize of ice at high subzero temperature, which results in a less total surface area of ice and an energetically favorable state. Ice recrystallizations occur when the temperature fluctuates diurnally and during the freeze-thaw cycle in frozen food or cryopreservation.

IBP exhibit ice recrystallization inhibition (IRI) activity at very low, micromolar concentration (Figure 1.7.). IRI activity of IBP was first reported using splat cooling assay in 1984 by Knight, C.A. *et al.* [35]. The splat cooling method is an aliquot of a solution is dropped onto cold metal to form an ice disk that consist of numerous fine-grained single ice crystals [36]. The time-dependent recrystallization is analyzed by time-lapse photography at -8°C . The modified method has been developed, for example, the sucrose-sandwich-splat assay [37] and glass capillary technique [38], which evaluate IBP concentration enough to exhibit completely IRI (IRI endpoint). Although IBPs are thought to bind to the surface of ice grains to inhibit their growth and uniting, the mechanism of IRI remain unclear.

1.8. Physiological function

IBPs are thought to protect their host from freezing damage. Types of organisms produced IBP are classified into freezing avoidant and freezing tolerant depending on their strategies [39–41]. Cold-adapted organisms such as fish and insects produce IBPs to depress noncolligatively freezing point in blood and hemolymph, respectively (Figure 1.8.A,B) [9,42,43]. Marine fish produced IBPs whose TH activity of approximately 1°C , to fill the gap between the freezing point of fish blood (-1°C) and sea water (-1.8°C). One of freeze avoidant insect, *Tenebrio molitor*, produce hyperactive IBP to adapt to environment where sands become lower than -5°C in the night [44]. Freezing avoidant is not able to recover after freezing. IBPs from freezing avoidant organism are usually called as antifreeze proteins (AFPs).

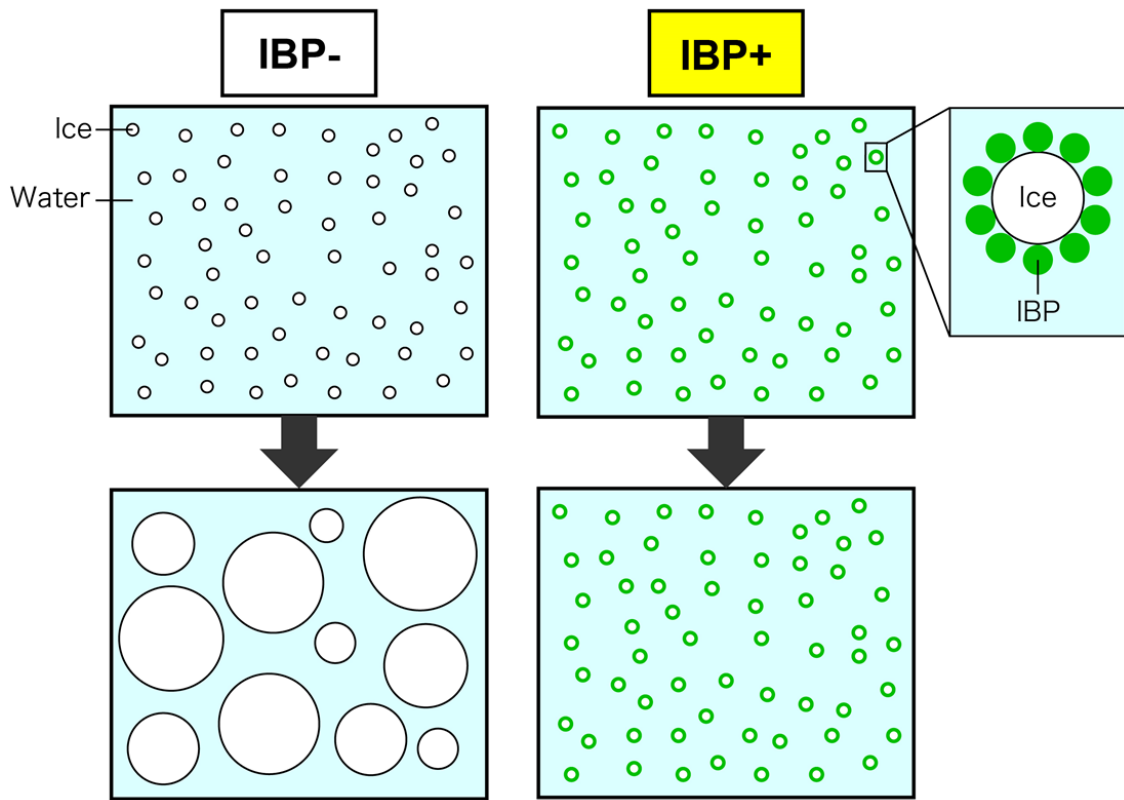


Figure 1.7. Schematic diagram of ice recrystallization inhibition (IRI).

Illustrations show the ice recrystallization process observed under photomicroscope with or without IBP. The ice grains at high subzero temperature fuse together and grow depending on time. In the presence of IBP, the fusion and growth process of ice grains are prevented by IBPs, leading to inhibiting ice recrystallization.

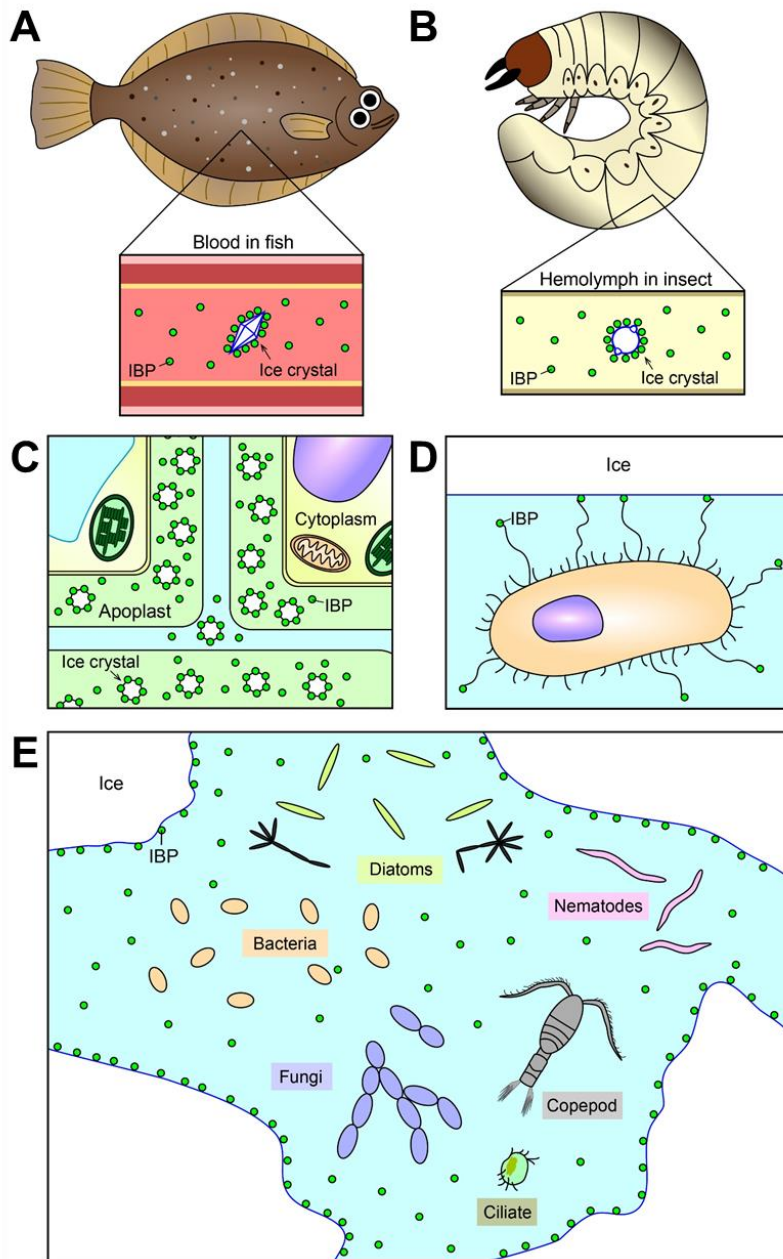


Figure 1.8. Schematic diagram of biological function of IBPs.

IBPs (green spheres) play a role to protect their host organisms from freezing injuries. **(A)** Fish produce IBPs in their blood and depress the freezing point of it. **(B)** Insects produce hyperactive IBPs in the hemolymph and avoid freezing. **(C)** Plant IBPs existing in apoplast inhibit ice recrystallization. **(D)** Some bacteria use IBP to attach to surface of ice floating via a long linker-proteins. **(E)** Many cold tolerant microorganisms (bacteria, fungi, diatoms, nematodes, copepod and ciliate) secrete IBPs with high IRI activity in extracellular space to keep their living liquid space.

Plants and microorganism are difficult to move and live in environment with high subzero temperature fluctuations, leading to inescapable freezing. Thus, they have been developed strategy of freezing tolerant [45–47]. Freeze tolerant organisms are thought to inhibit ice recrystallization and minimize freezing damage through producing IBPs with high IRI activity. Plants are known to face extreme environments like ice-laden environments and produce IBPs in intercellular spaces (apoplast) to protect their tissues from frost damage through its high IRI activity (Figure 1.8.C) [41,48,49]. Two bacteria use IBPs to anchor them to ice floating via a long linker-proteins from lipid bilayer of the cell, which gives them to gain access oxygen and nutrients (Figure 1.8.D) [50,51]. Most of microorganism is known to secrete IBPs extracellular space (Figure 1.8.E). Microorganism lived in sea maintain liquid environment using the secreted IBPs to keep brine channels open within sea ice [29,48,52–55].

1.9. Structures of IBPs

IBPs can commonly exhibit ice-binding ability in spite of varieties of amino acid sequence and structural characteristic. IBPs are classified into several group depending on their secondary structure and amino acid sequence.

1.9.1. Fish IBPs

Fish IBPs are divided into five types: AFGP, type I, II, III and IV IBP.

AFGP was first discovered from the blood serum of Antarctic Notothenioids [9]. AFGP consist of three repeating units of Ala-Ala-Thr, where C β of Thr is glycosylated with the disaccharide β -D galactosyl-(1 \rightarrow 3)- α -N-acetyl-D-galactosamine. Depending on a number of repeating units (n), 8 isoforms of this protein are known in molecular weight from 2.6 kDa (n=4) to 33.7 kDa (n=50) [56–58]. AFGP1 and 8 are largest and smallest molecules, respectively. AFGP is a left-handed helix that made a round every three residues and similar to poly-proline type II

helix (PPII) [59,60]. The sugar chains align in one side and form highly hydrophilic region. In opposite of them, hydrophobic residue like Ala occupied. AFGP are thought that sugar chain at regular interval interact with ice crystal by hydrogen bonding.

Type I IBP was first identified in 1976 from winter flounder *Pseudopleuronectes americanus* that lived in the western coastal waters of the North Atlantic [61]. The crystal structure of isoform 6 of w/IBP was determined in 1995 (Figure 1.9.A) [62,63]. IBP I is an alanine-rich amphipathic α -helix composed of three repeating of the 11-residue consensus sequence (Thr-Ala-Ala-X-Ala-X-X-Ala-Ala-X-X: X is mostly Ala) (Mw=3.3-4.5kDa) [64]. The four Thr residues apart on one side of the helix at equal space of 16.5Å, similar to the 16.7Å oxygen atom spacing in the pyramidal plane (20-21) [16]. Another type I IBP (Maxi) was discovered from the plasma of winter flounder *Pseudopleuronectes americanus* (Figure 1.9.D) [65]. Maxi is classified in hyperactive IBP to exhibit TH of 2°C. The X-ray crystal structure showed a dimeric four helix bundle [66].

Type II IBP was first discovered in 1981 from sea raven *Hemitripterus americanus* [67]. Type II IBP is a cysteine-rich globular protein (10 Cys residues) containing five disulfide bonds (Mw=14-24 kDa) and similar structure to C-type (Ca²⁺-dependent) lectin (Figure 1.9.B) [68–71]. Type II IBP was categorized into Ca²⁺-dependent type [68,69] and Ca²⁺-independent type [70], which has highly identity of sequence and crystal structure. Ca²⁺-dependent type II IBP binds to the primary prism plane through the residues Asp, Thr, and Glu of the Ca²⁺-binding loop and 1 mol Ca²⁺ ion [72]. Ca²⁺-independent type II IBP is thought to adsorb onto ice crystal through water molecules on flat hydrophobic surface surrounded by a similar loop region [70,71].

Type III IBP was first isolated in 1985 from Ocean pout *Macrozoarces americanus*, an inhabitant of the Newfoundland coastal waters [73]. Type III IBP is globular protein containing twisted loops folded into triple-strand β -sheets (Mw=6.5–7.0 kDa) (Figure 1.9.C) [74–77]. Type

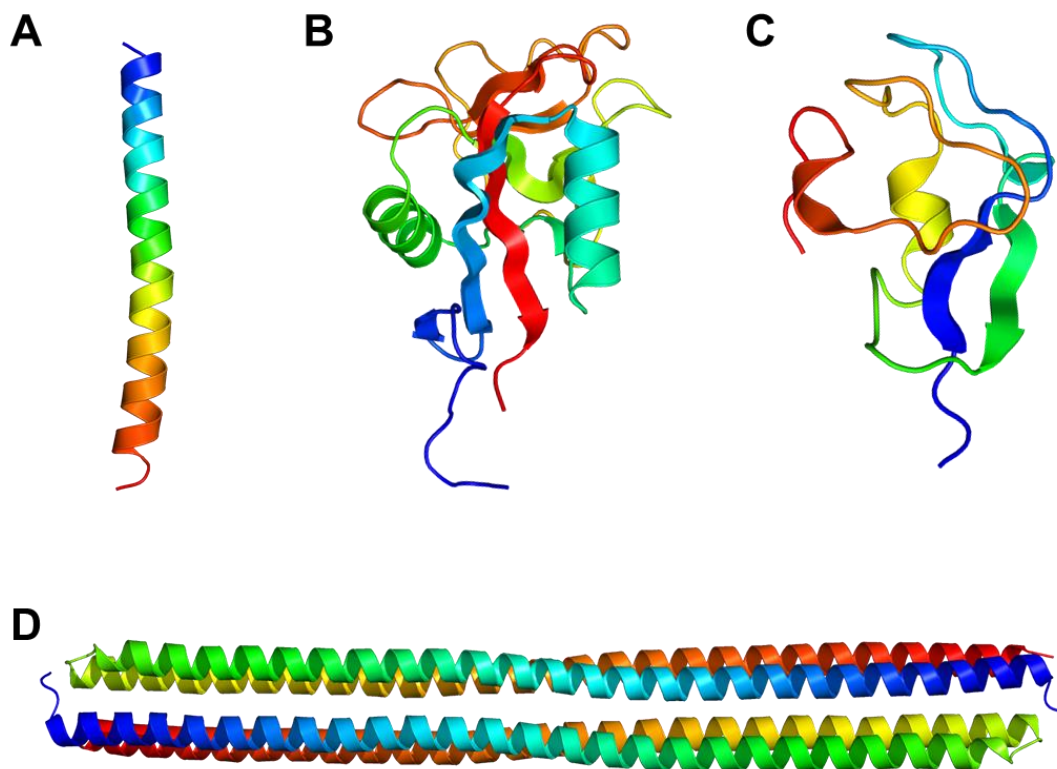


Figure 1.9. X-ray crystal structure of fish IBPs.

(A) Type I IBP from winter flounder (Protein Data Bank (PDB) code: 1WFA). (B) Type II IBP from longsnout poacher (PDB code: 2ZIB). (C) Type III IBP from ocean pout (PDB code: 1HG7). (D) Hyperactive type I IBP from winter flounder: Maxi (PDB code: 4KE2). All structures are represented in cartoon model and created by PyMOL.

III IBP is categorized into QAE-Sephadex- and SP-Sephadex-binding groups [73,78]. The former group is further divided into subgroups: QAE1 and QAE2 isoforms. QAE1 isoforms can inhibit ice crystal growth but SP and QAE2 isoforms only retards ice growth and exhibit no TH activity. Type III IBP possess a flat hydrophobic ice-binding site (IBS) that composed of two adjacent planar surfaces inclined at an angle 150°, where target plane is primary prism plane and pyramidal plane each planar surface [74,76,77,17].

Type IV IBP is assumed to form four-helix bundle [79]. Although type IV IBP was discovered in the longhorn sculpin, the concentration in the blood is known to be low thus predicted not to function as antifreeze agent [80].

1.9.2. Arthropod IBPs

Insect IBPs are known as hyperactive IBP to survive their host in habitat environments that harsh cold air temperature ($< -30^{\circ}\text{C}$) [81]. Insect IBP was first identified in 1997 from yellow mealworm *Tenebrio molitor* [82]. *Tm*IBP from beetle comprises of a right-handed β -helix structure (Mw=8.4 kDa), which contained seven or eight tandem repeats of a 12-residue consensus sequence (TCTxSxxCxxAx) (Figure 1.10.A) [83,84]. *Tm*IBP displays the Thr-Cys-Thr (T-C-T) pattern as the ice-binding site due to each β -strand exist on one side of the helix.

A moth, spruce budworm *Choristoneura fumiferana* produces IBP (*Cf*IBP) that contain Thr- and Cys-rich (Mw=9 kDa) (Figure 1.10.B) [42]. *Cf*IBP is left-handed β -helix structure and has T-X-T motif on their IBS similar to *Tm*IBP, which contained loop consisted of a 15-residue a tandemly.

A longhorn beetle *Rhagium inquisitor* that habitat of the winter season of Siberia produces a one 13-kDa IBP (*Ri*IBP) [85,86]. *Ri*IBP is flat and silk-like β -helical (solenoid) structure based on X-ray crystallography (Figure 1.10.C) [87]. The ice-binding site of *Ri*IBP is tight, two-layered

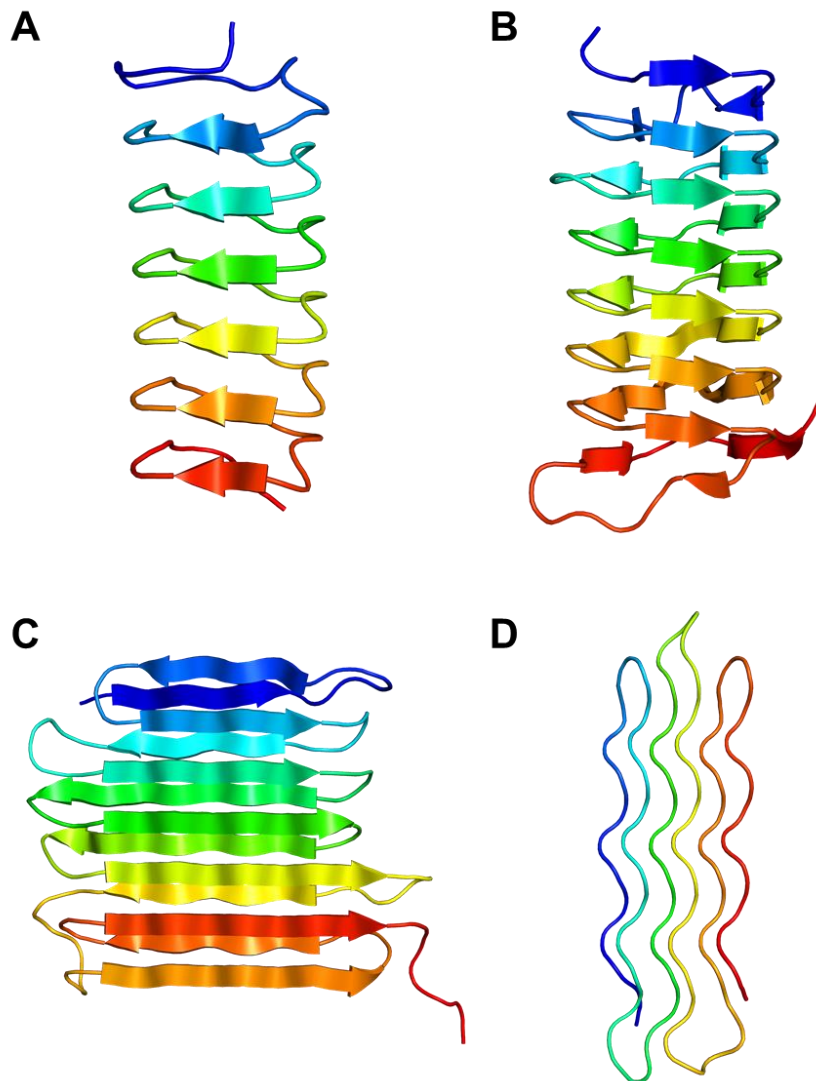


Figure 1.10. X-ray crystal structure of arthropod IBPs.

(A) *Tm*IBP from the beetle *Tenebrio molitor* (PDB code: 1EZG). (B) *Cf*IBP from the moth, spruce budworm *Choristoneura fumiferana* (PDB code: 1M8N). (C) *Ri*IBP from the longhorn beetle *Rhagium inquisitor* (PDB code: 4DT5). (D) *Sf*IBP from the snow flea *Hypogastrura harveyi* (PDB code: 2PNE). All structures are represented in cartoon model and created by PyMOL.

β -sandwich, which compose of four arrays of Thr residues and comprise the TXTTXT motifs.

*Ri*IBP exhibit TH of around 6.5°C, which is one of highest activity among all IBP categories.

An inchworm, larvae of the pale beauty moth *Campaea perlata*, produce two Thr-Ala rich IBP (*iw*IBP) isoforms with high TH of 6.4°C (Mw=3.5 or 8.3 kDa). The 8.3-kDa isoform of *iw*IBP is predicted to fold into a flat silk-like β -helical structure [88].

Snow flea *Hypogastrura harveyi* produces two isoforms (*sf*IBP) containing glycine-rich (Mw=6.5 or 15.7 kDa) [89]. The X-ray crystal structure of 6.5-kDa isoform showed the protein made up of six antiparallel left-handed PPII-like helices (Figure 1.10.D) [90]. This stacked in two sets of three to form compact brick-like structure with hydrophilic and hydrophobic faces on the opposite sides. The structure of 15.7-kDa isoform is predicted similar to the small isoform [91].

Recently, it was reported that a springtail (Collembola) *Granisotoma rainieri* collected from snow in Hokkaido, Japan, also produce glycine-rich IBP (*Gr*IBP) [92]. The X-ray crystal structure showed a PPII helical bundle, which is similar to the structure of *sf*IBP with six-helix while the number of helices is different (nine-helix).

1.9.3. Plant IBPs

The antifreeze activity in plant was first confirmed in 1992 [93]. IBP was found from overwintering plant, which possess weaker TH but higher IRI activity to minimize the damage caused by ice recrystallization. Plant IBPs were thought to not only support to tolerate freezing state but also provide protection against psychrophilic pathogens.

A forage grass, perennial ryegrass *Lolium perenne*, produce a heat-stable IBP (*Lp*IBP) that exhibit high IRI but low TH activity (Mw=11 kDa) [49]. The crystal structure of *Lp*IBP was determined, which showed a left-handed β -roll structure with eight 14- and 15-residue coils (Figure 1.11.A) [94]. *Lp*IBP has very similar structure to insect IBP but no regularity in amino-

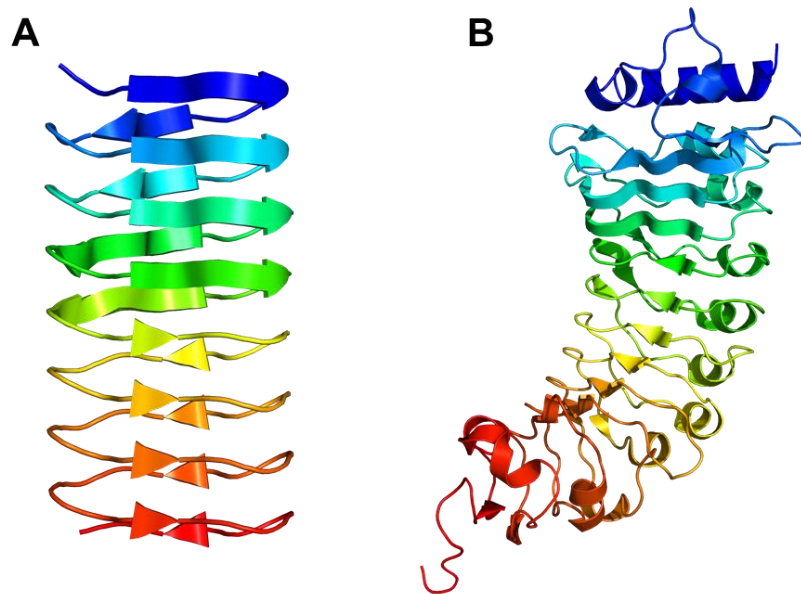


Figure 1.11. X-ray crystal structure of plant IBPs.

(**A**) *Lp*IBP from the forage grass, perennial ryegrass *Lolium perenne* (PDB code: 3ULT). (**B**) *Dc*IBP from the carrot *Daucus carota* (PDB code: 6W78). All structures are represented in cartoon model and created by PyMOL.

acid sequence of ice-binding site.

A common vegetable, carrot *Daucus carota*, produce an N-glycosylated Leu-rich IBP (*DcIBP* or *DIBP*) with molecular weight of 36-kDa [37,46]. *DcIBP* composed of 24-amino acid tandem repeats. The crystal structure of *DcIBP* determined in 2020 shows a curved solenoid structure homologously to plant polygalacturonase-inhibiting protein (Figure 1.11.B) [95]. The IBS of *DcIBP* was determined on the convex surface of the solenoid but not flat surface likely to other IBPs. *DcIBP* was reported to exhibit extremely IRI activity at nanomolar concentration.

1.9.4. Microbial IBPs

Antifreeze activity was first confirmed in bacteria and fungi in 1993 [45]. The structure of microbial IBP was determined in 2012 (Figure 1.12.A,B) [96,97]. IBPs have been discovered from most microorganism including bacteria [98], yeast [99], fungi [100], diatoms [101], and copepods [102], which shares a common β -helical fold unlike IBPs from fish, insects and plants. These IBP are called as domain of unknown function (DUF) 3494 IBP (Figure 1.12.A-C) [103]. Microbial IBPs consisted of many β -helix regardless of no repetitive amino acid sequence, whose β -helix is irregularly stacked along with a α -helix. They have common three-dimensional structure while do not have common ice-binding motif. IBPv contains two consecutive DUF3494 domains, from which the *Flavobacteriaceae* strain 3519-10 expresses in nature (Figure 1.12.D) [104,105]. A 17-residue linker connects two DUF3494 domains.

The structure of bacterial IBP from arctic bacterium *Marinomonas primoryensis* was reported different from that of DUF3494 IBPs. *MpIBP* is large β -solenoid structure including linearly aligned internal Ca^{2+} ions (Figure 1.12.E) [106]. Although Ca^{2+} ions are not involved in ice-binding, it is thought to be important to stabilize the structure because antifreeze activity is

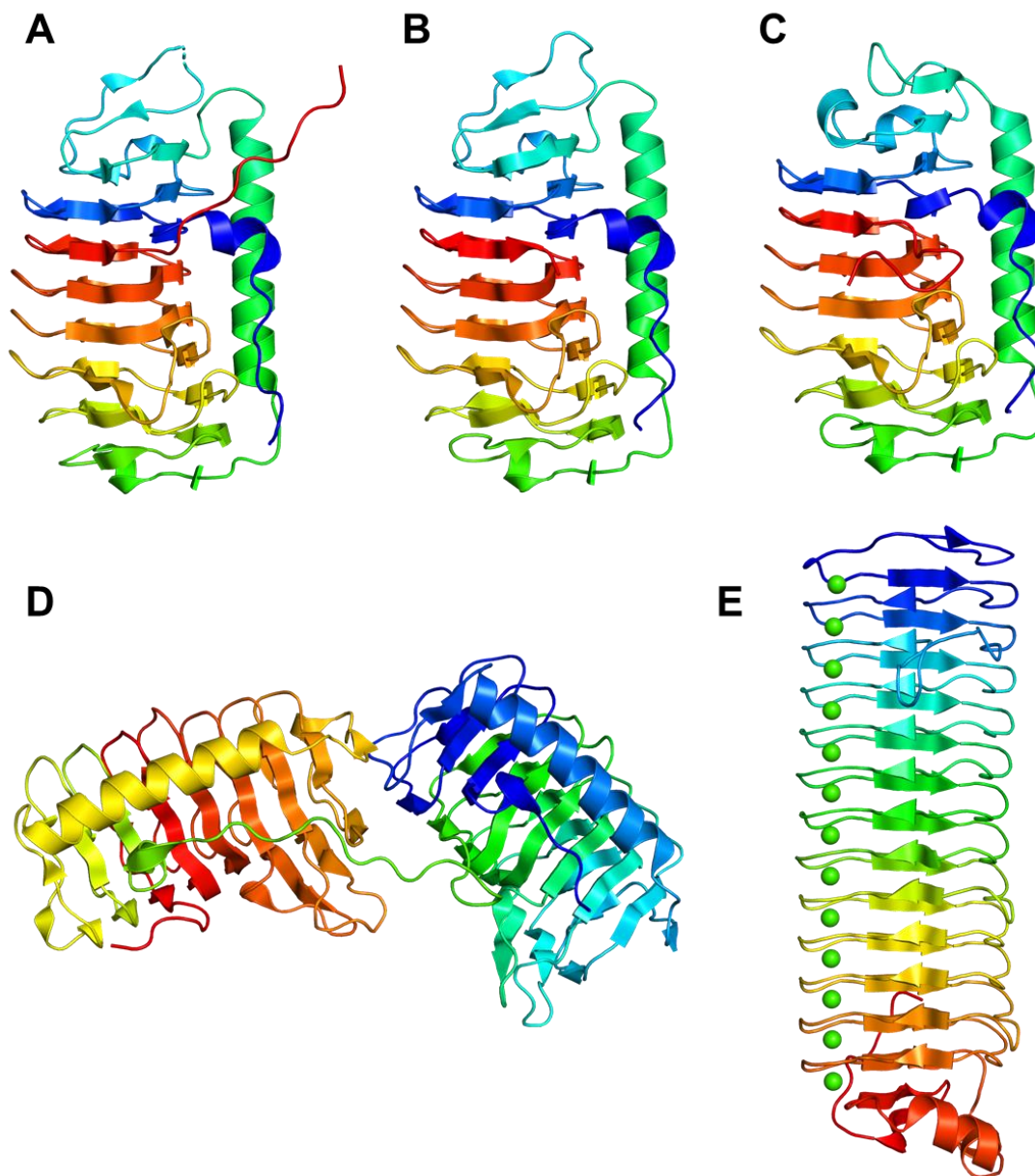


Figure 1.12. X-ray crystal structure of microbial IBPs.

(A) *LeIBP* from the Arctic yeast, *Leucosporidium* sp. AY30 (PDB code: 3UYU). (B) *TisIBP* from the snow mold fungus *Typhula ishikariensis* (PDB code: 3VN3). (C) *ColIBP* from the Antarctic sea ice bacterium, *Colwellia* sp. Strain SLW05 (PDB code: 3WP9). (D) *IBPv* from a bacterium within the family *Flavobacteriaceae* (isolate 3519-10) in the Vostok Ice Core (PDB code: 5UYT). (E) *MpIBP* from an Antarctic bacterium, *Marinomonas primoryensis* (PDB code: 3P4G). All structures are represented in cartoon model and created by PyMOL.

confirmed only in the presence of the ion. *Mp*IBP is known to possess unique ice-binding motif (Thr-X-Asx) on its IBS.

1.10. Ice-binding mechanism of IBPs

Hydration waters of proteins are generally crucial for its structure and function. IBPs have been examined the relationship between hydration waters and the ice-binding function. IBPs possess one or two IBSs consisted of many hydrophobic residues making a flat surface, whose IBS organize hydration waters in an ice-like geometry on its surface [106]. Most of studies suggested that hydration waters on IBSs completely matching water arrangement of ice lattice.

Several IBPs are reported to observe “cage” like bound waters consisted of polygonal structure of hydration waters on IBSs. Single ice crystal is hexagonal but the caged water molecules exhibit a pentagonal arrangement and therefore are called “ice-like” water molecules. These ice-like water molecules are assumed to merge with water molecules (quasi-liquid layer) constructing ice-water interface of an ice crystal, which anchor IBP to an ice crystal surface. Thus, this is known as anchored clathrate water (ACW) mechanism. The polygonally arranged water molecules on IBS has recently been found in *Mp*IBP, fish hyperactive type I (Maxi) and type III IBPs and so on [66, 107–109]. For example, type III IBP possess water arrangement matching prism and pyramidal plane in polygonal waters networks [109]. Some IBPs organize polygonal waters while other IBPs are not confirmed them in the structure [22,29,42,81,84]. Such hydration waters are partly observed in crystal structure because IBPs locate in face to face in crystal packing structure due to hydrophobic interaction between hydrophobic IBSs. This packing cause to force out bound waters on IBSs, leading not to understand original water positions [110]. Thus, the ice-binding mechanism still not completely understand and is assumed there are unique ice-binding manner for each IBP.

1.11. Purpose and scope of this dissertation

A cold-tolerant ascomycete *Antarctomyces psychrotrophicus*, which is isolated from several substances of Antarctica such as soils [111], waters in lakes [112], marine macroalgae [113], are known to secrete IBP (*Anp*IBP) in extracellular space [114]. *Anp*IBP with a molecular weight of less than 28 kDa belongs to moderately active IBP depending on their TH activity ($\sim 0.7^{\circ}\text{C}$ at the concentration of 300 μM). In contrast, *Anp*IBP modified ice crystal generated in supercooled water into a lemon-like shape that is usually observed in hyperactive IBP [115]. Ice-binding properties of *Anp*IBP are thought to reflect the unique structural properties. Microbial IBP do not contain consensus sequence in IBS so that many researchers are interested how they recognize specific ice planes. The study of *Anp*IBP will hence give us a significant clue to understand unique ice-binding mechanism of microbial IBPs.

The temperature become subzero ($< 0^{\circ}\text{C}$) in not only polar region such as Antarctica but also winter season in Japan. There are many cold-adapted organisms in Japan, among which overwinter insects are well-known. Beetles are reported to be dominant among overwinter insects found from tree in winter of Hokkaido [116]. However, it has not been progressed IBP research on such Japanese insects. Also, in worldwide, IBPs have been examined only in four beetles belonging to the superfamily *Tenebrionoidea* [82,117–119]. Japanese stag beetle *Dorcus hopei binodulosus* (*Dhb*) is a-long life overwintering insect, whose larva is known to be able to alive in tree root stock at -5°C [116,120,121]. *Dhb* is easily available insect to purchase adult and larvae from the shop, of which the breeding methods have been established. *Dhb* beetle belongs to a superfamily *Scarabaeoidea*, which is different to former superfamily *Tenebrionoidea*. Thus, a study of IBP using *Dhb* leads to understanding the role and function of IBP in Japanese overwintering insect and the origin of hyperactive insect IBP.

In this study, we analyzed the structure-function relationship of moderately active microbial IBP and hyperactive insect IBP. To examine ice-binding properties of IBPs, we employed further methods including molecular biology and structural biology.

Chapter 2: Elucidation of ice-binding mechanism of microbial *AnpIBP*

Preface: This chapter was published in *Biomolecules*: Yamauchi, A., Arai, T., Kondo, H., Sasaki, Y.C. and Tsuda, S. (2020) An ice-binding protein from an Antarctic ascomycete is fine-tuned to bind to specific water molecules located in the ice prism planes.

2.1. Abstract

Many microbes that survive in cold environments are known to secrete ice-binding proteins (IBPs). The structure-function relationship of these proteins remains unclear. A microbial IBP denoted *AnpIBP* was recently isolated from a cold-adapted fungus, *Antarctomyces psychrotrophicus*. The present study identified an orbital illumination (prism ring) observed on a globular single ice crystal hemisphere when soaked in a solution of fluorescent *AnpIBP*, suggesting that *AnpIBP* binds to specific water molecules constructing the ice prism planes. In order to examine this unique ice-binding mechanism, we carried out X-ray structural analysis and mutational experiments. It appeared that *AnpIBP* is made of 6-ladder β -helices with a triangular cross section that accompanies an "ice-like" water network on the ice-binding site. The network, however, does not exist in a defective mutant. *AnpIBP* has a row of four unique hollows on the IBS, where the distance between the hollows (14.7 Å) is complementary to the oxygen atom spacing of the prism ring. These results suggest the structure of *AnpIBP* is fine-tuned to merge with the ice-water interface of an ice crystal through its polygonal water network and is then bound to a specific set of water molecules constructing the prism ring to effectively halt the growth of ice.

2.2. Introduction

Proteins bind to their ligands to perform specific functions. Hydration water molecules in a protein play a significant role in ligand binding and also have roles in dissolving proteins in water and maintaining their tertiary structures [122,123]. Some hydration water molecules located on an ice-binding protein (IBP) are known to be arranged polygonally, similar to the hexagonally latticed waters of ice crystals formed under atmospheric pressure [9,106]. The presence of regularly arrayed troughs, which trap the hydration water molecules at regular intervals, has also been reported in some IBPs [22,29,42,81,84]. These water molecules are arranged in an ice-like geometry and are thus called “ice-like waters”. A role for these molecules in anchoring the host protein to ice crystal surfaces has been postulated.

The IBPs isolated from cold-adapted organisms such as fish, insects, plants, and microorganisms [4] are known to inhibit ice growth through binding to the water molecules constructing the crystal surface. Such ice, a ligand of IBP, is a solid state of water in which the water molecules are systematically organized into a hexagonal arrangement. This arrangement is the principle feature of the single ice crystal created at one atom defined by three equivalent a -axes (a_1 – a_3) perpendicular to the c -axis [12]. The hexagonal ice (denoted I_h) has six primary prism planes and six secondary prism planes along the c -axis. These prism planes lie parallel and perpendicular to the a -axes, respectively. The basal plane lies perpendicular to the c -axis and parallel to the a -axis. Other inclined planes between the basal and prism planes are defined as pyramidal planes. It has been demonstrated that the growth speed of the prism planes toward the a -axis is approximately 100 times faster than that of the basal planes toward the c -axis [20]. A snowflake is an example of a hexagonal single ice crystal, though its preparation is very difficult. An alternative handling technique for single ice crystals was recently developed [17], in which a single ice crystal hemisphere 3–4 cm in diameter is created by utilizing a plastic pipe and a cooling

bath. We can determine the a - and c -axes of this golf-ball-size single ice crystal using a polarizer, where its earth-axis corresponds to the c -axis of I_h . When such an ice hemisphere is mounted on a frosty probe with the desired orientation, and soaked in a solution of fluorescence-labeled IBP, a pattern appears on the globular ice surface under ultraviolet (UV) light. This is called the pattern of fluorescence-based ice plane affinity (FIPA) of an IBP species, as presented in [18]. Variations of the FIPA pattern have recently been reported [19]. From these data, one can correlate the ice planes constructing the hexagonal single ice crystal and the FIPA patterns created on the globular single ice crystal. For example, the FIPA pattern observed at the polar area of a globular single ice crystal implies the basal-plane binding of an IBP.

In addition to the FIPA pattern, IBP's ice-binding ability can be detected by the observation of morphological change in an ice crystal and thermal hysteresis (TH) activity. Both observations require a photomicroscope system equipped with a cooling stage, whose temperature needs to be lowered to deep freezing temperatures, such as -40°C . IBP changes the photomicroscope image of a single ice crystal into a hexagonal bipyramid, a hexagonal trapezohedron [18,19], or a lemon-like shape [22], depending upon the type and number of ice planes growth terminated by an IBP species [29]. TH is the difference between the melting and freezing temperatures (T_m and T_f) of a single ice crystal prepared in an IBP solution; $\text{TH} = |T_m - T_f|$ [8,18,28,30]. The two temperatures are equal for normal solutions, and the presence of IBPs decreases T_f and slightly raises T_m to generate the TH, which can be evaluated with a photomicroscope system as described earlier [31]. IBP from fish and plants generally exhibit $0.5\text{--}1.5^{\circ}\text{C}$ of TH activity at millimolar concentrations, and they are called "moderately active IBP". In contrast, insect and microbial IBPs that exhibit $2\text{--}6^{\circ}\text{C}$ of TH activity even at micromolar concentrations are called "hyperactive IBPs" [22].

IBPs have been used to elucidate the relationship between hydration water molecules and the ice-binding function. IBPs have one or two ice-binding sites (IBSs), which consist of many

hydrophobic residues making a flat surface in which several polar residues are inserted at regular intervals or dispersively [29]. For several IBP species, “caged” hydration water molecules were observed on the hydrophobic IBS with some hydrogen bonding to the polar residues. The caged water molecules are not hexagonally organized but exhibit a pentagonal arrangement and therefore are called “ice-like” water molecules [66,106,108,109]. For example, IBP from *Marinomonas primoryensis* (*Mp*IBP) has pentagonally arranged water molecules on its IBS [106]. These molecules exist in the vicinity of CH₃ groups of Thr side chains and are stabilized on the IBS through hydrogen bonding to the main-chain nitrogen and side-chain hydroxyl groups of Thr, as well as to the side-chain oxygen atom of Asp. The ice-like water molecules are thought to play a significant role in facilitating IBP binding to ice crystals and are known as anchored clathrate water (ACW). Polygonally arranged water molecules have been observed for moderately active type II and III IBPs [108,109], as well as hyperactive type I IBP (*Maxi*) [66,107], but not for insect IBPs [22,29,42,81,84]. Instead, surface water molecules are trapped in regularly arrayed troughs on insect IBPs, which are made of two rows of Thr residues, and the spacing of the oxygen atom of the trapped water molecules matches the distance between water molecules in both basal and prism planes of a single ice crystal. Such troughs are created by the repetitive nature of the amino acid sequence of IBPs from *Tenebrio molitor* (*Tm*IBP) and *Dendroides canadensis* (*DIBP*), which consists of a 12-residue consensus sequence TCTxSxNCxxAx repeated tandemly, where T, C, S, N, and A are Thr, Cys, Ser, Asn, and Ala, respectively, and x represents any residue [84,124]. *Anp*IBP does not have any tandem repeat sequences [115], and it is not clear what structure it forms or how it binds to ice crystals.

IBPs from microorganisms including bacteria [106], fungi [97], diatoms [53], and copepods [102] share a common structure, denoted the domain of unknown function (DUF) 3494 [103]. This domain is constructed of approximately 230 amino acids (~25 kDa) and speculated

to be widespread, having been passed many times between prokaryotic and eukaryotic microorganisms by horizontal gene transfer [102,115]. The DUF3494 domain is characterized by a uniquely formed β -helical structure, which is also assumed to exist in *AnpIBP*. IBP from the Antarctic bacterium *Colwellia sp.* SLW05 (*CoIBP*) and that from Arctic yeast (*LeIBP*) are both contain the DUF3494 domain. The former exhibits high TH activity ($\sim 4^{\circ}\text{C}$) at $140\ \mu\text{M}$ [125], whereas the activity of *LeIBP* is much lower (0.35°C), even at $370\ \mu\text{M}$ [96]. The *AnpIBP* exhibited TH activity ($\sim 0.7^{\circ}\text{C}$) at $300\ \mu\text{M}$, which was the same level as that of the moderately active fish IBP. An ability to modify ice crystals into a lemon shape is regarded as a typical sign of high TH activity. *AnpIBP* was reported to generate such a lemon-shaped crystal, although it is only moderately active [115]. The present study used the FIPA experiments and X-ray crystal structure determination of a recombinant protein of *AnpIBP* and a mutant version for which an extraordinary ice-binding property has been suggested. Here we present new structural data for an IBP identified from a cold-tolerant fungus, *Antarctomyces psychrotrophicus* (*AnpIBP*). *AnpIBP* showed a unique ability to bind to the equator region of a single ice crystal when we prepared it in a globular form, a phenomenon that we called a “prism ring”.

2.3. Materials and methods

2.3.1. Expression and purification of recombinant *AnpIBP* and its mutants

Wild-type *AnpIBP* and its mutant version were prepared as described previously, using *Pichia pastoris* as the host organism [115]. Briefly, a DNA encoding His-tag (His \times 6) plus the Ala1-Val216 sequence of *AnpIBP* was inserted downstream of an α -factor signal sequence in the expression vector pPICZ α . The vector was transformed into *P. pastoris* after linearization by a restriction enzyme. The transformant was precultured in buffered glycerol complex medium, followed by 96–120 h incubation in methanol-containing medium, to express *AnpIBP*. The culture was then centrifuged to collect the medium containing *AnpIBP*. The protein was purified by a series of ion-exchange chromatography passes (High S and High Q, Bio-Rad, Hercules, CA, USA) and further purified by size-exclusion chromatography (Superdex 200, GE Healthcare, Chicago, IL, USA). The mutant proteins were prepared using the same procedure. The purity of these samples was confirmed by sodium dodecyl sulfate-polyacrylamide gel electrophoresis (SDS-PAGE). We have previously reported that *A. psychrotrophicus* secretes glycosylated *AnpIBP* at the Asn55 position [115]. The *AnpIBP* under investigation here, expressed in *P. pastoris*, was also thought to be glycosylated, because it showed multiple or smear bands in SDS-PAGE. We found that the substitution of Asn55 with aspartic acid produced a non-glycosylated form of *AnpIBP*, and the N55D mutant of *AnpIBP* is defined as *AnpIBP* hereafter. Further amino acid replacements were made in this *AnpIBP*. The S153 of *AnpIBP* was replaced with Tyr, for example, and is called the S153Y mutant in this article. These samples were dissolved in water or 20 mM Tris-HCl at pH 8.0, and concentrated by ultrafiltration (Mw cutoff = 3 kDa) (Merck Millipore, Burlington, MA, USA). Their final concentration was determined using UV absorbance at 280 nm with a coefficient calculated on the basis of the amino acid sequence.

2.3.2. Thermal hysteresis measurements and ice crystal morphology

The TH activity of *Anp*IBP and its mutants was measured by observation of a single ice crystal prepared in an IBP solution, using a photomicroscope equipped with a temperature-controlled stage and a Charge Coupled Device (CCD) camera, as described previously [31] (Figure 2.1.). A 1- μ L sample solution in a glass capillary tube was flash frozen to approximately -25°C and slowly warmed to near 0°C to observe a single ice crystal. For this crystal, we initially measured the melting point (T_m) while increasing the stage temperature. We then prepared another single ice crystal, and lowered the temperature with a cooling rate of $0.1^{\circ}\text{C}/\text{min}$. An ice crystal does not start to grow when the temperature is higher than the lower limit of TH, and it shows bursting growth when this limit is exceeded, which is determined to be the freezing point (T_f). The difference between the two temperatures ($T_m - T_f$) is defined as the TH value [8,18,28,30]. The TH was measured at least three times, and an averaged value was plotted at concentrations between 30 and 500 μM .

2.3.3. FIPA analysis

In order to identify the IBP-bound plane of a single ice crystal, the FIPA pattern was observed for our samples using the procedure described in [18]. A single ice crystal was prepared in a polyvinyl chloride (PVC) pipe ($\text{O} = 30$ mm and height = 30 mm) with a tiny notch (1 mm \times 2 mm) placed on the aluminum tray (Figure 2.2.). Degassed water was poured into the tray to 5 mm in depth and cooled to -0.5°C . Ice growth was initiated by adding a small piece of ice to the supercooled water, which was propagated into the PVC pipe through the notch, acting as a seed to generate a single ice crystal. When the inside of the pipe started freezing, degassed water was carefully added into the PVC pipe. After further incubation at -1.8°C for 3 days, a single cylindrical shaped ice crystal was created in the pipe. The crystallographic c - and a_1 - a_3 -axes of

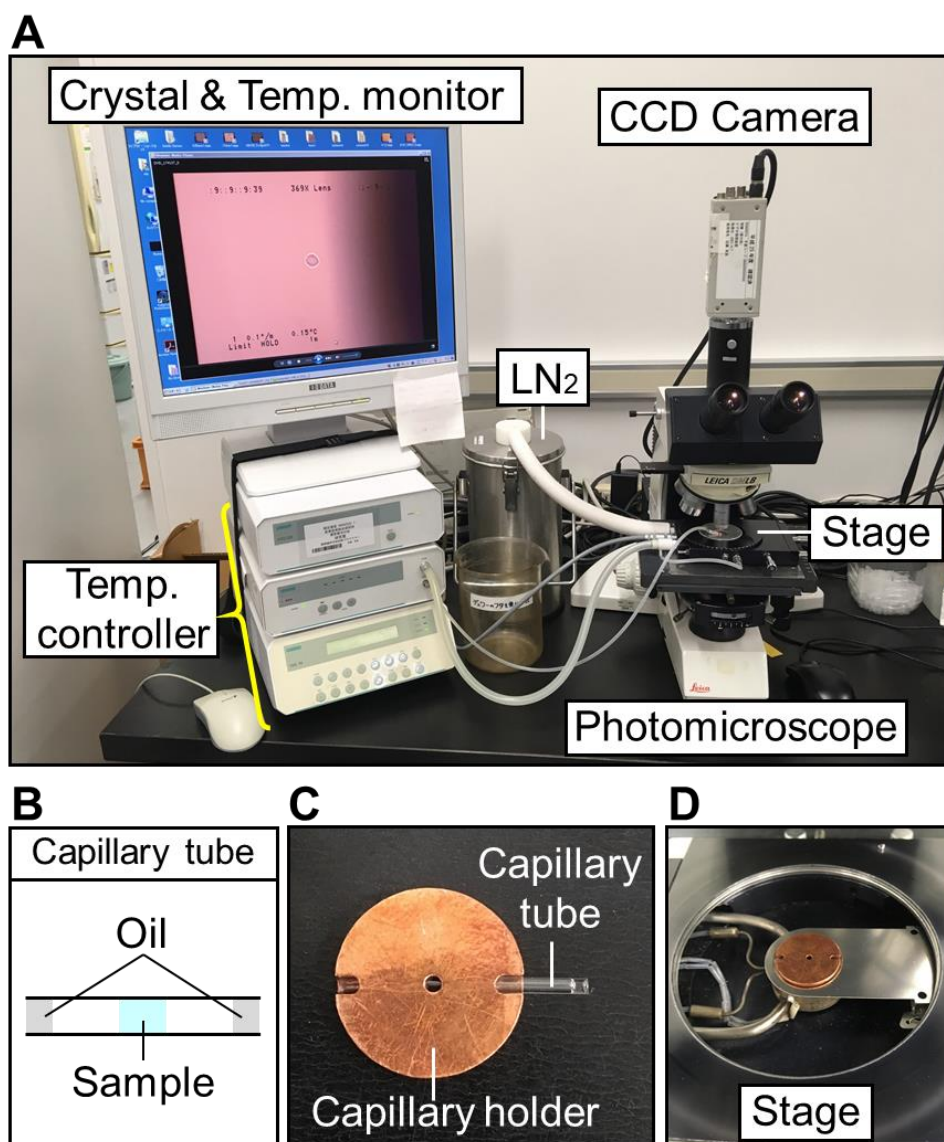


Figure 2.1. Experimental setup for TH measurement of an IBP solution.

(A) A photomicroscope equipped with a temperature-controlled stage, a CCD camera and liquid nitrogen (LN₂). The stage temperature can be changed to the desired temperature set by the temperature controller, regulating with LN₂. A display shows the observed crystal and stage temperature. (B) Sample in a capillary tube. About 1- μ L sample solution was added in a glass capillary tube. A mineral oil (0.5- μ L) was placed on both ends of capillary as a lid. (C) The capillary tube (sample) set in a capillary holder made of copper. (D) Sample set on the temperature-controlled stage to measure TH.

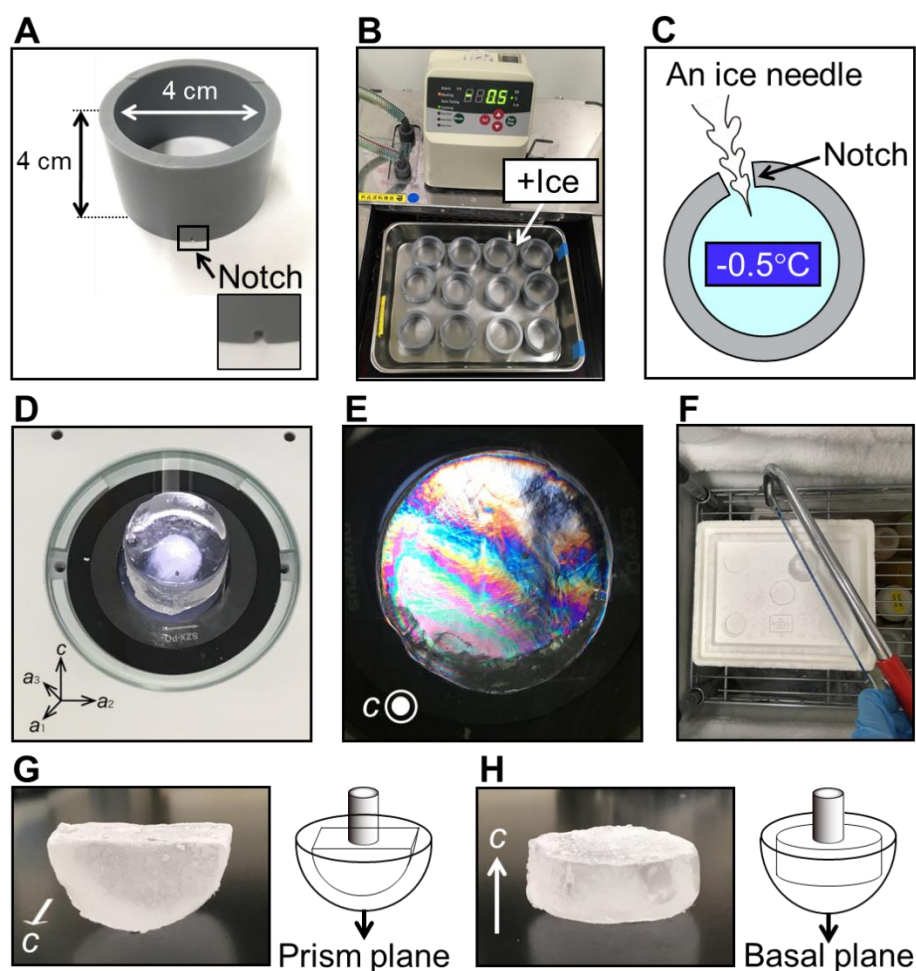


Figure 2.2. Preparation of a single ice crystal for FIPA analysis.

(A) PVC pipe (width & height: 4 cm) with a notch at the bottom. (B) The PVC pipes placed on the aluminum tray put in a cooled water bath. A small piece of ice was added to the supercooled water (-0.5°C) to initiate ice growth. (C) Illustration shows a state of the added ice crystal propagating into the PVC pipe through the notch. The needle shaped ice acts to generate a single ice crystal in the pipe. Degassed water was further added into the PVC pipe after water freezing inside of it. After 3 days-incubation at -1.8°C , a single cylindrical shaped ice crystal was obtained. (D) The single cylindrical ice crystal put on polarizers to check the crystallographic c - and a_1 - a_3 -axes. (E) The crystallographic c -axis (basal plane) was identified when the cylindrical ice crystal showed iridescence on polarizers. (F) Single cylindrical ice crystal cut into halves with a saw. Half single ice crystals were used for observation of (G) the prism-plane binding and (H) the basal-plane binding of IBPs. The half crystal was mounted on a copper rod with a desired orientation and modified into a hemispherical shape.

this cylindrical ice crystal were checked using polarizers. The crystal was modified into a hemispherical shape ($\varnothing = 30$ mm) with a heated stick and was mounted on a chilled copper rod with a desired orientation. The single ice crystal hemisphere mounted on the rod was soaked in a 40-mL solution of fluorescence-labeled IBP so as to face down the curved front of the crystal. The fluorescence dye used was tetra-methyl-rhodamine (5 (6)-TAMRA-X, SE: Thermo Fisher Scientific, Waltham, MA, USA). The single ice hemisphere was held in the solution for 4–5 h at -5°C . When it became golf ball sized ($\varnothing = 5$ cm), it was detached from the copper rod to observe the FIPA pattern under UV light in a cold room (-1°C).

2.3.4. Crystallization and X-ray structure determination of *AnpIBP* and its mutants

The *AnpIBP* and its S153Y mutant prepared without His-tag were crystallized using the hanging drop vapor diffusion method [126]. A 1- μL solution of each solution, with the concentration adjusted to 20 mg/mL was mixed with an equal volume of a crystallization solution at 20°C . Large crystals of wild-type *AnpIBP* were obtained when they were dissolved with 0.1 M HEPES-NaOH pH 8.6, 0.95 M ammonium sulfate, and 0.1 M lithium sulfate. The S153Y mutant was crystallized with 0.1 M Bis-Tris pH 7.0 and 4.0 M ammonium acetate. The experiments using synchrotron radiation were performed with the approval of the Photon Factory Program Advisory Committee (proposal number 2018G105). Diffraction data for *AnpIBP* and the S153Y mutant were collected at the beam line BL-17A [127] at the Photon Factory KEK, Japan, and were processed using XDS [128] and the CCP4 [129] program suit. The crystal structure of *AnpIBP* was determined using the molecular replacement method using Phenix [130] with a coordinate file of *ColIBP* (PDB code: 3WP9) [125] as a search model. In this model, a 21-residue segment between Pro38 and Leu74 of the original *ColIBP* coordinate was removed, because the corresponding segment does not exist in *AnpIBP*. The initial model structure of *AnpIBP* was

further refined using the software packages Phenix, Refmac5 [131], and Coot [132]. The structure of the S153Y mutant was also determined using the molecular replacement method with the coordinate file of *AnpIBP*. The statistics for data collection and refinement [133] are summarized in Table 2.1. The crystal packings of wild-type *AnpIBP* and S153Y mutants are shown in Figure 2.4. The coordinates were deposited in the Protein Data Bank (PDB) under code 7BWX for *AnpIBP* and 7BWY for the S153Y mutant.

2.4. Results and Discussion

2.4.1. FIPA of *Anp*IBP showed a novel prism-ring pattern

Figure 2.3.A,B shows the FIPA patterns observed for *Anp*IBP, for which illustrated interpretations are presented in Figure 2.3.C,D, respectively. The contiguous illumination ring was observed at the rim of the hemisphere, when it was soaked into the IBP solution to direct its *c*-axis downward (Figure 2.3.A,C). On a different ice hemisphere whose *a*₃-axis was directed downward, the fluorescence from ice-bound *Anp*IBP was observed in the area between the equator and a middle latitude but not in the polar region (Figure 2.3.B,D). The ring area is centered at the equator, implying that it is made of the water molecules that participate in both the primary prism and the secondary prism planes. For simplicity, we named this orbital FIPA pattern (Figure 2.3.A) a prism ring; *Anp*IBP binds to the water molecules constructing the prism ring. Note that a faint yellow circle observed at the center of hemisphere is an artifact arising from the hole left by the metal rod used to hold and cool the ice crystal [18].

It has been shown that the FIPA pattern is sometimes changed with increases in the concentration of IBP [134,135]. For example, the pattern was observed in a limited area for a 0.01-mg/mL solution of fish type I IBP from barfin plaice, and it was overcast by the entire illumination when the protein concentration was increased to 0.1 mg/mL. This observation was interpreted as indicating that this IBP binds only to the pyramidal plane at 0.01 mg/mL, whereas it covers the whole ice crystal, including the basal plane, when its concentration is 10 times higher [134]. A similar change was observed for type II IBP from longsnout poacher (*Lp*IBP) [135]. We performed a concentration dependence experiment for *Anp*IBP between 0.01 and 0.15 mg/mL. The FIPA pattern did not change with increasing concentration; *Anp*IBP binds to the prism ring but not to the basal plane, even at the highest concentration (data not shown). *Anp*IBP is a member of the microbial IBPs containing the DUF3494 domain. The FIPA pattern reported for the known

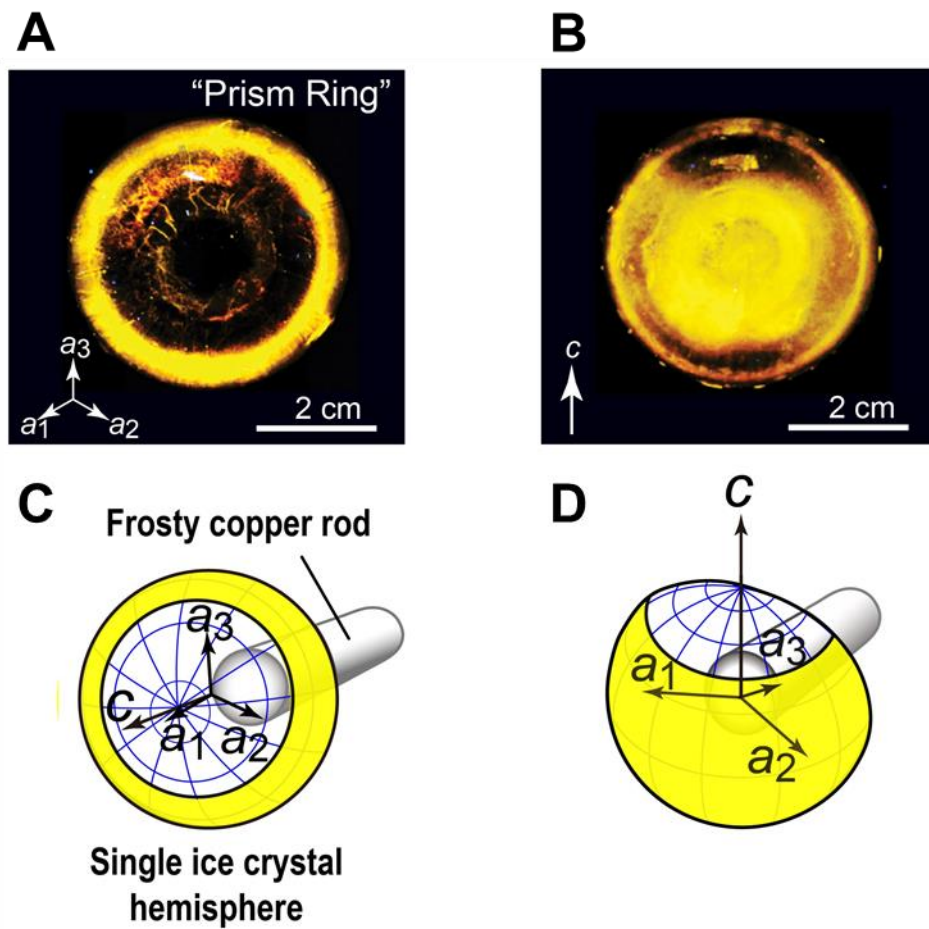


Figure 2.3. Observation of fluorescence-based ice plane affinity (FIPA) of *AnpIBP*.

(A) A ring-like FIPA pattern of *AnpIBP* (denoted a “prism ring”). The ice hemisphere was mounted on a frosty copper rod to align its c -axis with the rod as illustrated in (C), and then soaked in 0.1 mg/mL protein solution to direct the c -axis downward. The prism ring was observed at the rim of the hemisphere, suggesting that *AnpIBP* binds to the water molecules that participate in both the primary prism and secondary prism planes. (B) The FIPA pattern of *AnpIBP* observed on a different ice hemisphere whose a_3 -axis is normal to the paper as illustrated in (D). The pattern shows that the prism ring observed in (A) is spread from the equator to a higher latitude.

DUF3494-characterized IBPs, such as *Col*IBP [125], *Tis*IBP [136], *Sfi*IBP [137], and *Ffi*IBP [138], showed that they are all capable of binding to the basal plane. This observation implies that *Anp*IBP is exceptional, and its manner of binding to the prism ring is controlled by a unique structural property.

2.4.2. *Anp*IBP folds as an irregular β -helical structure

To clarify the manner of ice binding, the X-ray crystal structure of *Anp*IBP was determined at 1.9 Å resolution using a molecular replacement method utilizing *Col*IBP (PDB code: 3WP9) as a structural template [125]. An asymmetric unit contains six *Anp*IBP molecules (Figure 2.4). The final model of *Anp*IBP shows the structural coordinates of 203 out of 216 amino acid residues. Statistics of the data collection and the parameter values used in the refinement process are summarized in Table 2.1. The structure of *Anp*IBP consists of a 45-Å-long β -helical fold with a triangular cross section (Figure 2.5.A). The main constituents are 6-ladder β -helical loops, which are supported by a long α -helix located along the β -helical axis. The β 1 loop following the N-terminal segment (blue) was aligned next to the β 6 loop following the C-terminus (red), and they are assembled in a “head-to-tail” manner. As a consequence, the six β -helical loops are irregularly assembled in the order β 1– β 6– β 5– β 4– β 3– β 2.

Such an irregularly ordered β -helical arrangement has been found in other microbial IBPs containing the DUF3494 domain, such as *Col*IBP [125], *Tis*IBP [136], and *Efc*IBP [139]. The β -helical loops of *Anp*IBP are different in length: β 1, G12–G29 (18); β 6, A184–Q201 (18); β 5, N166–G183 (18); β 4, N145–G165 (21); β 3, S117–A144 (28); and β 2, A93–A116 (23). The lengths of the β 2-, β 3-, and β 4-loops are 3- to 10-residues longer than those of the others (β 1-, β 5-, and β 6-loops). The three surfaces of the triangular β -helical domain are named the A-, B-, and C-faces (Figure 2.5.B). The A-face is partially covered by the long α -helix, whereas the other

two surfaces are exposed to solvent. As with other microbial IBPs [97,105], there are two hydrophobic cores in *AnpIBP*. One comprises the central area of the β -helical domain, which is contributed by aliphatic residues originated from the $\beta 1$ – $\beta 6$ – $\beta 5$ – $\beta 4$ region and aromatic residues from the $\beta 2$ – $\beta 3$ – $\beta 4$ region. A segment from D30 to I52 stacked on the $\beta 1$ -loop does not satisfy the property of β -folds and was assigned as a loop region, protruding aliphatic side chains toward the inner core of the β -helical domain and acting as a capping structure to stabilize the overall structure. Another hydrophobic core is formed at the interface between the A-face and a long α -helix.

The crystal structure shows that D55, whose original residue is N55 modified with a glycan, is located at the C-terminal end of the long α -helix and is far distant from the B-face containing the IBS. The TH activity of N55D is identical to that of the wild-type, confirming the previous indications that the glycan is not involved in ice binding [115]. The C-terminal region (A204–V216) is longer than that of other microbial IBPs. In the crystal structure of *AnpIBP*, the C-terminal region was not identified because of the weak electron density, suggesting that it is flexible. Similar additional segments at the N- or C-terminal end have sometimes been identified in the DUF3494 microbial IBPs, though their functions are not clear. The C-terminal segment of *AnpIBP* contains basic residues (K206, R209, K212, and K215) at equal intervals, which sandwich several hydrophobic residues. The role of this C-terminal segment is unknown. The overall structural motif of *AnpIBP* is highly similar to that of other IBPs from bacteria, despite their phylogenetic distance. This finding is in good agreement with the previous indications that Antarctic ascomycetes acquired *AnpIBP* from bacteria through horizontal gene transfer [115].

Table 2.1. Data collection and refinement statistics for wild-type *AnpIBP* and S153Y.

Crystal	AnpIBP (7BWX.pdb)	AnpIBP_S153Y (7BWY.pdb)
<i>Data collection</i>		
Beam line	Photon Factory BL-17A	
Wavelength (Å)	0.9800	
Space group	<i>P</i> 2 ₁ 2 ₁ 2	<i>P</i> 3 ₂ 21
Unit-cell parameters (Å)	<i>a</i> =86.43, <i>b</i> =208.28, <i>c</i> =100.78	<i>a</i> = <i>b</i> =92.31, <i>c</i> =22.67
Resolution range (Å) ^a	47.62-1.90 (2.01-1.90)	46.10-2.02 (2.06-2.02)
<i>R</i> _{merge} ^{a,b}	0.107 (0.467)	0.083 (1.654)
Observed reflections	944254	1442200
Independent reflections	141990	72989
Completeness (%) ^a	99.9 (99.6)	99.9 (99.8)
Multiplicity ^a	6.7 (6.6)	19.8 (19.6)
$\langle I/\sigma(I) \rangle$ ^a	12.9 (4.2)	21.1 (2.2)
<i>Refinement</i>		
Resolution range (Å) ^a	47.62-1.90 (1.95-1.90)	45.72-2.02 (2.07-2.02)
<i>R</i> factor ^{a,c}	0.135 (0.194)	0.179 (0.424)
Free <i>R</i> factor ^{a,c,d}	0.164 (0.216)	0.216 (0.418)
R.M.S bond lengths (Å)	0.013	0.011
R.M.S bond angles (°)	1.695	2.081

^a Values in parentheses are for the highest resolution shell.

^b $R_{\text{merge}} = \sum \sum_j | \langle I(h) \rangle - I(h)_j | / \sum \sum_j \langle I(h) \rangle$, where $\langle I(h) \rangle$ is the mean intensity of a set of equivalent reflections.

^c $R \text{ factor} = \sum | |F_{\text{obs}}(h)| - |F_{\text{calc}}(h)| | / \sum |F_{\text{obs}}(h)|$, where F_{obs} and F_{calc} are the observed and calculated structure factors, respectively.

^d Randomly chosen 5.0% of the reflection data were used to calculate free R factor (Brunger AT, 1992, Nature 355, 472-475 [133]).

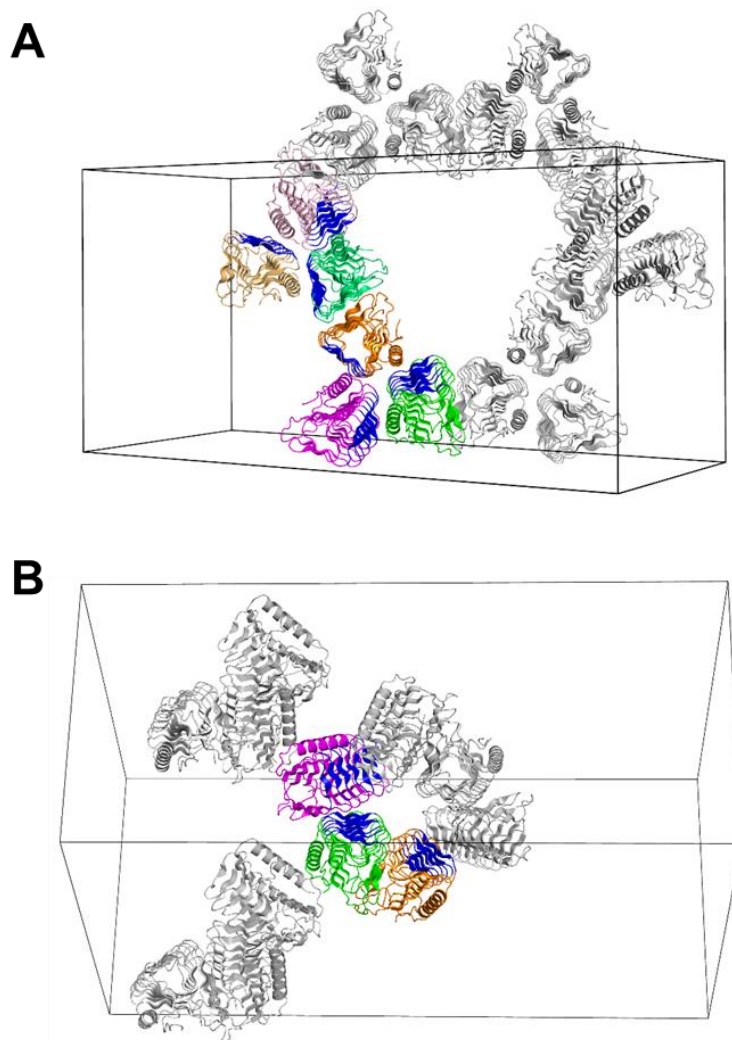


Figure 2.4. Crystal packings of wild-type *AnpIBP* and its mutant (S153Y).

Figure 2.4.A shows the molecular packing in wild-type *AnpIBP* crystal, which were crystallized in space group $P2_12_12$. Six monomers of *AnpIBP* in the asymmetric unit of the cell are drawn with color. IBS residues are colored blue. Neighboring molecules which are related by the crystallographic symmetry operations are drawn with gray. A unit cell is represented by black lines. **Figure 2.4.B** shows the molecular packing for the S153Y mutant in the space group of $P3_22_1$. Three molecules in the asymmetric unit and neighboring molecules are drawn with the same color scheme as for the wild-type. For both wild-type *AnpIBP* and S153Y mutant, IBS residues are almost free from the molecular contacts and exposed toward the solvent. The figures were generated by PyMOL.

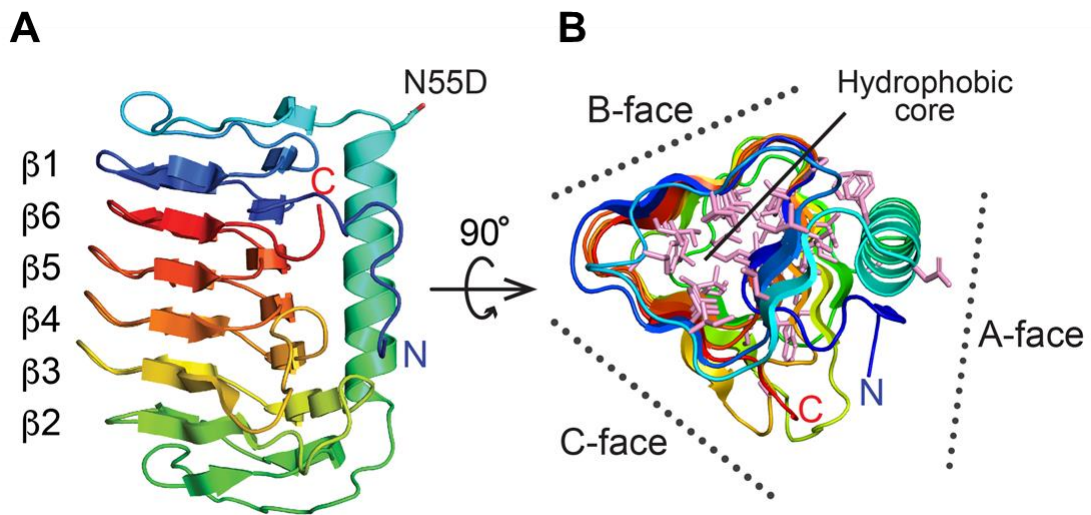


Figure 2.5. The crystal structure of *AnpIBP* (7BWX.pdb).

(A) Overall structure of *AnpIBP* represented with ribbon model colored in gradation from blue (N-terminus) to red (C-terminus). The six β -helical loops are irregularly aligned in the order $\beta 1$ – $\beta 6$ – $\beta 5$ – $\beta 4$ – $\beta 3$ – $\beta 2$. (B) Structural view of *AnpIBP* along the β -helical axis, showing that the β -helical fold is a triangular shape on which the A-, B-, and C-faces are defined. A large hydrophobic region is present at the center of the triangle. The long α -helix is stabilized on the A-face through additional hydrophobic cores.

2.4.3. The IBS of *AnpIBP* located on the B-face

To identify the IBS location of *AnpIBP*, we prepared a mutant protein in which the T58 on the A-face (Figure 2.6.A) was replaced with tyrosine (denoted T58Y) and examined its TH activity. The S153 and T156 on the B-face were also replaced with tyrosine, and the TH value was measured. The Y131 on the B-face was further replaced with threonine. Figure 2.6.B shows the TH activity of *AnpIBP* (wild-type) and its four mutant proteins: T58Y, Y131T, S153Y, and T156Y. They showed a typical linear dependence of TH on the square root of concentration. The wild-type had 0.63°C of maximal TH activity at a concentration of 250 μM. The T58Y that mutated on the A-face exhibited a similar dependence to the wild-type. Mutations in S153Y and T156Y on the B-face resulted in a decrease in activity to 17% of the wild-type. These results suggest that the IBS of *AnpIBP* is on the B-face. The Tyr131 located on the B-face protrudes a bulky side chain, which may cause steric hindrance when the B-face binds to an ice crystal. Hence, we expected TH to be increased for Y131T, because threonine is a typical ice-binding residue for most IBPs. However, the mutation affected neither TH nor the ice-shaping abilities, indicating that Y131 is located in such a way as to maintain the ice-binding ability. To confirm that there was no significant influence of these mutations on protein folding, we performed circular dichroism (CD) measurements (Figure 2.7.). The wild-type (*AnpIBP*) exhibited minimum ellipticity at 217 nm and maximum ellipticity at 197 nm on the CD spectra, suggesting a β-helical structure. The same profile was reported for other microbial IBPs [125,136]. All *AnpIBP* mutants exhibited highly similar CD profiles to the wild-type, suggesting that defective mutations did not affect the overall structure but collapsed a structure needed for ice binding on the B-face.

To further investigate the ice-binding properties of the defective mutants, we observed their ice-shaping ability and FIPA pattern (Figure 2.6.C,D). It has been demonstrated that the morphology of a single ice crystal showed a lemon shape in hyperactive IBPs exhibiting 5–6°C

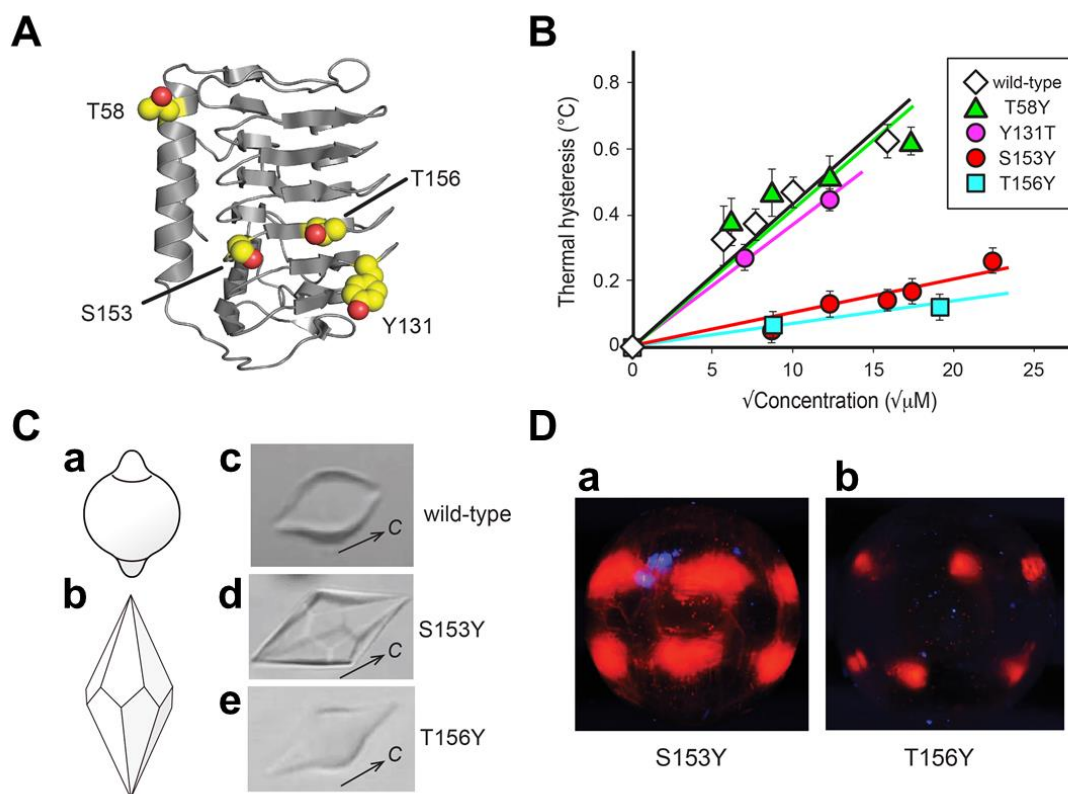


Figure 2.6. Effect of amino acid replacement on the ice-binding ability of *AnpIBP*.

(A) Mutation sites on the crystal structure of *AnpIBP*. The side chains of the wild-type residues are shown as spheres. T58 is located on the A-face and the others on the B-face. (B) Thermal hysteresis activities (°C) of *AnpIBP* and its mutants plotted against the square root of each concentration. (C) Morphologies of a single ice crystal observed for *AnpIBP* and its mutant solutions. Illustrations show a lemon-shape ice crystal (a) observed for hyperactive IBPs and a bipyramidal ice crystal (b) observed for moderately active IBPs. The wild-type *AnpIBP* showed a lemon-shaped ice crystal (c), whereas the defective mutants (S153Y and T156Y) showed crystal bipyramids (d and e). (D) Comparison of FIPA patterns between the S153Y and T156Y mutants of *AnpIBP*. The orientation of these ice crystal hemispheres are the same as in Figure 2.3.B,D. These mutants lost the ability to bind to the prism ring.

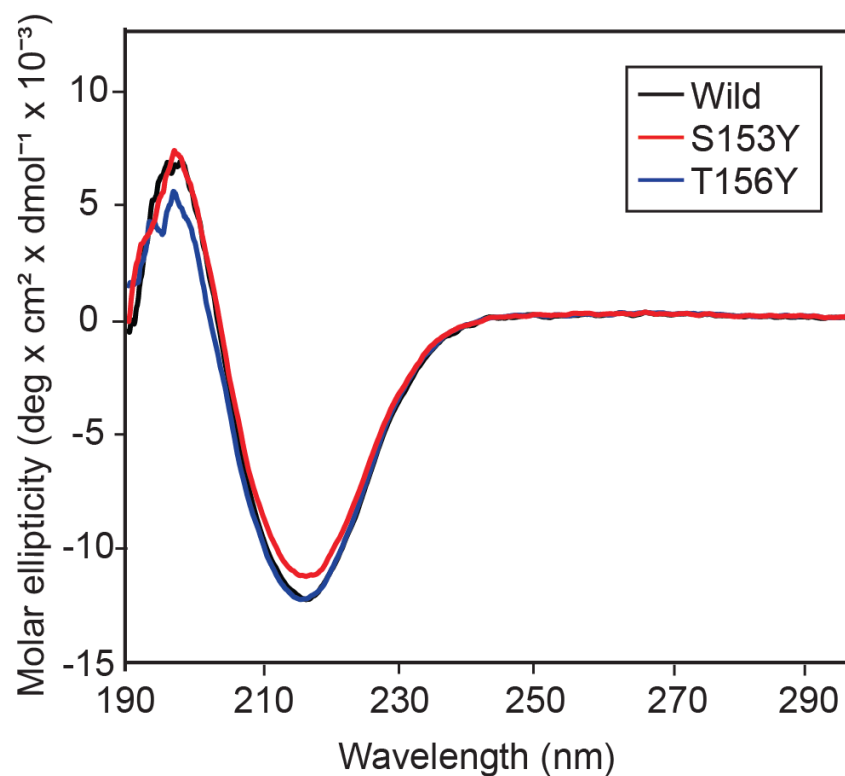


Figure 2.7. CD spectra of wild-type *AnpIBP* and its mutants (S153Y and T156Y).

Circular dichroism (CD) spectra of *AnpIBP* wild-type and its mutants (S153Y and T156Y). The CD spectra were measured by with a J-720 spectropolarimeter (Jasco, Tokyo, Japan) with a quartz cuvette of 0.1 cm optical path length. *AnpIBP* and its mutants were dissolved in 10 mM sodium phosphate buffer (pH 7.4). Spectral data were collected from 190 and 260 nm at room temperature. We repeated the scans four times, and the averaged values were plotted.

of TH activity, such as insect-derived IBPs (Figure 2.6.Ca). In contrast, a hexagonal bipyramid is created in moderately active IBPs exhibiting approximately 1°C of maximal TH, such as fish-derived IBPs (Figure 2.6.Cb). *Anp*IBP is categorized as a moderately active IBP based on its TH value (Figure 2.6.B). However, a single ice crystal in *Anp*IBP solution represented a lemon-like shape (Figure 2.6.Cc) as observed previously [115], suggesting that *Anp*IBP can also bind to multiple ice planes although its manner will not be perfectly the same as the hyperactive IBPs. In contrast, the defective mutant S153Y generated a hexagonal bipyramid, as produced by fish IBPs (Figure 2.6.Cd). Another mutant, T156Y, also produced a hexagonal bipyramid, although it is not clearly faceted (Figure 2.6.Ce). In FIPA analysis, the illumination of S153Y was observed in six patches at the middle latitude of the ice hemisphere (Figure 2.6.Da). This result indicates that the S153Y mutant loses the binding affinity to the prism ring, as it occupies the equator. The illumination area of T156Y was further reduced (Figure 2.6.Db) in comparison with that of the S153Y mutant, suggesting a significant loss of binding ability. These results suggest that Ser153 and Thr156 on the B-face are the residues necessary to bind to the water molecules constructing the prism ring of a single ice crystal hemisphere.

2.4.4. Ice-like polygonal water networks were observed on the IBS of *Anp*IBP

The data presented here indicate that the IBS of *Anp*IBP is constructed on the B-face, similar to other microbial IBPs [103]. On the basis of the known IBS construction, its location in *Anp*IBP was hypothesized to be in the area surrounded by a blue line in Figure 2.8.A. The size of this IBS—the solvent-accessible area—is approximately 1,418 Å², slightly larger than the 921 Å² estimated for IBS on *Tis*IBP [97]. The amino acid residues that participate in the IBS are also shown in Figure 2.8.A. The Thr and Ser are indicated in yellow, and the charged residues are in green. A four-residue segment stacked on the β1-loop and six-residue segments of six-stranded

parallel β -sheets are the candidate ice-binding residues: T36-S-I-T39 (loop region), Q17-G-V-A-N-A22 (β 1), S189-A-V-T-L-D194 (β 6), A171-L-I-A-A-Q176 (β 5), S153-S-A-T-L-G158 (β 4), T126-T-L-V-T-Y131 (β 3), and S100-A-V-G-L-D105 (β 2). For each β -loop, the side chains of four residues are directed outward, whereas two residues are directed inward, leading to an out–out–in–out–in–out pattern similar to that identified in *Tis*IBP6 and *Col*IBP [97,125].

Some of the DUF3494 IBPs are composed of repetitive amino acid sequences. For example, *Ff*IBP, a hyperactive IBP, has repetitions of the consensus sequence –T–A/G–X–T/N [138]. A slightly different *Efc*IBP also contains the repetitive sequence –T–X–T or T–X–D and is categorized as a moderately active IBP [139]. In the IBS amino acid sequence of *Anp*IBP, there is no such repetitive sequence. The outward-pointing residues on the IBS of *Anp*IBP contain relatively small hydrophobic side chains, such as alanine, glycine, serine, and threonine, which share 70% of the total IBS. The residues shown in columns 1, 2, and 4 (Figure 2.8.A, right) are hydrophobic residues, whereas column 6, at the edge, contains charged groups. A hydrophobic surface containing spaced hydroxyl groups is a typical feature of IBS and is thought to be key to locating the ice-like clathrate water molecules on that site.

It has been shown that hydration water molecules on an IBP are relevant to its ice-binding function. We examined such water molecules located on the crystal structures of *Anp*IBP and the S153Y mutants. In crystals of *Anp*IBP and S153Y, the asymmetric unit contained six molecules and three molecules, respectively (Figure 2.4.). Among the six *Anp*IBPs, half of the IBSs were covered by another protein, whereas the other half was exposed to the solvent. This is due to the hydrophobic nature of IBSs, which tend to align face to face in an asymmetric unit [140]. We found that approximately 150 water molecules are located beside three molecules of *Anp*IBP that are closely assembled in the crystal. These water molecules mostly form pentagonal or hexagonal structures. These structures are called “semi-clathrate water networks” and are initially found in

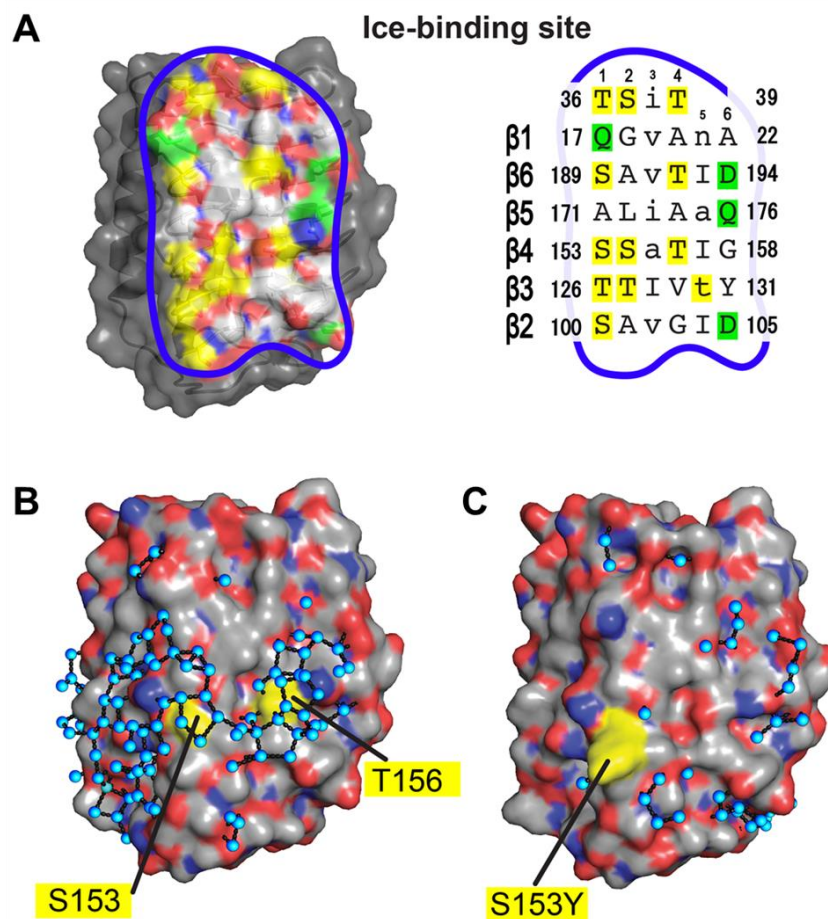


Figure 2.8. Surface models of the present determined structures of *AnpIBP* (7BWX.pdb) and its mutant (7BWY.pdb).

(A) An ice-binding site (IBS) constructed on the B-face of *AnpIBP* (wild-type) whose area is indicated by a blue line. The capitals in columns 1, 2, 4, and 6 represent the outward-pointing residues, mostly Thr and Ser (yellow). The small characters in columns 3 and 5 are inward-pointing residues, mostly hydrophobic residues. The polar residues are aligned in column 6 (green). (B) Surface model of wild-type *AnpIBP* in the same orientation as (A), where gray, red, and blue show the hydrophobic, positively charged, and negatively charged residues, respectively. The black rods connect the oxygen atoms of the hydration waters (cyan) proximal to each other within 3.5 Å, the maximum allowed distance for a hydrogen bond [140,141]. Many hydration water molecules are circled and organized into polygonal geometry on the IBS. (C) Surface model of the crystal structure of the S153Y mutant whose ice-binding ability was lowered. The polygonally arranged water molecules were not detected on the IBS.

a hyperactive fish type I IBP called Maxi [66,107]. In Maxi, approximately 400 water molecules participate in the water networks, which extend from a core region to the outside of the four-helix bundle structure. When we identified the water molecules whose oxygen atoms are proximal to each other within 3.5 Å to be connected with a hydrogen bond [141,142], a total of 88 water molecules were displayed on the solvent-exposed IBS (Figure 2.8.B). The molecules are mainly organized into polygonal arrangements similarly to those observed in Maxi, which extend over the left and right sides of the IBS in *Anp*IBP. There are at least 13 polygons on the IBS of *Anp*IBP, which are mainly located around S153 and T156. Such ice-like polygonally arranged water molecules were not identified on the solvent-exposed IBS of a mutant, S153Y (Figure 2.8.C), whose TH activity and ice-binding ability were lowered (Figure 2.6.C,D). Molecular dynamics calculations of ice growth kinetics suggest that the growth front of an ice crystal forms a unique layer composed of semi-clathrate waters that change between liquid and solid intermediate states [143,144]. This growth front is named a “quasi-liquid layer” and is assumed to be an initial target of IBP when making an IBP–ice complex. The polygonal water networks of *Anp*IBP are assumed to merge with this quasi-liquid layer, leading to the location of the host (*Anp*IBP) on the surface of an ice crystal. This mechanism facilitates rapid association of IBP to ice crystals and has been proposed for several other IBPs that accompany the polygonal water networks.

2.4.5. Ice-binding mechanism of *Anp*IBP

Figure 2.9.A,B shows a single ice crystal hemisphere formed in a solution and its constituent water molecules organized into hexagonal arrangement, respectively. Figure 2.9.A illustrates the location of the prism ring as observed for *Anp*IBP, as well as the basal plane. The basal plane is the polar area of the spherical ice corresponding to the top surface of the hexagonal ice (Figure 2.9.B). The location of the primary and secondary prism planes (white squares) and

the oxygen atom spacing of the basal, primary prism and secondary prism planes (expanded views) are indicated in Figure 2.9.B.

It has been shown that several IBPs have regular arrays of hollows on their surface [29]. They are sometimes vacant in the crystal structure due to crystal packing. They are thought to trap the hydration water molecules so that they are located at regular intervals [42,84]. For such arrayed water molecules, an anchoring role to bind the host protein (IBP) to ice crystal plane(s) has been hypothesized. For example, an insect-derived *Tm*IBP has six arrayed hollows on its IBS to trap water molecules (Figure 2.9.C). This IBP consists of tandem repeats of 12 consensus sequences containing a tripeptide “TCT”, where T is Thr and C is Cys. In this motif, two ranks of six Thr residues are exposed outside and Cys residues are oriented inside. This out–in–out arrangement of TCT is stacked on the β -helical domain, leading to the formation of hollows in which to locate six regularly arrayed water molecules (Figure 2.9.C). An original ice-binding model of *Tm*IBP was that the two ranks of Thr function in ice binding, because the two-dimensional spacing between their side-chain hydroxyl groups shows complementary matches to the oxygen atom spacings of the primary prism and basal planes [84]. *Tm*IBP, however, binds to all of the ice planes besides the primary prism and basal planes. Figure 2.9.C shows that the hollows are present at 4.6- and 13.8-Å intervals, closely matching the oxygen atom spacings of the basal plane (Figure 2.9.B). This observation is consistent with *Tm*IBP binding to the basal plane. Because the oxygen atom distance of 4.6 ± 1.0 Å has been identified for all planes of a single ice crystal, the presence of surface-trapped oxygen atoms separated by 4.6 Å might be key to binding to the oxygen atoms constructing many ice planes.

The presence of four regularly arrayed hollows was identified in the IBS of *Anp*IBP (Figure 2.9.D). Unlike *Tm*IBP, these hollows are not flanked by ranks of Thr, as the IBS of *Anp*IBP does not consist of a tandem repeat sequence. The segments organized into out–out–in–out–in–out

arrangement stacked on the β -helical domain create these hollows with regular intervals. The distance between the first and second hollows and between the third and fourth hollows is 4.6 Å, and that between the first and third hollows and between the second and fourth hollows is 14.7 Å (Figure 2.9.D). These intervals perfectly match the oxygen atom distance in the primary and secondary prism planes (4.6 and 14.7 Å) as well as that comprising the prism ring. The 4.6 Å atom spacing is common for many ice planes, whereas 14.7 Å is only specific to the prism planes. We assume that such a rigorous water atom spacing is located on the prism planes but not on the basal plane. Figure 2.9.E shows an additional surface model of a microbial IBP denoted *Tis*IBP6 [97]. This is also composed of a β -helical domain that includes the out-out-in-out-in-out segments and exhibits the ability to bind to whole ice crystal planes. The hollows on this IBP are separated by 4.6 Å, and the 14.7 Å interval does not exist between these water molecules.

The *Anp*IBP has the polygonally arranged ice-like water molecules on its IBS (Figure 2.8.B), which are assumed to have an anchoring role by merging with the quasi-liquid layer constructing an ice crystal surface, which is more ordered than bulk water molecules, but less ordered than those in the hexagonal ice lattice [145,146]. The polygonally arranged water molecules are assumed to assist the *Anp*IBP in immersing into the quasi-liquid layer, which may locate the IBS in close proximity to the water molecules of the solid ice lattice. This structure facilitates subsequent *Anp*IBP binding to the latticed water molecules separated by 14.7 Å that are specifically involved in the prism ring. A similar, but not identical arrangement of water molecules was observed on a fish type III IBP (*nfe*IBP6 and its mutant) [109]. This IBP also has polygonally arranged water molecules but does not exhibit hollows on that surface. Instead, several water molecules that participate in the polygonal water network exhibit a perfect position match to their target ice planes (primary and pyramidal ice planes). The insect-derived IBPs, such as *Tm*IBP, have regularly arrayed hollows, but they do not accompany a polygonally arranged

water network [84]. The other IBPs that have polygonal water networks do not have arrayed hollows on their surface [106,108]. Therefore, *AnpIBP* is the first example to both have polygonally arranged water molecules and have hollows to tightly trap the surface water molecules at regular intervals, allowing the binding of this IBP only to water molecules separated by 14.7 Å, which form the prism ring. The fish type III IBP also accompanies the surface-bound waters [109], which are not linearly aligned but are two-dimensionally organized. This may cause its specific binding to only the primary prism plane and a pyramidal plane. The growth speed of the prism planes is approximately 100 times faster than that of the basal plane [20]. *AnpIBP* binding to the prism planes effectively inhibits this fast growth, which protects the host organism (*A. psychrotrophicus*) from ice injuries.

To summarize, the present study determined the target ice planes and X-ray crystal structures of the wild-type and a defective mutant of *AnpIBP*. The *AnpIBP* uniquely binds to the water molecules that participate in the primary and secondary prism planes, which were detected as a prism ring in the FIPA experiment. Both the ice-like polygonally arranged water molecules and a row of four hollows to trap the surface water molecules exist on the IBS of *AnpIBP* and perfectly match the oxygen atom spacings (4.6 and 14.7 Å) of the prism ring. The presence of oxygen atoms separated by 14.7 Å should be key to recognizing the prism ring, whereas four trapped water molecules will bind *AnpIBP* tightly onto the prism ring. These results suggest that *AnpIBP* is fine-tuned to merge with the ice–water interface of an ice crystal through polygonally arranged water molecules and then bind to specific water molecules constructing the prism ring through the water molecules trapped in the four hollows.

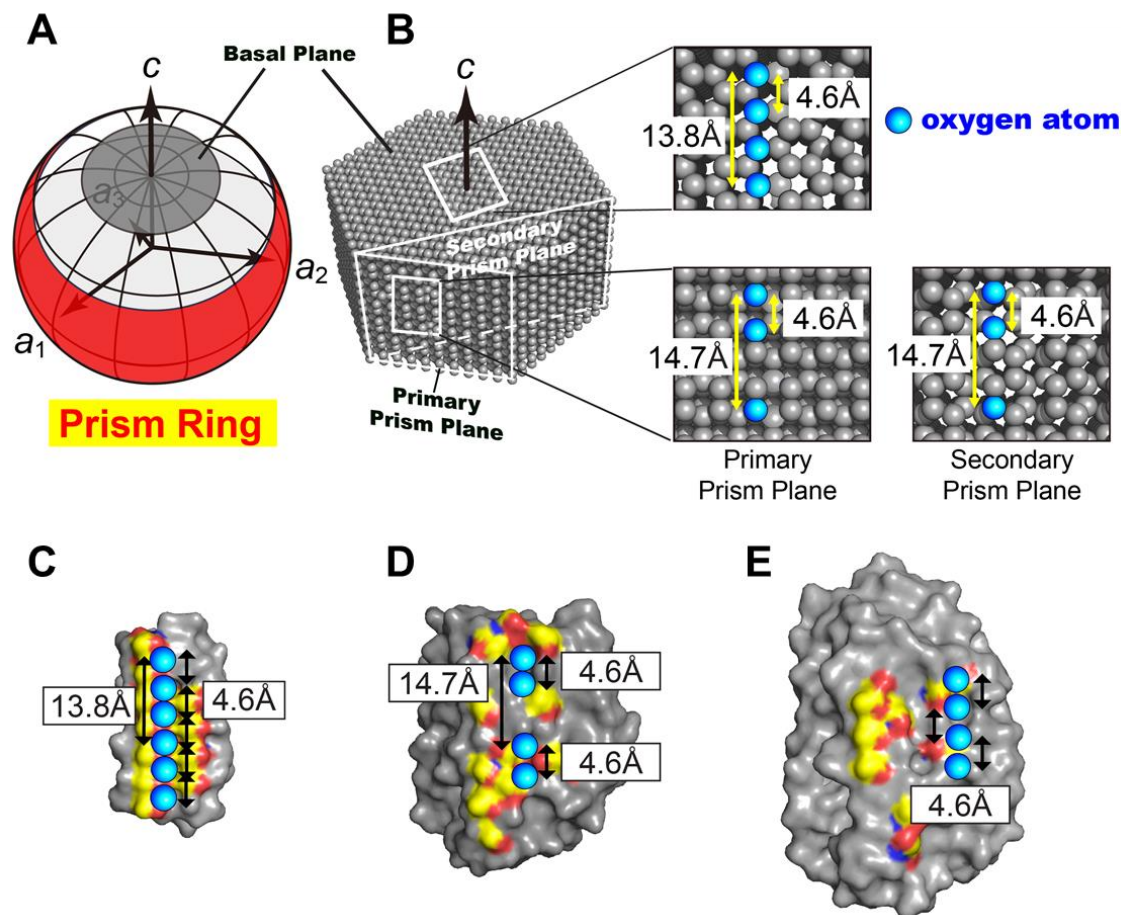


Figure 2.9. Oxygen atom spacings of a single ice crystal and IBPs.

(A) Illustration of the prism ring, indicating the *Anp*IBP-bound area on a single ice crystal hemisphere. (B) Hexagonally arranged water molecules that are the constituents of the single ice crystal hemisphere. Only the oxygen atoms are indicated. The basal plane is the top surface of (A,B). The oxygen atoms separated by 4.6 and 14.7 Å are unique constituents of the primary and secondary prism planes as well as the prism ring. (C) IBS of *Tm*IBP has six hollows to trap the water molecules (cyan) at regular intervals. They show a close match to the O-atom distances of the basal plane (4.6 and 13.8 Å). (D) Four linearly arrayed hollows observed on the IBS of *Anp*IBP to trap the water molecules. Their intervals perfectly match the distance between the oxygen atoms comprising the prism ring (4.6 and 14.7 Å). (E) Hollows with 4.6-Å intervals observed on *Tis*IBP6, which possesses the ability to bind to multiple ice planes.

Chapter 3: Discovery of hyperactive IBP
from *Dorcus hopei binodulosus*

Preface: This chapter was published in International Journal of Molecular Science: Arai, T.*, Yamauchi, A.*, Miura, A., Kondo, H., Nishimiya, Y., Sasaki, Y.C. and Tsuda, S. (2021) Discovery of hyperactive antifreeze protein from phylogenetically distant beetles questions its evolutionary origin. * Two authors are equally contributed to this study.

3.1. Abstract

Beetle hyperactive ice-binding protein (IBP) has a unique ability to maintain a supercooling state of their body fluids, however, less is known about its origination. Here we found that a popular stag beetle *Dorcus hopei binodulosus* (*Dhb*) synthesizes at least 6 isoforms of hyperactive IBP (*Dhb*IBP). Cold-acclimated *Dhb* larvae tolerated -5°C chilled storage for 24 hours and fully recovered after warming, suggesting that *Dhb*IBP facilitates overwintering of this beetle. A *Dhb*IBP isoform (~ 10 kDa) appeared to consist of 6–8 tandem repeats of a 12-residue consensus sequence (TCTxSxNCxxAx), which exhibited 3°C of high freezing point depression and the ability of binding to an entire surface of a single ice crystal. Significantly, these properties as well as DNA sequences including untranslated region, signal peptide region, and an IBP-encoding region of *Dhb* are highly similar to those identified for a known hyperactive IBP (*Tm*IBP) from the beetle *Tenebrio molitor* (*Tm*). Progenitor of *Dhb* and *Tm* was branched off approximately 300 million years ago, so no known evolution mechanism hardly explains the retainment of the DNA sequence for such a long divergence period. Existence of unrevealed gene transfer mechanism will be hypothesized between these two phylogenetically distant beetles to acquire this type of hyperactive IBP.

3.2. Introduction

Stag beetles include approximately 1,200 species of insects belonging to the family *Lucanidae*, characterized by a pair of long horns, which resemble antlers of a stag, protruding from the mandibles of the male (Figure 3.1.A) [120,147]. The stag beetles established immense popularity in Japan [148,149] as evidenced by cartoons, trading card games, fan websites, or the Japanese Samurai helmet in the 1500s, which was decorated with an ornament called “Ku wagata” designed after the stag beetle (Figure 3.2.). Among them, *Dorcus hopei binodulosus* (*Dhb*) (Figure 3.1.A,B) is especially popular because of its stout large body [121]. The *Dhb* beetle is found in northeastern China, Korea, and Japan that has an icy winter season, while it uniquely possesses a long-life overwintering nature; larvae live for 1–2 years until pupation in a rotten tree or underground, and the adult lives for 3–5 years on the ground [120,121]. Because hyperactive ice-binding protein (IBP) discovered in fishes, insects, and bacteria is known to facilitate their cold-survival [22], we speculated whether the *Dhb* beetle produces this protein in its body fluids. Since only four beetles, namely *Tenebrio molitor*, *Dendroides canadensis*, *Anatolica polita*, and *Microdera punctipennis*, are known to synthesize hyperactive IBP composed of a consensus sequence [82,117–119] and all of them belong to the same superfamily *Tenebrionoidea*, less is known about the origins of this protein, while the *Dhb* beetle belongs to a different superfamily *Scarabaeoidea* [120]. Therefore, if *Dhb* contains hyperactive IBP, the discovery provides a first clue to understanding the origin of this protein as well as new resources (i.e., stag beetles) to explore more new species of hyperactive IBP.

Aqueous solutions that remain in liquid phase by lowering the temperature below the melting point are called supercooled solutions, in which numerous “embryo” ice crystals are present dispersively [39,150]. When the temperature is further lowered and thermal movement of embryo ice crystals decreases, they aggregate rapidly to form a large cluster to nucleate numerous

ice particles, thereby changing the water molecules into a multi-crystalline state, which is the general ice crystal structure. Note that a substance other than water molecules sometimes catalyzed the aggregation process [39]. The overwintering, cold-adapted insects have long been known for their ability to stabilize such a supercooled state of their body fluids at subzero temperatures, leading to protection from freezing [151]. The supercooled state, or semi-frozen state, is also stabilized with low molecular weight solutes in the body fluids, such as polyhydroxy alcohol (ex. glycerol), sugars (ex. trehalose), amino acids (ex. proline), and/or glycolipids. Insects that equip such cold-survival mechanisms are called freeze-avoidance species, which cannot recover once their body fluids is frozen entirely. In contrast, freeze-tolerant species can recover from the freezing of their body fluids, though usually only extracellular fluids are thought to be frozen by secreting proteinaceous ice nucleators that protects inside of cells from freezing [151]. The hyperactive IBP synthesized in the freeze-avoidance insects strongly arrests the growth of embryonic single ice crystals generated in supercooled water [82]. This mechanism indeed prevents aqueous solutions from freezing down to approximately -5°C . This protein is therefore regarded as a novel cryoprotectant to realize quality preservation of vaccines, cells, and organs around -5°C without formation of ice blocks [13]. Note that the IBP's ability to stabilize the supercooling state is evaluated by a difference between freezing and melting points of the IBP solution, which is called thermal hysteresis (TH) [29].

The hyperactive IBP, *Tm*IBP, was first identified in 1997 from the hemolymph of the beetle *T. molitor* (*Tm*), which exhibited a significant TH activity ($\sim 5^{\circ}\text{C}$) [82]. *Tm*IBP is a mixture of nine isoforms (MW = 8.4–12 kDa), consisting of 7–11 tandem repeats of a 12-residue consensus sequence, namely TCTxSxNCxxAx, where x is any amino acid residue [83]. A homologous IBP isoform (*Dc*IBP), containing the “TCT sequence,” was identified from another beetle *D. canadensis* that shares 46%–66% sequence identity with *Tm*IBP isoforms, and is composed of the

same 12-residue sequence repeats with occasional insertions of additional amino acids [151]. This 12-residue sequence is not identified in neither fish-, plant-, fungi-, nor bacteria-derived IBP. The spruce budworm *Choristoneura fumiferona* is not a beetle, but synthesizes IBP (SbwIBP, Mw = 9 kDa) composed of the TxT sequence (x is variable) and exhibits a high TH activity (5°C) [42]. Extensions of TxT, such as TxTxTxT, were identified for other hyperactive IBPs from the longhorn beetle *Rhagium inquisitor* (RiIBP, Mw = 12.8 kDa) [85] and the inchworm of the geometer moth *Campaea perlata* (iwIBP, Mw = 3.5–8.3 kDa) [88]. Hence, TxT is considered a key structural motif for significant TH activity. The IBP from snow flea *Hypogastrura harveyi* Folsom (sfIBP, Mw = 6.5–15.7 kDa) [89], a primitive arthropod with six legs and no wings, is an exception. It consists of a repetitive glycine-rich sequence instead of TxT, which also exhibits high TH activity (5.8°C).

We repeatedly bred *Dhb* beetle for years to obtain the final (3rd) instar larvae, which were used for cold-survival experiments and detection of hyperactive IBP synthesis in their hemolymph. We found that *Dhb* larvae tolerate –5°C -chilled preservation for 24 hours and synthesize at least six isoforms of hyperactive IBP (*Dhb*IBPs), for which we performed mitochondrial DNA & amino acid sequence analysis, recombinant-protein preparation, TH activity measurement, structural modeling, and phylogenetic analysis. Significantly, all the data obtained for *Dhb*IBP exhibited significant similarity to those identified for a known hyperactive IBP from a phylogenetically distant beetle, the *T. molitor* (*Tm*IBP).

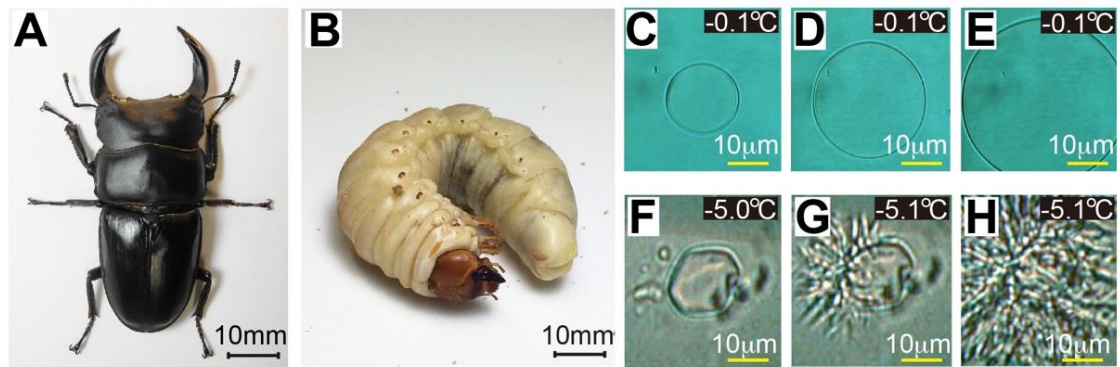


Figure 3.1. A stag beetle *Dorcus hopei binodulosus* (*Dhb*) and a bursting ice-crystal growth observed for its hemolymph at the freezing point.

(A) An adult form of *Dhb* and (B) its final instar larva. The adult is uniquely equipped with a pair of antlers like a stag. (C) A photomicroscope image of a single ice crystal in ordinary supercooled water (-0.1°C), which shows a rounded disk-like morphology. (D–E) The disk expanded when the temperature was held, implying that there is no antifreeze substance. (F) A photomicroscope image of a single ice crystal prepared in larval hemolymph, which kept unchanged even if the temperature was changed between -5.0°C and 0°C because of the ice-binding of hyperactive IBPs. The hyperactive IBP-bound ice crystal is uniquely modified into a lemon-like shape. (G) Bursting ice growth occurred from a tip of the lemon crystal when it further lowered the temperature to freezing point (-5.1°C). (H) The bursting ice growth continues to show a vein-like pattern, which is also a known phenomenon for hyperactive IBPs.

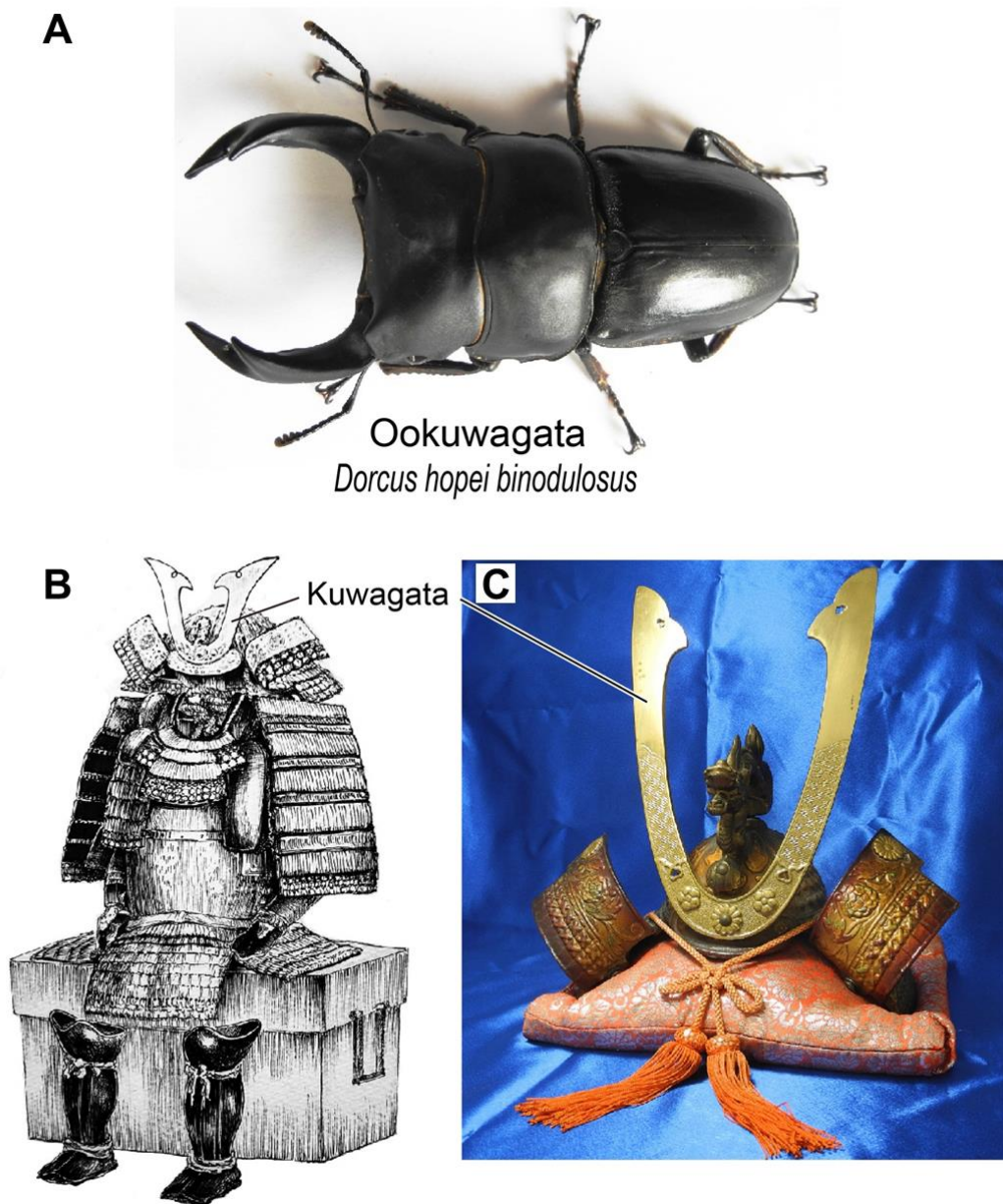


Figure 3.2. Popularity of the stag beetle in Japan.

(A) A photograph of the stag beetle *Dorcus hopei binodulosus* (♂), “Ookuwagata” in Japanese, where “Oo” means giant. (B) An example of an armor protection suit for the Japanese warrior “Samurai” in the 1,500s, illustrated by Tsuda. The helmet is decorated with a pair of antlers called “Kuwagata,” which was designed after the stag beetle to symbolize the toughness and power of the samurai wearing the suit. (C) A photograph of a replica of the samurai helmet decorated with Kuwagata, owned by an author (Miura).

3.3. Materials and methods

3.3.1. Construction of cDNA library from *Dhb* larva

A final instar larva of the stag beetle *Dorcus hopei binodulosus* (*Dhb*) acclimated at 10°C was flash frozen with liquid nitrogen and homogenized with a mortar and pestle. The homogenate suspension (200 mg) was prepared using TRI reagent (2 mL, MERCK, Darmstadt, Germany) and QIAshredder (QIAGEN, Hilden, Germany). After removing the insoluble fraction from the suspension by centrifugation at $11,000 \times g$ for 20 min, chloroform (400 μ L) was added to the supernatant to precipitate unwanted proteins and DNA. All RNAs, denoted “total RNA,” of the beetle was obtained in the aqueous phase. Total RNA was precipitated by adding 2-propanol (1 mL) and recovered with DEPC-treated water, which prevents RNA degradation. The Oligotex-dT30 mRNA Purification kit (TaKaRa, Shiga, Japan) was used to extract mRNAs from total RNA. Then, reverse transcription was performed using oligo (dT) primers and obtained mRNAs for 60 min at 42°C. This primer selectively binds the poly adenine (A) region of mRNAs, leading to the generation of single strand cDNAs (ss-cDNAs) that are complementary to mRNA sequences. The obtained ss-cDNAs were then reacted with RNase H and DNA polymerase I for 2.5 h at 16°C to form double strand cDNAs. We utilized the ZAP-cDNA synthesis kit (TOYOBO, Osaka, Japan) for these experiments. We did not know which cDNAs encode isoforms of *Dhb*IBP at this stage. To identify them in the next step, a DNA segment called “Adaptor,” whose nucleotide sequence is mentioned in the kit, was specifically ligated to 5'- and 3'-ends of each cDNA by T4 DNA ligase overnight at 8°C.

3.3.2. Sequence determination of cDNA encoding *Dhb*IBP

The cDNA sequence that encodes an isoform of *Dhb*IBP is described as follows: (I) 5'-Adap-UTR1-Met-signal sequence-*Dhb*IBP-stop codon-UTR2-poly (A)-Adap-3', where Adap,

UTR 1&2, and Met denote the Adaptor, untranslated region 1 & 2, and methionine, respectively. DNA→protein translation is initiated from Met. A mature *DhbIBP* is produced by the removal of a signal sequence located upstream (left-hand side) of the *DhbIBP* sequence. On the basis of known DNA sequences that encode hyperactive IBPs from beetles *Tenebrio molitor* and *Dendroides canadensis* (*TmIBP* and *DcIBP*) [83,117], we initially prepared the following primer: (a) 5'-TGYACTGGDGSTCYGAYTGYMVHDSKTGYAC-3' (forward primer). This primer (a) should bind to “*DhbIBP*” in the sequence (I), if it is a correct nucleotide sequence that can encode a protein whom cDNA exhibits high sequence similarity to that encoding *TmIBP* and/or *DcIBP*. We next prepared primer (b), which was designed to bind to the segment composed of “poly (A)–Adap” region in the sequence (I). (b) 5'-GAGAGAACTAGTCTCGAGTTT-3' (reverse primer). Polymerase chain reaction (PCR) was performed with primers (a) and (b) and the cDNA library (see previous paragraph) using Ex taq DNA polymerase (TaKaRa Bio Inc, Tokyo, Japan) on our PCR instrument (GeneAmp PCR system 9700, Applied Biosystems, Foster city, USA). The following reaction cycle was used: 94°C (1 min)–{94°C (1 min)–50°C (1 min)–72°C (1 min)} × 30–72°C (5 min)–4°C (hold). Various cDNAs amplified with these primers, which are the promising candidates for cDNAs encoding *DhbIBP* isoforms, were obtained using agarose gel electrophoresis (a similar example shown in Figure 3.3.G). The obtained cDNAs were ligated to the pGEM-T Easy vector (Promega, Madison, USA) using the Mighty TA-cloning Kit (TaKaRa). The resultant plasmid, including a cDNA candidate, was then transformed into competent *Escherichia coli* JM109. Following colony PCR with universal M13RV and M13M4 primers on the agarose gel, the plasmid was collected from positive clones using the QIAprep Spin Miniprep Kit (QIAGEN). We then determined their nucleotide sequence by employing BigDye™ Terminator v3.1 Cycle Sequencing Kit and ABI 3130xl Genetic Analyzer (Applied Biosystems, Foster City, CA). We found that cDNAs collected at this stage contained partial sequences,

composed of half-way portion to the stop codon–UTR2 segment, but did not include the signal sequence described in (I).

On the basis of the partial sequence of cDNA candidates that encode *DhbIBP* isoforms, we prepared the following primers: (c) 5'-TCGGGAATTCGGCACGAGG-3' (forward primer), (d) 5'-ATAGCGGCCGCGGATCCTTAATGTCCGGGACATCCTG-3' (reverse primer). Primer (c) was designed to bind to the upstream “5'-Adap” region in the cDNA sequence (I). Primer (d) binds to a region including the “stop codon–UTR2”. With these two primers, PCR performed using the cDNA library according to the procedures described in the previous paragraph. A problem in this experiment was that the primer (c) binds not only to “5'-Adap,” but also to the “Adap-3” region of the sequence (I), leading to the amplification of a large number of cDNAs. Hence, the amplified DNA fragments in the size range of 500–700 bp were purified using agarose gel electrophoresis, which was the estimated size of the cDNA encoding *DhbIBP* isoforms. Sequence analysis of our obtained samples in this time gave us revealed information, including the signal sequence, of cDNAs.

Because we could obtain information about the cDNA candidates, including the signal sequence, encoding *DhbIBP* isoforms, we prepared the following primer: (e) 5'-GGAACATATGGCATTCAAAACGTGTGCT-3' (forward primer). This primer was designed to bind to the signal sequence of cDNAs encoding *DhbIBP* isoforms, whose start codon is indicated with underlined text. Hence, final PCR was performed against the cDNA library with primers (e) and (b). The original reaction cycle was slightly modified to 94°C (1 min)–{94°C (1 min)–56°C (1 min)–72°C (1 min)} × 30°C–72°C (5 min)–4°C (hold). We obtained 650 bp PCR products in this final PCR. By employing the sequence determination procedures described in the last half of the 1st paragraph of this section, we could determine at least six nucleotide sequences encoding *DhbIBP* isoforms, which were translated into amino acid sequences shown in Figure 3.5. and 3.6.

3.3.3. Expression and purification of r*Dhb*IBP2 isoform

A codon optimized DNA sequence encoding *Dhb*IBP2 isoforms (Figure 3.5.) tagged with thioredoxin (Trx) plus six consecutive histidines (His) (r*Dhb*IBP2) was synthesized to include *Nde*I and *Not*I cleavage sites at 5' and 3' sites, respectively. Coexpression with the Trx-tag is known to facilitate expression of the beetle IBP from *Anatolica polita* [172]. We used this strategy to prepare r*Dhb*IBP2 in a similar manner. Histidine residues enabled affinity chromatography with the Ni-NTA column. Following the digestion of the two cleavage sites, the obtained DNA fragment encoding r*Dhb*IBP2 was inserted into the pET20b vector. This vector was then transformed into *E. coli* BL21 (DE3). Transformants selected on antibiotic plates were inoculated into 20 mL LB medium containing kanamycin and cultured at 37°C for 16 h. Harvested cells were transferred into LB medium (1 L) containing kanamycin and cultured at 37°C for 2–3 h. When its OD₆₀₀ value reached 0.4–0.8, the expression of r*Dhb*IBP2 was induced by isopropyl-β-D-thiogalactopyranoside (0.5 mM). The obtained cells were further cultivated at 15°C for 24 h, collected by centrifugation, resuspended in Tris-HCl buffer (0.1 M, pH 8.0) containing NaCl (0.1 M), and disrupted by sonication for 45 min. A soluble fraction of the cell lysate was obtained by centrifugation and loaded into the Ni-NTA column (QIAGEN) equilibrated with Tris-HCl (20 mM) containing NaCl (0.5 M). The r*Dhb*IBP2 was eluted by the same buffer containing 250 mM imidazole. The collected fraction was dialyzed against Tris-HCl buffer (20 mM, pH 8.0) overnight and purified using anion-exchange High-Q (Bio-Rad) column chromatography. The column-bound protein was eluted using a linear gradient of NaCl (0–300 mM). The active fraction obtained from this anion-exchange chromatography was dialyzed against and purified by gel-filtration Superdex 200 (GE-Healthcare, Amersham, UK) chromatography. The purity of the protein was confirmed by sodium-dodecyl sulfate polyacrylamide gel electrophoresis (SDS-

PAGE) (Figure 3.7.C). Purified *DhbIBP* was dialyzed against Tris-HCl buffer (20 mM, pH 8.0) and stored at -20°C until use.

3.3.4. Thermal hysteresis (TH) measurement for *rDhbIBP2*

The procedure to evaluate TH activity was described previously [31]. Briefly, hemolymph (0.8 μL) was placed in the middle of a HIRSCHMANN minicaps DE-M 18 glass capillary ($\text{\O} = 0.92\text{ mm}$) (HIRSCHMANN, Eberstadt, Germany). It was then soaked into a house-made capillary holder to set into a Linkam 10002L temperature-controlled photomicroscope stage (Linkam Science, London, UK). and observed under a Leica DMLB 100 photomicroscope system (Leica Microsystems AG, Wetzlar, Germany). The sample was flash frozen once to form a polycrystalline state of ice crystals by temperature reduction to -25°C , and then warming to obtain a single ice crystal in that solution. Following 3-min incubation, this ice crystal was cooled again at the rate of $-0.1^{\circ}\text{C min}^{-1}$ until bursting ice-crystal growth occurred, whose temperature was determined as the non-equilibrium freezing point [13]. The measurement was performed at least three times and averaged values were evaluated with error bars.

3.3.5. Fluorescence-based ice plane affinity (FIPA) measurement for *rDhbIBP2*

The FIPA analysis was performed according the published procedures [18]. Briefly, a single ice crystal ($\text{\O} = 3\text{ cm}$) was prepared with a cylindrical mold. After determining its *c*-axis using a polarizer, a half-cut of the cylindrical ice crystal was mounted on a hollow copper tube ($\text{\O} = 15\text{ mm}$), in which -0.8°C coolant was circulated by a refrigerant pump (Hitachi AMS-007, Hitachi, Japan). The “ice pitting method” [18] generated a six-sided star mark on the polar region of the single ice-crystal hemisphere, which indicates the a_1 – a_3 directions of the hexagonal ice unit under atmospheric pressure [12]. The hemisphere with known orientation is then mounted onto the

−0.8°C chilled probe to face down the desired ice plane. Following 1–2 h incubation with a 0.1 mg/mL solution of a fluorescence-labeled IBP sample, the FIPA pattern illuminated on the ice-crystal hemisphere was observed under UV light. The fluorescence dye used was tetramethylrhodamine (5(6)-TAMRA-X, SE) (Thermo Fisher Scientific, Waltham, USA), which attaches to a lysine residue (K¹⁰³) of the *rDhbIBP2* isoform.

3.4. Results and Discussion

3.4.1. Hemolymph of *Dorcus hopei binodulosus* (*Dhb*) exhibits antifreeze activity

The stag beetle examined in this study (Figure 3.1.A) was originally named *Dorcus curvidens binodulosus* [152] that was classified based on morphology, ecology, and karyology. Re-evaluating its detailed morphology and genome-based classification based on mitochondrial DNA (mtDNA) suggested that this beetle should be named *Dorcus hopei binodulosus* [120]. This new classification received a consensus from the scientific community and has been adopted [120,153]. Here, we extracted mtDNA from an adult sample (Figure 3.3.) and determined its 16S ribosomal RNA (16S rRNA) sequence, which comprises 981 base pairs. This sequence exhibited 99.2% identity with the 16S rRNA sequence of *Dorcus curvidens binodulosus* (GenBank accession no. AB178292.1) [152] and was therefore designated *Dorcus hopei binodulosus*.

IBP secretion was examined in 0.8 μ L hemolymph extracted from the final instar larvae of *Dhb*, which were raised according to the procedures shown in Figure 3.4. Of these, 40 were cold-acclimated at 4°C or 10°C in the last 2 months of breeding, and 11 were non-cold-acclimated at 25°C during the last 2 months. The hemolymph droplet was flash frozen on the Linkam 10002L photomicroscope stage to form an assembly of numerous single ice crystals, from which we reduced to one single ice crystal by manipulation of the stage temperature near 0°C [154]. We then applied slow temperature lowering ($-0.1^{\circ}\text{C min}^{-1}$) on this ice crystal, which modified it into a lemon-like morphology (Figure 3.1.F) and caused a vein-like bursting growth (Figure 3.1.G,H). These are typical observations for a solution containing hyperactive IBP [22]. Notably, such changes were detected for 4°C- and 10°C-acclimated larvae, while not for 25°C-incubated larvae, indicating that *Dhb* does not synthesize IBP without cold-acclimation. The temperature at which the bursting ice growth occurred was evaluated as the freezing point. The melting point of the lemon-like single ice crystal was also evaluated by increasing stage temperature, which allowed

TH evaluation [154]. The TH values of the hemolymph were variable according to a development stage and a larval size, and maximal values of $1.7^{\circ}\text{C} \pm 0.3^{\circ}\text{C}$ and $4.4^{\circ}\text{C} \pm 0.2^{\circ}\text{C}$ were determined for 4°C - and 10°C -acclimated final instar larvae, respectively. No significant TH value (0°C) was detected for the hemolymph of non-cold-acclimated larvae. Graham *et al.* (1977) reported a detection of comparable TH activity ($\sim 5^{\circ}\text{C}$) for the *TmIBP*-containing hemolymph [82]. The present observations hence suggest that *Dhb* preferably synthesizes hyperactive IBP (*DhbIBP*) by 10°C -cold acclimation. The *T. molitor* larvae maximize *TmIBP* synthesis when acclimated at 4°C [155], whereas 4°C -acclimated *Dhb* larvae exhibited poor activity. We speculate that the *Dhb* larva finds it challenging to maintain its metabolic rate at 4°C because of its large body (~ 20 g) compared with the *T. molitor* larva (< 0.2 g), which leads to decreasing *DhbIBP* production at lower temperatures.

3.4.2. *Dhb* larvae tolerate -5°C preservation for 24 hours

To examine cold survivability of final instar *Dhb* larvae acclimated at 10°C , we performed chilled preservation of *Dhb* larvae at -5°C and -10°C for 24 h. A dry plastic box (15 cm \times 10 cm \times 5 cm) containing naked larvae was placed in an incubator (model LTI-601SD, EYELA, Tokyo, JPN) preset at the required temperature (Figure 3.4.). We took out the chilled vessel after the 24 h preservation period to evaluate larval recovery after warming them to room temperature (24°C). All 10 larvae remained unfrozen by maintaining the supercooled state during the -5°C -preservation and fully recovered after warming (Video S1; available online at <https://www.mdpi.com/article/10.3390/ijms22073637/s1>). By contrast, at -10°C , all 10 larvae froze and did not recover. We next performed the -5°C -experiment with water droplets attached to larval skin. This droplet seeds ice crystals on the larval body and freezes them. The ice-seeding froze all 3 larvae during the 24-h preservation at -5°C , and the frozen larvae never recovered.

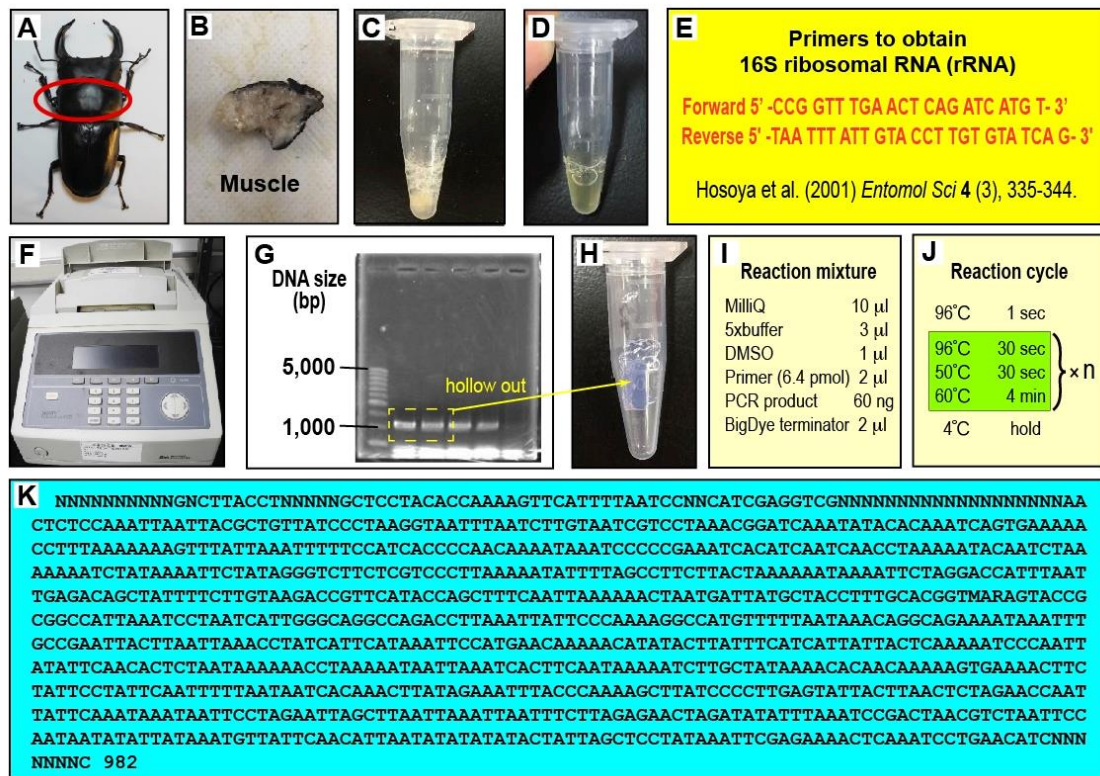


Figure 3.3. Taxonomic identification of the stag beetle *Dorcus hopei binodulosus*.

(A) The adult sample (♂) to identify the DNA sequence encoding its 16S ribosomal RNA (16S rRNA). After chilling its body on ice for anesthesia, we cut out the chest (red ellipse). (B) The chest muscle (25 mg) was collected using tweezers. (C) Muscle homogenized with 200 µL lysis buffer provided in the DNeasy blood & tissue kit (QIAGEN, Hilden, Germany). Following the kit protocol, (C) was incubated with a proteinase provided by the kit at 56°C for 2 d to obtain crude extracts. (D) DNA pool obtained from the crude extract by using detergents in the kit. (E) Two primers synthesized according to Hosoya, T. *et al* [ref. 152 in the text]. to obtain DNA encoding 16S rRNA. (F) Our PCR instrument (GeneAmp PCR system 9700, Applied Biosystems, Foster city, USA). The reaction cycle of 94°C (2 min)–{94°C (40 sec)–47.3°C (50 sec)–70°C (7 min)} × 35°C–72°C (7 min)–4°C (hold) was performed using the DNA pool and primers (E) and the reaction mixture in the kit. (G) Agarose gel electrophoretogram to examine PCR products. A major band was observed at approximately 1,000 base pairs (bp), which is the estimated size for DNA encoding 16S rRNA. (H) A portion of the gel with our target DNA excised out from (G). Approximately 300 ng DNA was obtained from the gel by using QIAquick gel extraction kit 250

(QIAGEN, Hilden, Germany). **(I)** Reaction mixture and **(J)** PCR cycle to amplify our DNA. Forward and reverse PCRs were performed separately and repetitively (n = 25–50) with modifications to the program indicated in green (ex. 30 → 20 sec, 50 → 47°C). **(K)** The 982-bp DNA sequence encoding 16S rRNA of our beetle determined with a sequence analyzer (3500 Series Genetic Analyzer, Thermo Fisher Scientific, Waltham, USA). This final sequence, except 45 “N”s (unidentified nucleotides), shares 99.2% identity with *Dorcus curvidens binodulosus* (NCBI GenBank accession NO. AB178292.1), which was later revised to *Dorcus hopei binodulosus*.

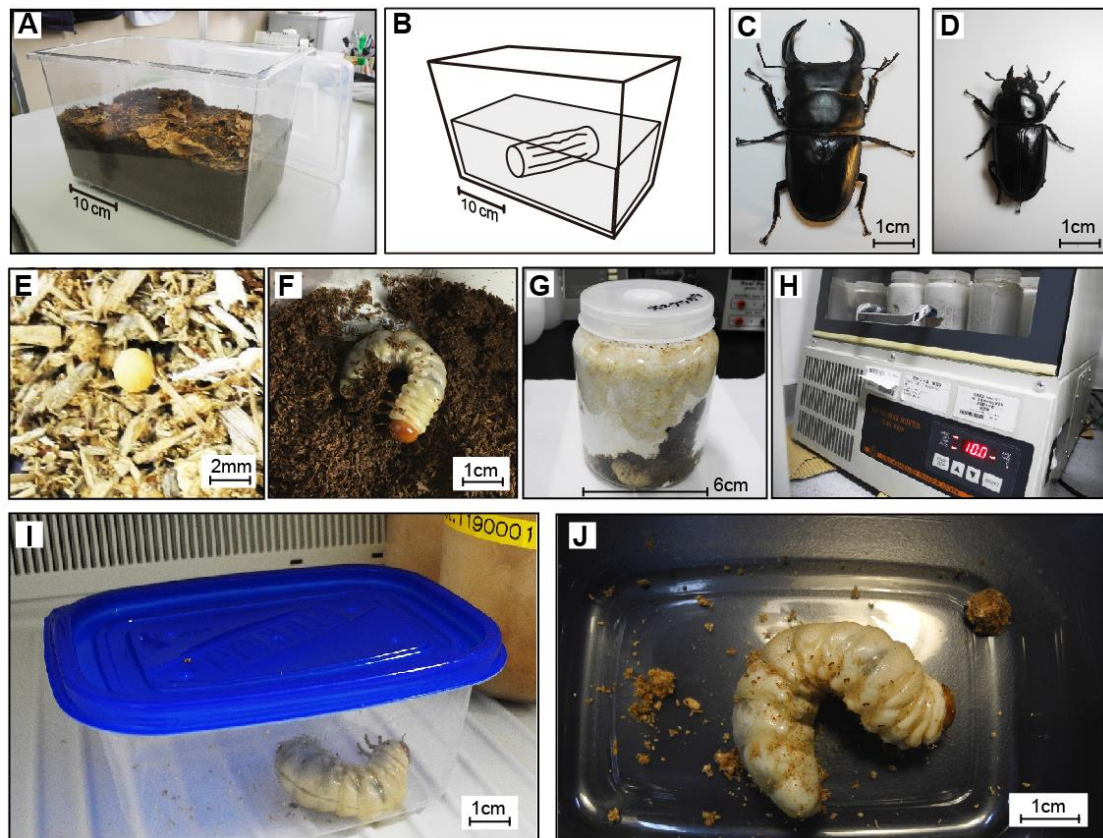


Figure 3.4. Preparation of *Dorcus hopei binodulosus* larvae.

(A) An acrylic case (37 × 22 × 25 cm) to breed the adult *Dhb* pair, where 1/2 the case was filled with commercial leaf mold (KBSP5.0, Four-Seasons, Sapporo, Japan). (B) A rotten piece of wood (*Quercus serrata*, Ø = 12 cm, *l* = 23 cm) was immersed into the mold. *Dhb* eggs were laid within this wood. (C) Male (♂) and (D) female (♀) *Dhb* bred to obtain larvae examined in this study. (E) A *Dhb* egg extracted from rotten wood. A total of 51 eggs were collected until the end of the summer of 2019. Each egg was separately moved into a cup (80 mL) filled with the same mold and incubated at 25°C. The infant larva (1st instar) hatched 1 month later. (F) The 2nd instar larva grew to ~2.5 cm in that summer. (G) A bottle (800 mL) filled with *Quercus* sawdust, in which the larva (F) was bred until it grew to 3rd (final) instar after incubation for 2 months at 25°C. Lignin-degraded nutrients in the sawdust are thought to accelerate larval growth. (H) A low-temperature incubator (model LTI-601SD, EYELA, Tokyo, JPN) to induce cold-acclimation of the 3rd instar larvae. Following the 2-month incubation at 25°C, they were cold-acclimated for an additional 2 months. Forty larvae were divided into two groups for cold-acclimation at either 4°C or 10°C.

The remaining eleven were bred at 25°C for reference. **(I)** A plastic vessel containing a 10°C-acclimated larva was placed in a freezer for 24-h chilled preservation at −5°C. **(J)** A *Dhb* larva, out of the freezer after 24 h of chilled preservation. A movie showing the recovery of this larva from the −5°C-chilled preservation is shown as **Video_S1** (<https://www.mdpi.com/article/10.3390/ijms22073637/s1>).

Note that reproducibility of these data was verified by using additional final instar larvae raised from different male-female pairs of *Dhb* captured in Osaka Japan. Asahina & Ohyama (1969) reported that larvae of some Japanese stag beetles overwinter within a small space of rotten wood, whose temperature was evaluated at -7°C , whereas outside air was chilled to approximately -15°C in the middle of winter [116]. They reported that beetle larvae remained unfrozen, whereas larvae of moths, namely *Arctiidae* and *Noctuidae*, froze in the same space. Although data on ambient temperatures of the *Dhb* larval habitat in the middle of winter are non-existent, the results suggest that *Dhb* tolerating up to -5°C can be categorized as a freeze-avoiding species, where cold-protective substances of the hemolymph, including IBP, prevents freezing for cold-survival.

3.4.3. *Dhb*IBP and *Tenebrio molitor* IBP show significant similarities

We constructed a cDNA library of *Dhb* according to the procedures described in Materials and method. We synthesized primers based on the DNA sequences encoding *Tm*IBP and *Dc*IBP [83,117]. Partial sequence determination of the DNA amplified using the forward- and reverse-primers and extension of that sequence using an improved version of the primers enabled us to identify at least 6 isoforms of IBP in the final instar larva of *Dhb* (Figure 3.5.). Alignment of the amino acid sequence with known beetle IBP isoforms is shown in Figure 3.6. The data revealed that *Dhb* synthesizes six isoforms of *Dhb*IBP, which are thought to exist as a mixture in the hemolymph, similar to *T. molitor* and *D. canadensis*. Many organisms, including fish, plants, and fungi, also synthesize multiple isoforms of IBP, a mix of which exhibits higher TH activity than any single isoform [31,156]. The first 28 residues of all *Dhb*IBP isoforms were designated as the signal peptide, similar to *Tm*IBP, suggesting that *Dhb*IBP isoforms are secreted into an extracellular space. Notably, this 28-residue signal peptide was also conserved in *Tm*IBP, but not in *Dc*IBP. The nucleotide sequence of *Dhb*IBP1 encoding the signal peptide especially shares

98.8% identity with the *Tm*IBP isoform Tq (accession no. DQ229126.1.) [157] and their amino acid sequences are 100% identical. *Dhb*IBP isoforms are composed of repetitive peptides from the 12-residue consensus sequence TCTxSxNCxxAx (x is any amino acid residue) (Figure 3.5.B), which differentiates the number of repetitions. A BLAST search (<https://blast.ncbi.nlm.nih.gov/Blast.cgi>) revealed that the top 20 polypeptides whose nucleotide sequences shared significant similarity with *Dhb*IBP isoforms were *Tm*IBP isoforms, of which *Dhb*IBP6 exhibited highest identity (90%) with the *Tm*IBP isoform Tq. DNA sequence similarity between the 6 *Dhb*IBP isoforms and 25 *Tm*IBP isoforms was $82\% \pm 5\%$ on average, whereas that between the 6 *Dhb*IBP isoforms and 10 *Dc*IBP isoforms was $67\% \pm 2\%$; *Dhb*IBP isoforms are similar to *Tm*IBP isoforms. The Blast search using DNA sequence of *Dhb*IBP3 against the *T. molitor* genome (GCA_014282415.1) further showed that 3'-untranslated region (UTR) of these two DNAs exhibited 81.9% of high sequence identity (122/149 base). The other 5' and 3'-UTR sequences of *Dhb*IBP also exhibited 80%–85% of high sequence identity with those identified in the *Tm*IBP genome. It should be noted that intron does not exist in the *Tm*IBP genome sequence [158].

The 108-residue isoform *Dhb*IBP1 is composed of eight tandem repeats of the 12-residue consensus sequence (Figure 3.5.A). Moreover, it possesses the highest isoelectric point of all six isoforms ($pI = 8.51$, Figure 3.5.C) due to the presence of five arginine residues, which may increase its activity with an activity enhancer [159]. *Dhb*IBP2 and *Dhb*IBP3 are composed of seven repeats of the consensus sequence. *Dhb*IBP2 is the largest isoform (11.2 kDa) and contains 109 residues. The C-terminus of *Dhb*IBP2 contains the 12-residue segment VLLLSKIIEHDD, which deviates from the repetition rule and does not exist in other IBPs. A highly similar sequence, namely VLLLSKIHKHDY, is also located in the C-terminus of the *Dhb*IBP4 isoform. The presence of this sequence in only two isoforms indicates that it does not play a crucial role in ice-

binding and works as a capping structure to stabilize the tertiary fold of these isoforms. In the 6th and 7th repeat of *DhbIBP3*, the conserved tripeptide sequence -Thr-Cys-Thr- (TCT) is replaced with -Thr-Cys-Ile- (TCI), which is not found in other *TmIBP* isoforms. *DhbIBP 5* and *6* are composed of six repeats of the consensus sequence. *DhbIBP5* exhibited 79% similarity to the 84-residue *TmIBP* isoform denoted 4–9 [83], which is the most abundant isoform (~50%) in *T. molitor*. The smallest isoform *DhbIBP6* (8.2 kDa) shares the highest similarity (80%) with another *TmIBP* isoform denoted 2–14. Another feature of *DhbIBP* isoforms is that the N-glycosylation site composed of the tripeptide NxT/S (x is any residue) exists within the last repeat of all *DhbIBP* isoforms (Figure 3.5.A, highlighted in green). More glycosylation sites exist in the N-terminal region of *DhbIBP1* and 6th repeat of both *DhbIBP1* and *DhbIBP3*. The glycans do not cause steric interference during ice-binding in the other IBP species [83]. No significant effect of glycan on TH activity was verified for our recombinant isoform of *DhbIBP2* that contains no glycan, as it was prepared with *Escherichia coli* expression system (Figure 3.7.).

3.4.4. A *DhbIBP* isoform equips the properties of hyperactive IBP

The production of a small protein (<10 kDa) is often difficult; however, tagging it with thioredoxin (Trx) sometimes improved yield, since the resultant fusion protein tends to become more stable and soluble [160]. Here, recombinant *DhbIBP2* (*rDhbIBP2*) was prepared as a 26 kDa fusion protein with a Trx-tag (Figure 3.7.A). The “His-tag,” consisting of six consecutive histidine residues, was inserted between Trx and *DhbIBP2*. The His-tag binds *rDhbIBP2* selectively to a Ni-NTA column, enabling its elution with imidazole buffer.

A soluble fraction containing *rDhbIBP2* was obtained using the Ni-NTA column and dialyzed against Tris-HCl buffer (20mM, pH 8.0) at 25°C overnight. Notably, the solution exhibited no sign of TH activity before dialysis, but it was detected after dialysis (Figure 3.1.C–E).

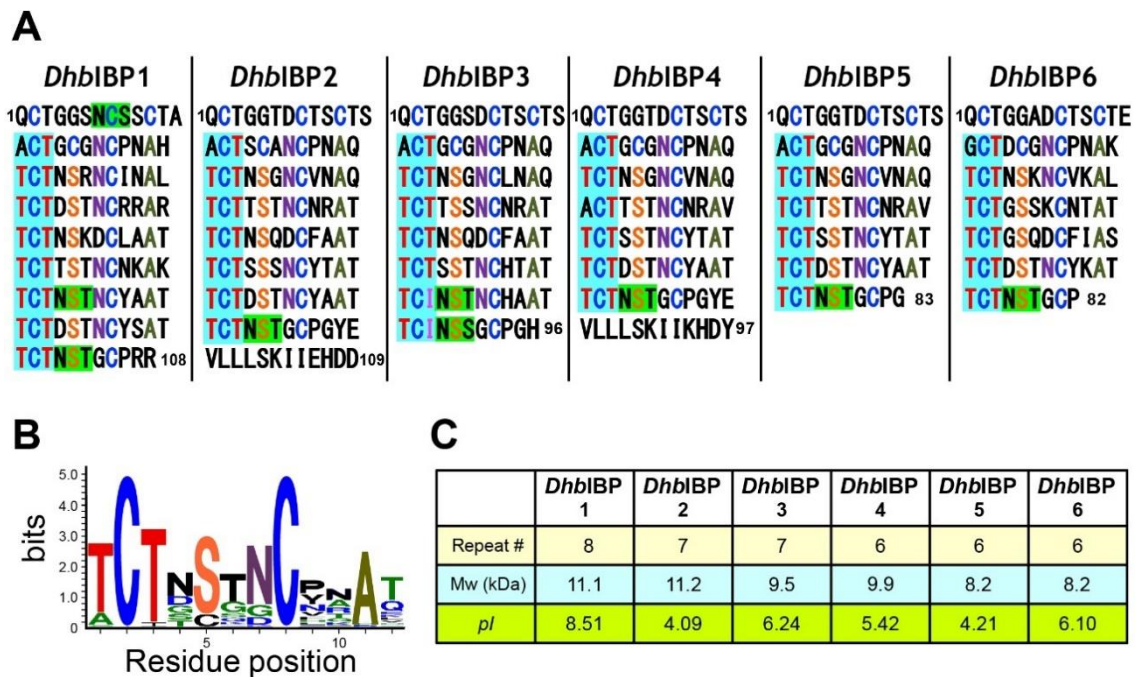


Figure 3.5. Amino acid sequence of *Dorcus hopei binodulosus* (*Dhb*)IBP.

(A) Sequence comparison between the six *DhbIBP* isoforms. Each consists of 6–8 tandem repeats of a 12-residue consensus sequence, in which “TCT” locating the 3 ranks of ice-like waters are highlighted with cyan. N-glycosylation sites (NxT/S, x is any residue) are highlighted with green. (B) The WEBLOGO plot (<http://weblogo.berkeley.edu/>) showing the consensus amino acid sequence based on the alignment of all *DhbIBP* sequences. The 12-residue consensus sequence TCTxSxNCxxAx was deduced from this plot. (C) Biochemical properties of the six *DhbIBP* isoforms. Number of tandem repeats, estimated molecular weights, and isoelectric points were evaluated for each isoform.

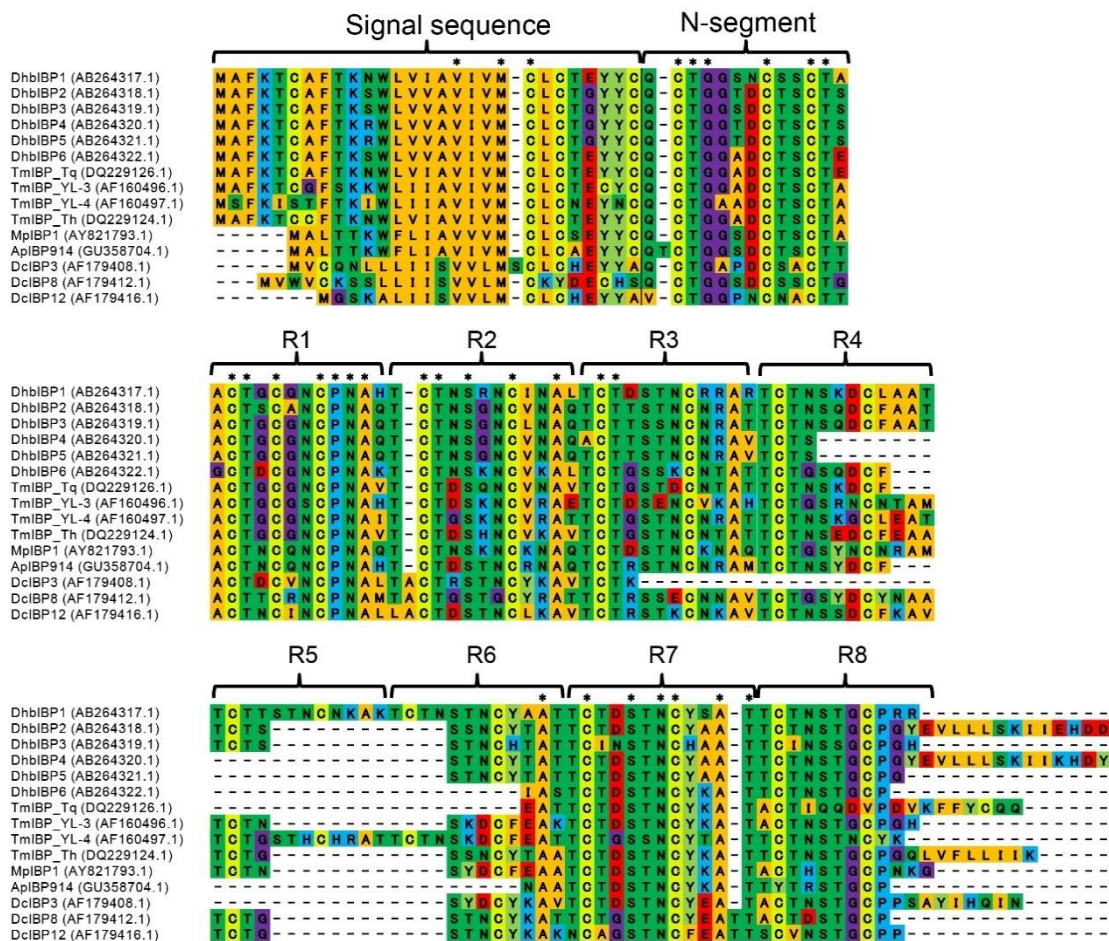


Figure 3.6. Alignment of the amino acid sequence of beetle IBPs.

Amino acid sequence alignment was performed for beetle hyperactive IBPs composed of tandem repeats of the 12-residue consensus sequence TCTxSxNCxxAx using the MUSCLE algorithm in the MEGA7 software (<https://www.megasoftware.net/>). This figure compares the amino acid sequence of *Dorcus hopei binodulosus* (*Dhb*) IBP isoforms with those of known beetle IBP isoforms exhibiting similar repetitive sequences extracted from the NCBI database (<https://www.ncbi.nlm.nih.gov/>). The accession code (ex. AB264317.1) of the mRNA sequence in the NCBI GenBank (<https://www.ncbi.nlm.nih.gov/genbank/>) is indicated for each *Dhb*IBP isoform (ex. *Dhb*IBP1). The N-terminal segment (N-segment) of all *Dhb*IBP isoforms starts with QCT· located next to the signal peptide sequence (signal sequence) and then tandem repeats of the 12-residue consensus sequence (R1–R8). The residues marked with an asterisk (*) are perfectly conserved in all IBP isoforms. Color indications for amino acids are as follows; neutral: green, positively charged: cyan, negatively charged: red, hydrophobic: orange, Cys: yellow, Gly: purple, and Tyr: light-green.

This indicates that during dialysis, the 18 cysteines of *Dhb*IBP2 were oxidized to generate disulfide bonds, leading to a properly folded protein. Such refolding was also observed when the recombinant *Tm*IBP isoform was dialyzed [161], which depends on both the dialysis period and incubation temperature. Following dialysis, the active solution was applied to a High-Q anion-exchange column, which eluted three peaks shown in Figure 3.7.B using a NaCl gradient (0–300 mM). The second peak exhibited TH activity and was applied to the Superdex 200 gel-filtration column. This gave us a fraction containing purified *rDhb*IBP2, which was verified as a single band on 15% tricine SDS-PAGE (Figure 3.7.C). Notably, a position mismatch on SDS-PAGE was reported for recombinant *Tm*IBP [161]. Purified *rDhb*IBP2 exhibited hyperbolic TH-dependence on protein concentration, which has been reported for all IBP species [150]. A TH value of approximately 3°C was evaluated at 150 μM (Figure 3.7.D), which is consistent with that obtained for a hyperactive isoform of *Tm*IBP (3°C at 200 μM) [161]. A single ice crystal modified into lemon-like morphology within this hysteresis gap and exhibited a vein-like bursting growth pattern, similar to those observed for the *Dhb* hemolymph (Figure 3.1.F–H). Again, they are typical observations for hyperactive IBPs. Furthermore, the target ice plane of *rDhb*IBP2 was examined by observing its binding onto a single ice-crystal hemisphere of a golf-ball size ($\varnothing = 30$ mm), which was prepared by using a plastic pipe and refrigerant circulator [18]. This ice-crystal hemisphere was immersed in *rDhb*IBP2 (0.1 mM) labeled with the fluorescent detergent tetramethylrhodamine and held at -0.8°C for 2 h. Then, the ice hemisphere was pulled and photographed under ultraviolet (UV) light. The illumination was observed entirely on the single ice-crystal hemisphere (Figure 3.7.E), indicating that *rDhb*IBP2 can bind to multiple ice planes, including prism, pyramidal, and basal planes, similar to known hyperactive IBPs [18]. The *rDhb*IBP2 was hence identified as a hyperactive IBP regardless of the Trx-tagging and removal of the glycosylation ability.

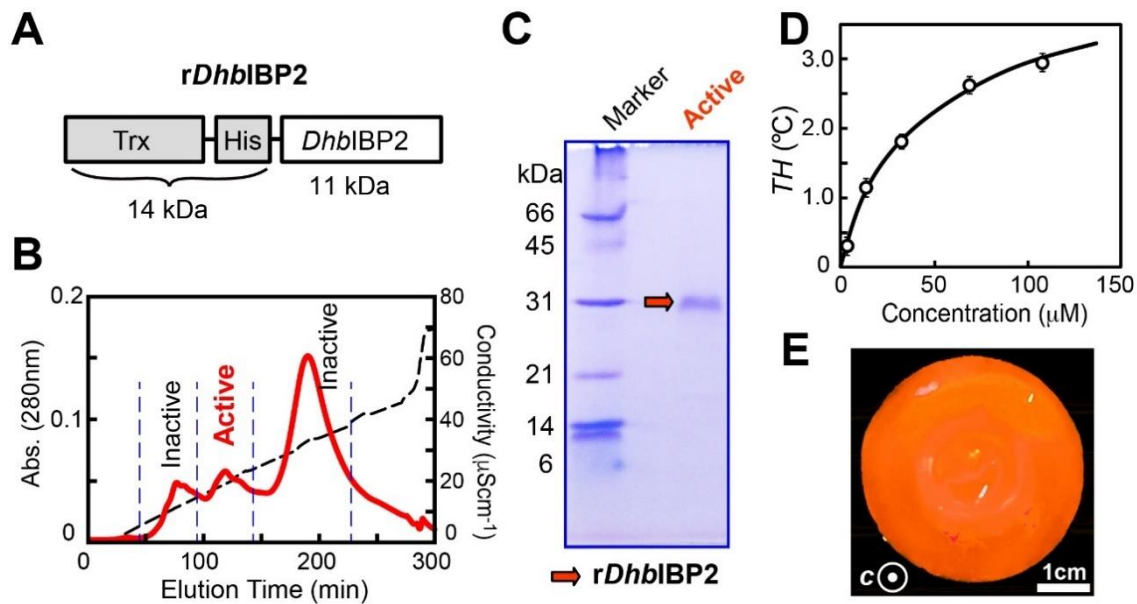


Figure 3.7. Preparation of a recombinant *Dorcus hopei binodulosus* (*Dhb*)IBP2 isoform as a fusion protein.

(A) A schematic representation of rDhbIBP2 composed of thioredoxin (Trx), histidine tag (His), and the 109-residue DhbIBP2 isoform connected in tandem. (B) The UV absorbance (280 nm) profile of rDhbIBP2 obtained with High-Q anion-exchange chromatography using an NaCl gradient (0–70 $\mu\text{S cm}^{-1}$). The lemon-like ice crystal and thermal hysteresis (TH) were detected for the “active” peak. (C) SDS-PAGE of the rDhbIBP2 sample purified with Ni-column chromatography. (D) Concentration dependence of TH values of rDhbIBP2. The measurement was performed in triplicate to draw error bars representing standard deviation. (E) A photograph of a single ice-crystal hemisphere, on which fluorescent (orange) rDhbIBP2 adsorbs entirely to illuminate the whole surface under UV light.

Davies *et al.* determined a 1.4-Å resolution crystal structure of *TmIBP* isoform 2–14 (PDB code: 1EZG) that appeared to form an extremely regular right-handed β -helix (Figure 3.8.A) [84]. Each coil consists of the 12-residue consensus sequence T^{1st}CTxSxNCxxAx^{12th}, of which side-chain OH-groups of T^{1st} and T^{3rd} are aligned with another string of waters trapped in a trough, leading to the construction of three ranks of oxygen atoms along the β -helical axis [81]. This enabled us to construct the model structure of *DhbIBP6* (Figure 3.8.B,C) because it shares 80% sequence similarity with *TmIBP* isoform 2–14 [83] (Figure 3.6.). By using the structural coordinates of *TmIBP* (PDB code: 1EZG) as a template, the model structure of this *DhbIBP6* isoform was constructed using the software MODELLER (<http://salilab.org/modeller/>). PyMOL and CHIMERA (<http://www.cgl.ucsf.edu/chimera/>) were also used for visualizing and drawing the model. As shown in Figure 3.8.B and 3.8.C, a rounded rectangular-shaped molecule composed of 6-turns right-handed β -helices was readily modeled for *DhbIBP6*, on which the location of the 3 ranks of oxygen atoms were speculated to be similar to *TmIBP*, though their atom positions were not finely postulated. Formation of the 8 disulfide bonds (C⁸–C¹⁸, C¹⁵–C²¹, C²⁷–C³³, C³⁹–C⁴⁵, C⁵¹–C⁵⁷, C⁶³–C⁶⁹, and C⁷⁵–C⁸¹), which are thought to stabilize β -helical formation were also assumed for *DhbIBP6* (Figure 3.8.B,C), on which sidechains of the consensus sequence are thought to be oriented toward “out^{1st}-in-out-out-in-out-out-in-out-out-in-out^{12th}” directions (Figure 3.8.C). Among them, inner pointing residues C^{2nd}, S^{5th}, C^{8th}, and A^{11th} comprised a core region together with six disulfide bonds between C^{2nd} and C^{8th}. The two-dimensional array of oxygen atoms on *TmIBP* (Figure 3.8.A) exhibited a perfect position match to the water’s oxygen atoms, constructing multiple ice-crystal planes [84], which can also be speculated for *DhbIBP6*. These structural features were adopted for the larger *DhbIBP* isoforms (Figure 3.5.), as the *TmIBP* structure is artificially elongated by the addition of more coils. Marshall *et al.* (2004) observed TH activity for a series of artificially prepared β -helical IBPs consisting of 6–11 tandem repeats

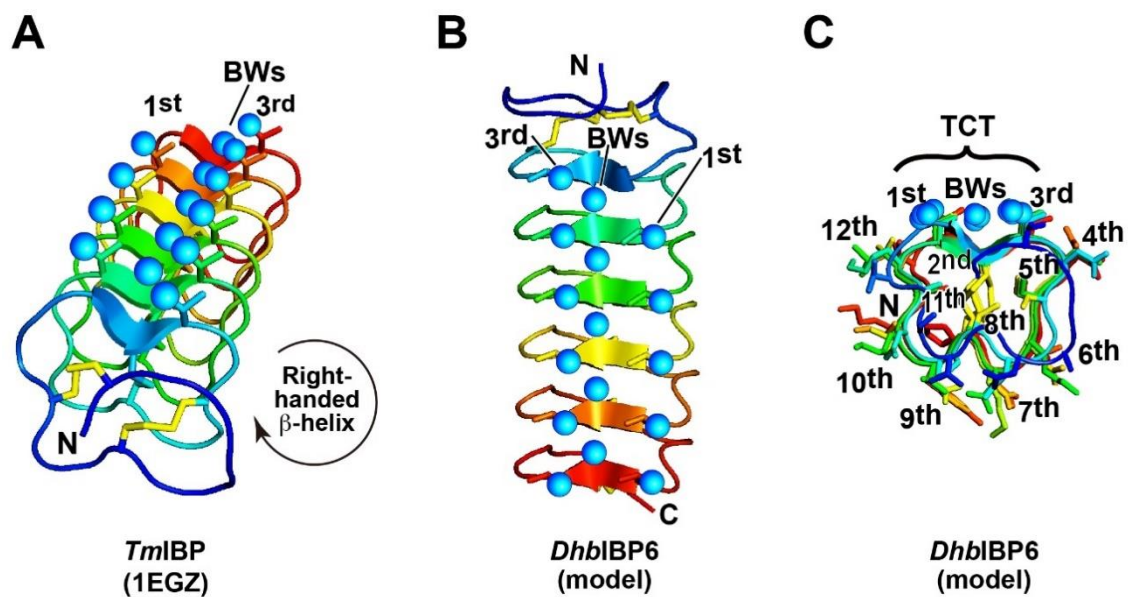


Figure 3.8. A model structure of *Dorcus hopei binodulosus* (*Dhb*)IBP6.

(A) The X-ray crystal structure of an insect IBP from the beetle *Tenebrio molitor* (*TmIBP*, PDB code = 1EZG) determined by Graham *et al.* [82]. Tandem repeats of TCT-containing sequence locate 3 ranks of oxygen atoms on side-chains T^{1st} and T^{3rd} as well as surface-bound waters (BWs) trapped in a trough. (B) A structural model of the *DhbIBP6* isoform constructed using the *TmIBP* structure as a template. *DhbIBP6* and *TmIBP* share 80% sequence identity. (C) A structural view down the model of *DhbIBP6* from N- to C-terminus. The inner core is assumed to form six disulfide bonds between C^{2nd} and C^{8th} and organize the 3 ranks of oxygen atoms on the TCT sequence.

and reported a 10–100-fold gain in activity upon going from 6 to 9 repeats [162]. The activity however decreased for 10 and 11 repeats, ascribed to imperfections of the position match between the ice-binding site and ice lattice, which occurs upon addition of too many coils.

3.4.5. Unrevealed gene transfer mechanism may exist between *Dhb* and *Tm*

The hyperactive IBPs with the TCTxSxNCxxAx sequence have been identified for four beetle species: *T. molitor*, *D. canadensis*, *A. polita*, and *M. punctipennis* [82,117–119]. The present examined *Dhb* should be a new member. In addition, our preliminary results suggest that another stag beetle *Dorcus rectus rectus* (*Drr*) synthesizes at least 14 isoforms of hyperactive IBP (Figure 3.9.), which also exhibit the same repetitive property to *Dhb*IBP. Notably, *Dhb* and *Drr* belong to the *Scarabaeoidea* superfamily, whereas the above four beetles with the 12-residue consensus sequence belong to *Tenebrionoidea* (Figure 3.10.). To investigate hypothetical evolutionary relationship among these beetles, we prepared a maximum likelihood phylogenetic tree (Figure 3.10.A) based on a total of 29 mRNA sequences of their IBP isoforms registered in the National Center for Biotechnology Information (NCBI) GenBank. In Figure 3.10.A, *Scarabaeoidea Dhb* (6 red dots) is the closest to *Tenebrionidae T. molitor* (11 cyan squares), which is consistent with the present identified similarities between *Dhb*IBP and *Tm*IBP. However, such hypothetical relationship is not supported by the most updated version of the fossil-calibration-based beetle phylogenetic tree (Figure 3.10.B) [163]. The Figure 3.10.B shows that superfamilies *Scarabaeoidea* and *Tenebrionoidea* belong to distant lineages, which branched off 250–300 million years ago which corresponds to the Permian glaciation period in the geological time scale [164]. One may speculate that IBPs predate speciation 300 million years ago and that most of the diverged beetles contain IBP genes. However, no *Dhb*IBP-like sequence exists in the genome of another *Scarabaeoidea* beetle, *Trypoxylus dichotomus*, for example (NCBI Genbank code:

*Drr*IBP1 (LC598940) Q¹CTGSPDCTSC**TTACTDCGNCPNAQ**TCTNSQNCVSAQ**TCTNSGNCVNAQ**TCTASTNCNRAT
TCTSSKDCFAAA**TCTTSTNCYTAATCTDSTNCYAATACTN**SSGCPNPSIKFF¹¹³

*Drr*IBP2 (LC598941) Q¹CTGSPDCTSC**TTACTDCGNCPNAQ**TCTNSQNCVSAQ**TCTNSGNCVNAQ**TCTASTNCNRAT
TCTSSKDCFAAA**TCTTSTNCYTATTCTDSTNCYAATACTN**SSGCPNPSIKFF¹¹³

*Drr*IBP3 (LC598942) Q¹CTGSPDCTSC**TTACTDCGNCPNAQ**TCTNSQNCVSAQ**TCTNSGDCVNAQ**TCTASTNCNRAT
TCTSSKDCFAAA**TCTTSTNCYTAATCTDSTNCYAATACTN**SSGCPNPSIKFF¹¹³

*Drr*IBP4 (LC598943) Q¹CTGGSDCSRCTA**ACTGCGNCPNAHTCTNSRNCINAL**TCTDSTNCR**RARTCTSSKDC**LAAT
TCTTSTNCNRA**KTCTNSTNCYAARTCTNSTNCYSATTCT**NSTGCPRR¹⁰⁸

*Drr*IBP5 (LC598944) Q¹CTGGADCT**SCTSTCTGCANCPNAQ**TCTNSGNCVNAQ-----**ACTASRNCNKAT**
TCTNSQDCFAA**TSTTSTNCYTATTCINSTNCHAATTC**INSSGCPGS⁹⁶

*Drr*IBP6 (LC598945) Q¹CTGGADCT**SCTSTCTGCANCPNAQ**TCTNSGNCVNAQ-----**ACTASRNCNKAT**
TCANSQDCFAA**TSTTSTNCYTATTCINSTNCHAATTC**INSSGCPGS⁹⁶

*Drr*IBP7 (LC598946) Q¹CTGGADCT**SCTSTCTGCANCPNAQ**TCTNSGNCVNAQ-----**ACTASRNCNKAT**
TCTKSQDCFAA**TSTTSTNCYTATTCINSTNCHAATTC**INSSGCPGS⁹⁶

*Drr*IBP8 (LC598947) Q¹CTGGPDCT**SCTA**ACTGCGNCPNAQ**TCTNSENCINAQ**-----**TCTSSTNCNRAT**
TCTSSKDCFAAA**TCTSSTNCYTATTCTDSTNCYAATTCT**NSTGCPNPSIKFV¹⁰¹

*Drr*IBP9 (LC598948) Q¹CTGGTDCT**SCTVACTGCGNCPNAV**TCTNSGNCVNAV-----**TCTASTNCNRAT**
TCTTSKDCFEAV**TCTGSTNCYKATTCTDSTNCYGATTACT**NSTGCPGT⁹⁶

*Drr*IBP10 (LC598949) Q¹CTGGTDCT**SCTA**ACTGCGNCPNAQ**TCTNSGNCINAV**-----**TCTTSTNCNRAT**
TCTSSTNCYIAA-----**TCTDSTNCYAATACTNSTGCPGYQV**LF⁸⁹

*Drr*IBP11 (LC598950) Q¹CTGGTDCT**SCTA**ACTGCGNCPNAV**TCTNSGNCINAV**-----**TCTTSTNCNRAT**
TCTSSTNCYIAA-----**TCTDSTNCYAATACTNSTGCPGYQV**LF⁸⁹

*Drr*IBP12 (LC598951) Q¹CTGGSDCT**SCTVACTGCGNCPNAV**TCTNSGNCINAV-----**TCTSSTNCNKAT**
TCTSSKDCFAA**T-----TCTDSTNCYAATTCTN**SSGCPGS⁸⁴

*Drr*IBP13 (LC598952) Q¹CTGGSNCS**SCTA**ACTGCGNCPNTH**TCTNSRNCVSAR**-----**TCTGSTNCKKAR**
TCTGSTNCYAA**RCTNSTNCYSAT-----TCTNSTGCPRH**⁸⁴

*Drr*IBP14 (LC598953) Q¹CTGGSNCS**SCTA**ACTSCGYCPNAHTCTNSRNCGNAR**-----**TCTSSTNCKKAR**
TCTSSTNCYAA**KTCTSSTNCYSAT-----TC**INSTGCPRH⁸⁴**

Figure 3.9. Preliminary determination of primary sequences of hyperactive IBP isoforms of the stag beetle *Dorcus rectus rectus* (*Drr*).

All 14 isoforms of hyperactive IBP of *Drr* (*Drr*IBP) 1–14 contain 6–8 tandem repeats of the 12-residue consensus sequence TCTxSxNCxxAx, similar to *Dorcus hopei binodulosus*. The accession code (ex. LC598940) of the mRNA sequence in DDBJ (DNA Data bank of Japan) (<https://www.ddbj.nig.ac.jp/ddbj/index-e.html>) is indicated for each *Drr*IBP isoform (ex. *Drr*IBP1). Determination of amino acid sequence was performed according to the procedures described in Methods (pages 8–10), where the forward primer (e) was modified to 5'-GGAACATATGGCGTTCAAAACGTGTGCT-3' to determine the *Drr*IBP sequence. The lemon-shaped ice crystal and its vein-like bursting crystal growth pattern (Figure 3.1.) was also observed for the hemolymph of this beetle, indicating that IBP isoforms listed in this figure exhibit a strong antifreeze activity similar to *Dorcus hopei binodulosus* (*Dhb*) IBP isoforms.

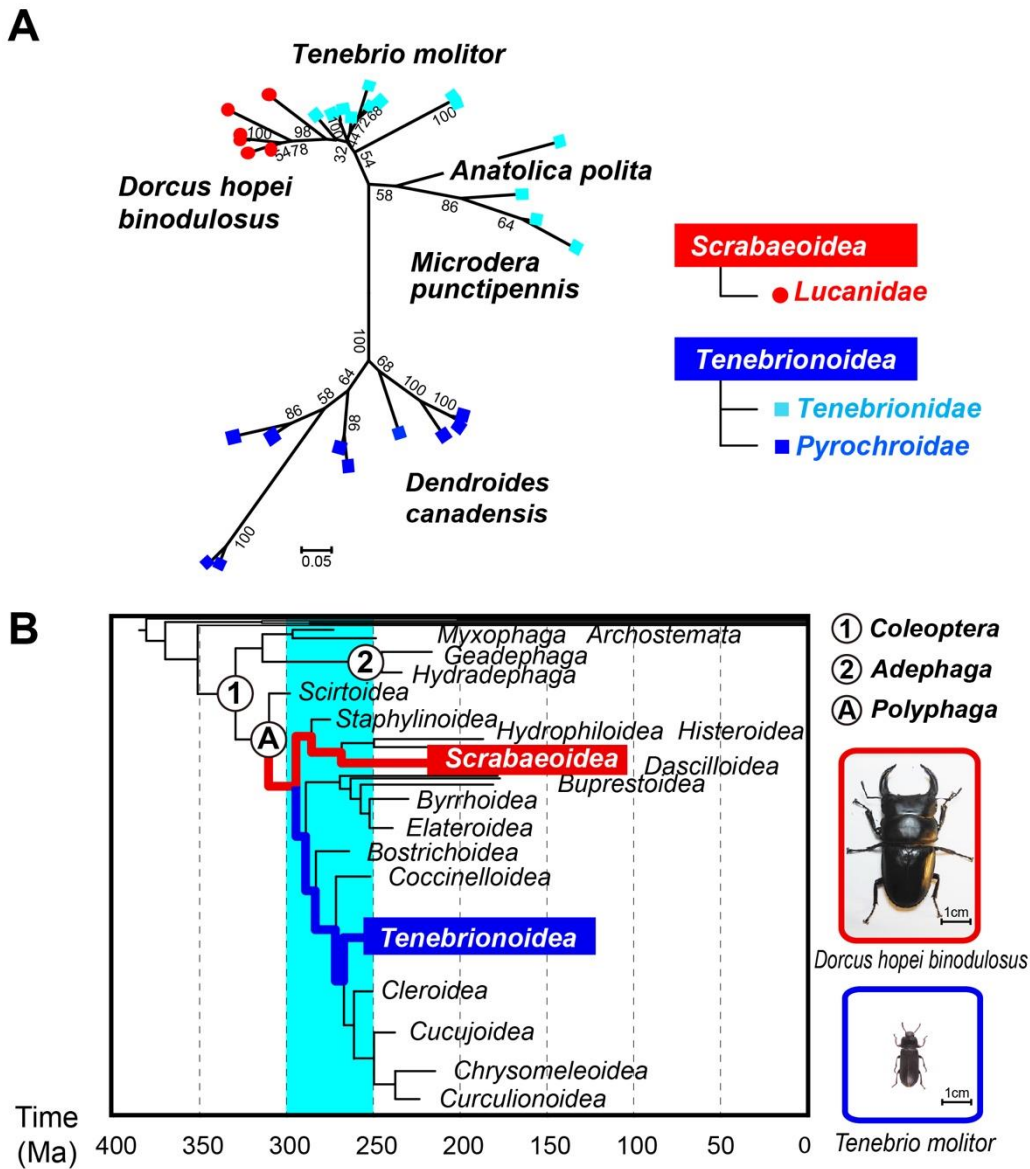


Figure 3.10. Phylogenetic relationship between the beetles synthesizing the hyperactive IBP composed of the consensus sequence TCTxSxNCxxAx.

(A) Maximum likelihood phylogenetic tree showing a hypothetical relationship among the beetles based on analysis of a mRNA sequence alignment. The tree was created with MEGA7 software (<http://www.megasoftware.net/>) based on the HKY + G model. It used 29 mRNA sequences of beetle hyperactive IBP isoforms whose NCBI accession codes are AB264317.1 – AB264322.1 (*D. h. binodulosus*), AF1591144.1 – AF160497.1 (*T. molitor*), GU358703.1 – GU358704.1 (*A. polita*), AY821792.1 – AY821793.1 (*M. punctipennis*), and AF179408.1 – AF179416.1 (*D. canadensis*). The bootstrap values for 500 replications (< 30 are not shown) was shown at the

nodes. **(B)** The fossil-calibration-based phylogenetic relationship between beetle superfamilies presented in Emmanuel, F. A. *et al.* (2017) [163]. The *T. molitor*, *D. canadensis*, *A. polita*, and *M. punctipennis* [82,117–119] belong to *Tenebrionoidea*. The ones examined in this study, namely *D. h. binodulosus* (*Dhb*) and *D. r. rectus* (*Drr*), belong to the phylogenetically distant superfamily *Scrabaeoidea*. Note that another beetle consisting of extensions of the TxT sequence, *Rhagium inquisitor*, belong to *Chrysomeleoidea*.

BNES01000010.1). Again, this type of hyperactive IBP was only identified for 4 beetle species in the past decades [82,117–119]. DNA analysis further questions the evolutionary origin of *Dhb*IBP and *Tm*IBP. Namely, the DNA sequence of *Dhb* including untranslated region, signal peptide region, and a *Dhb*IBP-encoding region exhibited a significant similarity to those identified for *Tm*IBP (Figure 3.6.).

Such similarity of the DNA sequences does not support the ordinary vertical evolution, since the sequences should not be retained in each superfamily for an ultimately long divergence period of approximately 300 million years. Indeed, no sign of sequence identity was detected for non-coding region of DNA in two different *Collembola* species, which were speculated to have diverged in the Permian glaciation period [165].

It has been shown that different lineages of organisms sometime synthesize similar genes through “convergent evolution”, which occurs when similar traits are acquired under selective pressure [166]. An example is the antifreeze glycoprotein (AFGP) discovered in two unrelated polar fishes, Antarctic notothenioid and Arctic cod. In Antarctic notothenioid fish, AFGP appears to be derived from a small fragment of a pancreatic trypsinogen gene, whereas in the Arctic cod, the DNA sequence is different [167,168]. Thus, the DNA sequences in two different organisms were also not retained in convergent evolution.

A remaining possibility to explain the DNA and protein similarities between the two phylogenetically distant beetles will be an unrevealed kind of horizontal gene transfer, the movement of genetic material between unicellular and/or multicellular organisms [169]. Recent studies based on genome sequencing revealed the presence of foreign DNA sequences in the genetic material of several species of *Lepidoptera* [170]. Indeed, pro- and eukaryotic genes that moved through the horizontal gene transfer are expressed in such insect genomes [171]. Hence, it might be speculated that progenitors of *Dhb* and *T. molitor* have acquired foreign DNA encoding

hyperactive IBP through unrevealed gene transfer mechanism mediated by an organism, despite Blast searches does not show any sign of hyperactive IBP synthesis in plants, fungi, nor bacteria DNA. One way to advance this study would be to discover more IBP-containing beetles and to clarify DNA sequence encoding their IBPs. Examples of the stag beetles that are popular and their breeding techniques are established include *Dorcus titanus*, *Dorcus rebrofemoratus*, *Lucanus maculifemoratus*, and *Prosopocoilus inclinatus*.

The present study revealed that the popular stag beetle *Dorcus hopei binodulosus* (*Dhb*) synthesizes hyperactive IBP. Cold-acclimated *Dhb* larvae were not frozen after -5°C -chilled preservation for 24 hours and recovered after warming, thus the survival strategy of *Dhb* is freeze-avoidance. The larvae synthesize at least 6 hyperactive IBP isoforms (*Dhb*IBPs), which are tandem repeat peptides of a 12-residue consensus sequence. The *Dhb*IBPs exhibited significant similarities to a known hyperactive IBP from *T. molitor* (*Tm*IBP), where progenitors of *Dhb* and *Tm* have diverged approximately 300 million years ago. Hence, any known evolution mechanism hardly explains the retainment the DNA sequence, suggesting the existence of a recent gene transfer between these two beetles to share the hyperactive IBP.

Chapter 4: General discussion

4.1. Summary in this study

IBPs have been found from cold-adapted organism including fish, insects, plants and microorganism [4]. IBPs are thought to have been evolved in structure to bind to ice crystal and to protect its hosts from freezing damage. The ice-binding properties are largely different between each IBP. The structure-function relationship of IBP is one of the topics attracting the scientist's interest in this research field. In this study, the author has been examined ice-binding mechanisms of moderate active microbial IBP and hyperactive insect IBP.

The author's laboratory found that *A. psychrotrophicus* secretes IBP and has examined its antifreeze activities, DNA sequences, amino acid sequences and evolutionary history [114,115]. Previous study showed that *Anp*IBP shaped ice crystal into a lemon-like morphology as found in hyperactive IBP [115]. The present study first shows that the ice-binding property is observed for moderately active IBP, for which its molecular mechanism was not clarified. To elucidate such a unique ice-binding mechanism, the author determined the target ice planes and X-ray crystal structures of *Anp*IBP in Chapter 2. The present study also showed that *Anp*IBP has both polygonal water networks and unique linearly aligned hollows on its IBS. It was speculated that *Anp*IBP is fine-tuned to merge with the ice–water interface of an ice crystal through the polygonally arranged water molecules and then bind to specific water molecules constructing the prism ring through the hydration water molecules trapped in the linearly aligned four hollows.

Hyperactive insect IBPs with a 12-residue consensus sequence (TCTxSxNCxxAx) have been found from four beetles belonging to same superfamily *Tenebrionoidea* [82,117–119]. The evolutionally origin of this protein is little understood. Also, IBP research has not been examined on Japanese overwintering insects. The author discovered new insect producing IBP habitat in Japan, Japanese stag beetle *Dourcus hopei binodulosus*. The *Dhb* belongs to superfamily *Scarabaeoidea* that is different from former species (*Tenebrionoidea*). The present

study identified that *Dhb* cold tolerance, gene structures, amino acid sequence, ice-binding properties, and evolutionary insight of *Dhb*IBP in Chapter 3. The author assume that *Dhb*IBP possesses highly organized waters on its IBS, whose 3 columns of linearly aligned waters and two-dimensional array of the oxygen atoms perfect match the position of the water's oxygen atoms constructing multiple ice planes. *Dhb* were thought to acquire the gene coding hyperactive IBP by horizontal gene transfer (HGT). The summary in this study is shown in Figure 4.1.

4.2. Ice-binding mechanism of moderately active *Anp*IBP vs hyperactive *Dhb*IBP

Some researchers reported that existence of ice-like waters with polygonal arrangement accompanying on its hydrophobic IBS of IBP [66, 106–109]. This caged ice-like waters are assumed to play a role in anchoring IBP to ice-water interface, thus this mechanism is called as the anchored clathrate water (ACW) mechanism [106]. The author assumes that the *Anp*IBP' polygonal water networks observed on its IBS also play such role.

Microbial IBPs usually construct many hollows on their IBS. These hollows play a crucial role in forming pentagonally organized waters [136,137,173,174]. The hollows are formed by hydrophobic residues that exist in ridge regions sandwiched by many convex. The side chains of hydrophobic residues occupy the hollows and several amide groups or carboxyl groups also exist near the hollow. Such amido groups and carboxyl groups bind to a part of polygonal waters by hydrogen bond, which stabilized polygonal water on IBS of IBP. When one residue was mutated on IBS of *Anp*IBP, polygonal water networks were not identified in defective mutant (S153Y). Based on the results, it was speculated that the polygonal waters are constructed with a perfect balance. The polygonal water networks are usually observed in microbial IBP. The positions of polygonal waters match the positions of the two-dimensional array of water's oxygen atoms constructing each ice plane [106,174]. The polygonal waters on fish IBP III are also two-

dimensionally organized, which complementary match the two-dimensional oxygen spacings of the primary prism plane or pyramidal planes [109]. *Anp*IBP accompanies polygonal water networks on its IBS while they do not arrange the waters with two-dimensional array that match the target ice plane, unlikely to other IBPs. Instead, *Anp*IBP possesses four linearly aligned hollows to recognize the oxygen atoms spacing of waters of prism planes. On IBS of *Anp*IBP, the intervals of linearly aligned bound waters on the four hollows (4.6 and 14.7 Å) perfectly match the water distance in the prism planes. The oxygen atoms of water located in the same interval (4.6 and 14.7 Å) exist in both the 1st and 2nd prism planes. In other words, *Anp*IBP accompanies the ice-like waters organized in line to match both 1st and 2nd prism planes. It is therefore assumed that only four hydration waters of *Anp*IBP control its ice-binding specificity.

In the IBS of insect IBP, 1st Thr-2nd Cys-3rd Thr were aligned on same β -sheet by tandem repeat [84]. This results in 3 columns of linearly aligned waters existed on its IBS, where 2nd column (Cys) generates linearly hollows and traps hydration waters arranged in an ice-like geometry. For both *Anp*IBP and insect IBP, the bound waters trapped in hollows is seemed to be deciding factor of its ice-binding specificity. IBP possess the unique structure to hold ice-like waters on its IBS as matching oxygen atom arrangements of ice lattice.

Microbial IBPs organize polygonal waters while for insect IBPs they have not been confirmed in their structure. One possible reason is that insect IBP does not construct a molecular surface so as to accompany the polygonal waters. Another possibility is an influence of crystal packing, where hydrophobic IBS tends to face to face and hide original structure of bound waters [110]. Given that polygonal water helps bind IBP to ice crystal surfaces, insect IBPs may also have polygonal waters on its IBS. In the future, there is a possibility to find insect IBP accompanying polygonal water. To understand how insect IBPs approach ice-water interface, further studies are needed.

4.3. Difference of antifreeze activities of *Anp*IBP and *Dhb*IBP

*Anp*IBP generated lemon like shaped ice crystals in supercooled water although it exhibits moderate TH activity [115]. The present data demonstrates that *Anp*IBP binds to contiguous multiple prism planes (i.e., 1st and 2nd prism planes) and to the mid-latitude area around the prism planes (i.e., pyramidal planes), which should result in the formation of a lemon-shaped ice crystal. *Anp*IBP can bind to multiple ice planes although its manner will not be perfectly the same as the hyperactive IBPs. Most of the microorganisms secrete IBP around them to inhibit the ice growth in their living space [29,48,52–55]. The growth speed of the prism planes toward the *a*-axis is approximately 100 times faster than that of the basal plane [20]. Thus, *Anp*IBP effectively inhibits this fast growth through its binding to the prism planes. The author assumes that *A. psychrotrophicus* protect themselves from ice injuries and become dominant in living environment by using such ice-binding properties.

Insect IBP is known to possess very high TH activity among IBPs [22]. In the present study, *Dhb*IBP is assumed to locate existence of highly organized ice-like water molecules that are capable of binding to multiple ice planes, leading to high TH activity (~5°C). The host (*Dhb*) is reported to live in -5°C-tree root stock [116]. TH value of *Dhb*IBP corresponds to the temperature of the host (*Dhb*) living environment. The author assumed that *Dhb* produces *Dhb*IBP and stabilizes supercooling state of the hemolymph, leading to tolerate such subzero temperature environment. Both IBPs examined in this study are closely related in survival strategies of their host organism.

4.4. Evolutionary mechanism of *Anp*IBP and *Dhb*IBP

Horizontal gene transfer (HGT) is exchanging of a gene between two different organisms [175], which has been reported in many microorganism producing IBPs [102,115,176–179]. The

ice cause physical damage against microorganism lived in icy environment, which leads to cell rupture. In such environment, extracellular DNA and salts are more concentrated than that in under ice ocean, which results in increasing the probability of HGT. Ice poses a strong selection pressure on microorganisms [102]. It is thought that microorganisms acquire adaptability to the new environment by obtaining foreign genes through HGT [180]. Previous study showed that the two different IBP genes possessing low sequence similarity were identified in *A. psychrotrophicus*, which suggests the importance of the gene acquisition [115]. In this study, we examined ice-binding properties of *AnpIBP1a*. The further studies of ice-binding properties of *AnpIBP2* are also interesting and it will give more understanding about survival strategy of *A. psychrotrophicus*.

In the case of insect IBP, there is possibility of HGT. The most updated version of the fossil-calibration-based beetle phylogenetic tree showed that superfamilies *Scarabaeoidea* (Dhb) and *Tenebrionoidea* (Tm) belong to distant lineages, which branched off 250–300 million years ago and corresponds to the Permian glaciation period in the geological time scale [164]. In such period, it is predicted to exert strong selection pressure like microorganism. One may speculate that HGT occurs frequently in not only microorganism but also insect and the others living in freezing environment, which suggests the importance of IBP gene for organisms to tolerate such circumstance.

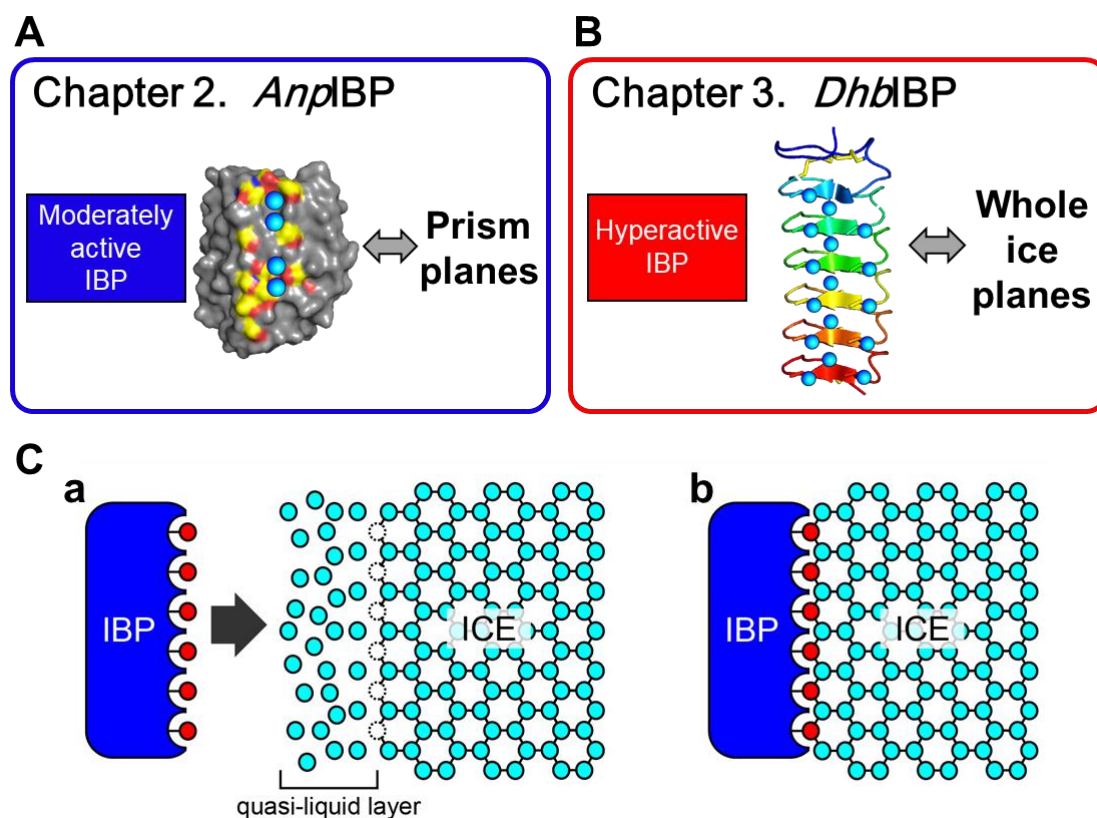


Figure 4.1. Structure-function relationship of two IBPs examined in this study.

(A) The moderately active *Anp*IBP binds to specific water molecules constructing the prism planes through linearly aligned water molecules trapped in four hollows (Chapter 2). (B) The hyperactive *Dhb*IBP possess three columns of linearly aligned oxygen atoms capable of binding to whole ice planes (Chapter 3). The hyperactive IBP was suggested to have highly organized ice-like waters on its IBS. (C) Illustration shows schematic diagram of ice-binding mechanism of IBP. IBP possess the unique structure to hold ice-like waters (red spheres) on its IBS as matching arrangement of waters (oxygen atoms) of ice lattice. The ice-like surface-bound waters of IBP are assumed to merge with water molecules constructing ice-water interface (quasi-liquid layer) of an ice crystal, leading to a connection of the IBP to an ice crystal surface (a). When ice-like waters attach onto the ice lattice, they are included in the ice crystal (b).

4.5. Conclusions

To conclude, the present study shows that microorganism-derived IBP and insect-derived IBP are both finely designed to make a complementary binding to single ice crystals for freeze tolerance, although these two organisms are very different. IBPs are expected various uses for medical and industrial field, where it is desirable to design new antifreeze molecules. This research provides the foundation for it.

References

1. Herbert, R.A. *The Ecology and physiology of psychrophilic microorganisms*. In *Microbes in Extreme Environments* (Herbert, R.A. & Codd, G.A., eds.) Academic Press: London, England, 1986; pp. 1–23.
2. Margesin, R.; Neuner, G.; Storey, K.B. Cold-loving microbes, plants, and animals—fundamental and applied aspects. *Naturwissenschaften* **2007**, *94*, 77–99. Doi: 10.1007/s00114-006-0162-6.
3. Hoshino, T.; Matsumoto, N. Cryophilic fungi to denote fungi in the cryosphere. *Fungal Biology Reviews*. **2012**, *26*, 102–105. Doi: 10.1016/j.fbr.2012.08.003.
4. Voets, I.K. From ice-binding proteins to bio-inspired antifreeze materials. *Soft Matter*. **2017**, *12*, 4808–4823, Doi: 10.1039/c6sm02867e.
5. Duman, J.G. Thermal-hysteresis-factors in overwintering insects. *J. Insect Physiol.* **1979**, *25*, 805–810. Doi: 10.1016/0022-1910(79)90083-0.
6. Phadtare, S. Recent developments in bacterial cold-shock response. *Curr Issues Mol Biol.* **2004**, *6*, 125–136. PMID: 15119823
7. Su, Y.; Jiang, X.; Wu, W.; Wang, M.; Hamid, M. I.; Xiang, M.; Liu, X. Genomic, transcriptomic, and proteomic analysis provide insights into the cold adaptation mechanism of the obligate psychrophilic fungus *Mrakia psychrophila*. *G3 (Bethesda)* **2016**, *6*, 3603–3613. Doi: 10.1534/g3.116.033308.
8. Raymond, J.A.; DeVries, A.L. Adsorption inhibition as a mechanism of freezing resistance in polar fishes. *Proc. Natl. Acad. Sci. USA* **1977**, *74*, 2589–2593. Doi: 10.1073/pnas.74.6.2589.
9. DeVries, A.L.; Wohlschlag, D.E. Freezing resistance in some Antarctic fishes. *Science* **1969**, *163*, 1073–1075, Doi: 10.1126/science.163.3871.1073.
10. Yokoyama, H. Supercooled water and its structure. *Bulletin of Yokohama City University. Natural Science* **2012**, *62*, 11–34.
11. Yokoyama, H.; Kannami, M.; Kanno, H. Existence of clathrate-like structures in supercooled water: X-ray diffraction evidence. *Chemical Physics Letters* **2008**, *463*, 99–102. Doi: 10.1016/j.cplett.2008.08.042.
12. Hobbs, P.V. *Ice Physics*; Oxford Univ Press: London, UK, 1974; pp. 461–523.
13. Mahatabuddin, S.; Tsuda, S. Applications of Antifreeze Proteins: Practical Use of the Quality Products from Japanese Fishes. *Adv Exp Med Biol.* **2018**, *1081*, 321–337. Doi: 10.1007/978-981-13-1244-1_17.
14. Hew, C.L.; Yang, D.S.C. Protein interaction with ice. *Eur J Biochem.* **1992**, *203*, 33–42. Doi:

- 10.1111/j.1432-1033.1992.tb19824.x.
15. Olijve, L.C.; Meister, K.; DeVries, A.L.; Duman, J.G.; Guo, S.; Bakker, H.J.; Voets, I.K. Blocking rapid ice crystal growth through nonbasal plane adsorption of antifreeze proteins. *Proc. Natl. Acad. Sci. USA* **2016**, *113*, 3740–3745. Doi: 10.1073/pnas.1524109113.
 16. Knight, C.A.; Cheng, C.C.; DeVries, A.L. Adsorption of α -helical antifreeze peptides on specific ice crystal surface planes. *Biophys. J.* **1991**, *59*, 409–418. Doi: 10.1016/S0006-3495(91)82234-2.
 17. Garnham, C.P.; Natarajan, A.; Middleton, A.J.; Kuiper, M.J.; Braslavsky, I.; Davies, P.L. Compound ice-binding site of an antifreeze protein revealed by mutagenesis and fluorescent tagging. *Biochemistry* **2010**, *49*, 9063–9071. Doi: 10.1021/bi100516e.
 18. Basu, K.; Garnham, C.P.; Nishimiya, Y.; Tsuda, S.; Braslavsky, I.; Davies, P. Determining the ice-binding planes of antifreeze proteins by fluorescence-based ice plane affinity. *JoVE* **2014**, *83*, e51185. Doi: 10.3791/51185.
 19. Rahman, A.T.; Arai, T.; Yamauchi, A.; Miura, A.; Kondo, H.; Ohyama, Y.; Tsuda, S. Ice recrystallization is strongly inhibited when antifreeze proteins bind to multiple ice planes. *Sci. Rep.* **2019**, *9*, 2212. Doi: 10.1038/s41598-018-36546-2.
 20. Kallungal, J.P. *The Growth of a single ice crystal parallel to the a-Axis in subcooled quiescent and flowing water*. Ph.D. Thesis, Syracuse University, Syracuse, NY, USA, 1975.
 21. Takamichi, M.; Nishimiya, Y.; Miura, A.; Tsuda, S. Fully active QAE isoform confers thermal hysteresis activity on a defective SP isoform of type III antifreeze protein. *FEBS J.* **2009**, *276*, 1471–1479. Doi: 10.1111/j.1742-4658.2009.06887.x.
 22. Scotter, A.J.; Marshall, C.B.; Graham, L.A.; Gilbert, J.A.; Garnham, C.P.; Davies, P.L. The basis for hyperactivity of antifreeze proteins. *Cryobiology* **2006**, *53*, 229–239. Doi: 10.1016/j.cryobiol.2006.06.006.
 23. Sazaki, G.; Zepeda, S.; Nakatsubo, S.; Yokoyama, E.; Furukawa, Y. (2010) Elementary steps at the surface of ice crystals visualized by advanced optical microscopy. *Proc. Natl. Acad. Sci. USA* **2010**, *107*, 19702–19707. Doi: 10.1073/pnas.1008866107.
 24. Nada, H.; Furukawa, Y. Antifreeze proteins: computer simulation studies on the mechanism of ice growth inhibition. *Polym J* **2012**, *44*, 690–698. Doi: 10.1038/pj.2012.13.
 25. Kristiansen, E.; Ramløv, H.; Hagen, L.; Pedersen, S.A.; Andersen, R.A.; Zachariassen, K.E. Isolation and characterization of hemolymph antifreeze proteins from larvae of the longhorn beetle *Rhagium inquisitor*. *Comp Biochem Physiol B Biochem Mol Biol.* **2005**, *142*, 90–97. Doi: 10.1016/j.cbpc.2005.06.004.
 26. Yeh, Y.; Feeney, R.H. Antifreeze proteins: structures and mechanisms of function. *Chem. Rev.* **1996**, *96*, 601–618. Doi: 10.1021/cr950260c.
 27. Anklam, M.R.; Firoozabadi, A. An interfacial energy mechanism for the complete inhibition

- of crystal growth by inhibitor adsorption. *J. Chem. Phys.* **2005**, *123*, 144708. Doi: 10.1063/1.2060689.
28. Celik, Y.; Graham, L.A.; Mok, Y.F.; Bar, M.; Davies, P.L.; Braslavsky, I. Superheating of ice crystals in antifreeze protein solutions. *Proc. Natl. Acad. Sci. USA* **2010**, *107*, 5423–5428, Doi: 10.1073/pnas.0909456107.
 29. Davies, P.L. Ice-binding proteins: a remarkable diversity of structures for stopping and starting ice growth. *TiBS*. **2017**, *39*, 548-555. Doi: 10.1016/j.tibs.2014.09.005.
 30. Barrett, J. Thermal hysteresis proteins. *Int. J. Biochem. Cell Biol.* **2001**, *33*, 105–117, Doi: 10.1016/s1357-2725(00)00083-2.
 31. Takamichi, M.; Nishimiya, Y.; Miura, A.; Tsuda, S. Effect of annealing time of an ice crystal on the activity of type III antifreeze protein. *FEBS J.* **2007**, *274*, 6469-6476. Doi: 10.1111/j.1742-4658.2007.06164.x.
 32. Lifshitz, I.M.; Slyozov, V.V. The kinetics of precipitation from supersaturated solid solutions. *J Phys Chem Solids* **1961**, *19*, 35–50. Doi: 10.1016/0022-3697(61)90054-3.
 33. Kahlweit, M. Ostwald ripening of precipitates. *Adv Colloid Interf Sci* **1975**, *5*, 1–35. Doi: 10.1016/0001-8686(75)85001-9.
 34. Knight, C.A.; Wen, D.; Laursen, R.A. Nonequilibrium antifreeze peptides and the recrystallization of ice. *Cryobiology* **1995**, *32*, 23–34. Doi: 10.1006/cryo.1995.1002.
 35. Knight, C.A.; DeVries, A.L.; Oolman, L.D. Fish antifreeze protein and the freezing and recrystallization of ice. *Nature* **1984**, *308*, 295–296. Doi: 10.1038/308295a0.
 36. Knight, C.A.; Hallett, J.; DeVries, A.L. Solute effects on ice recrystallization: an assessment technique. *Cryobiology* **1988**, *25*, 55–60. Doi: 10.1016/0011-2240(88)90020-X.
 37. Smallwood, M.; Worrall, D.; Byass, L.; Elias, L.; Ashford, D.; Doucet, C.J.; Holt, C.; Telford, J.; Lillford, P.; Bowles, D.J. Isolation and characterization of a novel antifreeze protein from carrot (*Daucus carota*). *Biochem J* **1999**, *340*, 385–391.PMCID: PMC1220261.
 38. Tomczak, M.M.; Marshall, C.B.; Gilbert, J.A.; Davies, P.L. A facile method for determining ice recrystallization inhibition by antifreeze proteins. *Biochim Biophys Res Commun* **2003**, *311*, 1041–1046. Doi: 10.1016/j.bbrc.2003.10.106.
 39. Zachariassen, K.E.; Kristiansen, E. Ice nucleation and antinucleation in nature. *Cryobiology* **2000**, *41*, 257–279. Doi: 10.1006/cryo.2000.2289.
 40. Duman, J.G. Antifreeze and Ice Nucleator Proteins in Terrestrial Arthropods. *Annu. Rev. Physiol.* **2001**, *63*, 327–357. Doi: 10.1146/annurev.physiol.63.1.327.
 41. Vrieling, A.S.O.; Aloï, A.; Olijve, L.L.C. Interaction of ice binding proteins with ice, water and ions. *Biointerphases* **2016**, *11*, 018906. Doi: 10.1116/1.4939462.
 42. Graether, S.P.; Kuiper, M.J.; Gagné, S.M.; Walker, V.K.; Jia, Z.; Sykes, B.D.; Davies, P.L. β -Helix structure and ice-binding properties of a hyperactive antifreeze protein from an insect.

- Nature* **2000**, 406, 325–328. Doi: 10.1038/35018610.
43. Jia, Z.; Davies, P.L. Antifreeze proteins: an unusual receptor–ligand interaction. *Trends Biochem. Sci.* **2002**, 27, 101–106. Doi: 10.1016/S0968-0004(01)02028-X.
 44. Duman, J.G. Insect antifreezes and ice-nucleating agents. *Cryobiology* **1982**, 19, 613–627. Doi: 10.1016/0011-2240(82)90191-2.
 45. Duman, J.; Olsen, T.M. Thermal hysteresis protein activity in bacteria, fungi and phylogenetically diverse plants. *Cryobiology* **1993**, 30, 322–328. Doi: 10.1006/cryo.1993.1031.
 46. Worrall, D.; Elias, L.; Ashford, D.; Smallwood, M.; Sidebottom, C.; Lillford, P.; Telford, J.; Holt, C.; Bowles, D. A carrot leucine-rich-repeat protein that inhibits ice recrystallization. *Science* **1998**, 282, 115–117. Doi: 10.1126/science.282.5386.115.
 47. Yu, S.O.; Brown, A.; Middleton, A.J.; Tomczak, M.M.; Walker, V.K.; Davies, P.L. Ice restructuring inhibition activities in antifreeze proteins with distinct differences in thermal hysteresis. *Cryobiology* **2010**, 61, 327–334. Doi: 10.1016/j.cryobiol.2010.10.158.
 48. Budke, C.; Koop, T. Inhibition of Recrystallization. *Antifreeze proteins volume 2. Biochemistry, Molecular Biology and Applications* (Eds: H. Ramløv. D. S. Friis.) Springer Nature, Switzerland, **2020**; pp. 159–184. Doi: 10.1007/978-3-030-41948-6_7.
 49. Sidebottom, C.; Buckley, S.; Pudney, P.; Twigg, S.; Jarman, C.; Holt, C.; Telford, J.; MaArthur, A.; Worrall, D.; Hubbard, R.; Lillford, P. Heat-stable antifreeze protein from grass. *Nature* **2000**, 406, 256. Doi: 10.1038/35018639.
 50. Guo, S.; Garnham, C.P.; Whitney, J.C.; Graham, L.A. Davies, P.L. Re-evaluation of a bacterial antifreeze protein as an adhesin with ice-binding activity. *PLoS ONE* **2012**, 7, e48805. Doi: 10.1371/journal.pone.0048805.
 51. Vance, T.D.; Graham, L.A.; Davies, P.L. (2018). An ice-binding and tandem beta-sandwich domain-containing protein in *Shewanella frigidimarina* is a potential new type of ice adhesin. *FEBS J.* **2018**, 285, 1511–1527. Doi: 10.1111/febs.14424.
 52. Raymond, J.A. Algal ice-binding proteins change the structure of sea ice. *Proc. Natl. Acad. Sci. USA* 2011, 108, E198. Doi: 10.1073/pnas.1106288108.
 53. Bayer-Giraldi, M.; Weikusat, I.; Besir, H.; Dieckmann, G. Characterization of an antifreeze protein from the polar diatom *Fragilariopsis cylindrus* and its relevance in sea ice. *Cryobiology* **2011**, 63, 210–219, Doi: 10.1016/j.cryobiol.2011.08.006.
 54. Raymond, J.A.; Janech, M.G.; Fritsen, C.H. Novel ice-binding proteins from a psychrophilic Antarctic alga (Chlamydomonadaceae, Chlorophyceae). *J. Phycol.* **2009**, 45, 130–136. Doi: 10.1111/j.1529-8817.2008.00623.x.
 55. Krembs, C.; Eicken, H.; Deming, J.W. Exopolymer alteration of physical properties of sea ice and implications for ice habitability and biogeochemistry in a warmer Arctic. *Proc. Natl.*

- Acad. Sci. USA* **2011**, *108*, 3653–3658. Doi: 10.1073/pnas.1100701108.
56. Burcham, T.S.; Osuga, D.T.; Rao, B.N.N.; Bush, C.A.; Feeney, R.E. Purification and primary sequences of the major arginine-containing antifreeze glycopeptides from the fish *Eleginus gracilis*. *J Biol Chem* **1986**, *261*, 6384–6389. Doi: 10.1016/S0021-9258(19)84573-8.
57. Burcham, T.S.; Osuga, D.T.; Yeh, Y.; Feeney, R.E. A kinetic description of antifreeze glycoprotein activity. *J Biol Chem* **1986**, *261*, 6390–6397. Doi: 10.1016/S0021-9258(19)84574-X.
58. Harding, M.M.; Anderberg, P.I.; Haymet, A.D.J. ‘Antifreeze’ glycoproteins from polar fish. *Eur J Biochem* **2003**, *270*, 1381–1392. Doi: 10.1046/j.1432-1033.2003.03488.x.
59. Gibson, M.I. Slowing the growth of ice with synthetic macromolecules: beyond antifreeze (glyco) proteins. *Polym Chem* **2010**, *1*, 1141–1152. Doi: 10.1039/c0py00089b.
60. Tachibana, Y.; Fletcher, G.L.; Fujitani, N.; Tsuda, S.; Monde, K.; Nishimura, S-I. Antifreeze glycoproteins: elucidation of the structural motifs that are essential for antifreeze activity. *Angew Chem Int Ed* **2004**, *43*, 856–862. Doi: 10.1002/anie.200353110.
61. Duman, J.G.; DeVries, A.L. Isolation, characterization, and physical properties of protein antifreezes from the winter flounder, *Pseudopleuronectes americanus*. *Comp Biochem Physiol* **1976**, *54B*, 375–380. Doi: 10.1016/0305-0491(76)90260-1.
62. Yang, D.S.; Sax, M.; Chakrabarty, A.; Hew, C.L. Crystal structure of an antifreeze polypeptide and its mechanistic implications. *Nature* **1988**, *333*, 232–237. Doi: 10.1038/333232a0.
63. Sicheri, F.; Yang, D.S.C. Ice-binding structure and mechanism of an antifreeze protein from winter flounder. *Nature* **1995**, *375*, 427–431. Doi: 10.1038/375427a0.
64. Harding, M.M.; Ward, L.G.; Haymet, A.D.J. Type I ‘antifreeze’ proteins: structure-activity studies and mechanisms of ice growth inhibition. *Eur J Biochem* **1999**, *264*, 653–665. Doi: 10.1046/j.1432-1327.1999.00617.x.
65. Marshall, C.B.; Fletcher, G.L.; Davies, P.L. Hyperactive antifreeze protein in a fish. *Nature* **2004**, *429*, 153. Doi: 10.1038/429153a.
66. Sun, T.; Lin, F.H.; Campbell, R.L.; Allingham, J.S.; Davies, P.L. An antifreeze protein folds with an interior network of more than 400 semi-clathrate waters. *Science* **2014**, *343*, 795–798. Doi: 10.1126/science.1247407.
67. Slaughter, D.; Fletcher, G.L.; Ananthanarayanan, V.S.; Hew, C.L. Antifreeze proteins from the sea raven, *Hemitripterus americanus*. *J Biol Chem* **1981**, *256*, 2022–2026. Doi: 10.1016/S0021-9258(19)69910-2.
68. Ewart, K.V.; Fletcher, G.L. Isolation and characterization of antifreeze proteins from smelt (*Osmerus mordax*) and Atlantic herring (*Clupea harengus harengus*). *Can J Zool* **1990**, *68*,

- 1652–1658. Doi: 10.1139/z90-245.
69. Yamashita, Y.; Miura, R.; Takemoto, Y.; Tsuda, S.; Kawahara, H.; Obata, H. Type II antifreeze protein from a mid-latitude freshwater fish, Japanese smelt (*Hypomesus nipponensis*). *Biosci Biotechnol Biochem* **2003**, *67*, 461–466. Doi: doi.org/10.1271/bbb.67.461.
 70. Nishimiya, Y.; Kondo, H.; Takamichi, M.; Sugimoto, H.; Suzuki, M.; Miura, A.; Tsuda, S. Crystal structure and mutational analysis of Ca²⁺-independent type II antifreeze protein from longsnout poacher, *Brachyopsis rostratus*. *J. Mol. Biol.* **2008**, *382*, 734–746. Doi: 10.1016/j.jmb.2008.07.042.
 71. Gronwald, W.; Loewen, M.C.; Lix, B.; Daugulis, A.J.; Sönnichsen, F.D.; Davies, P.L.; Sykes, B.D. The solution structure of type II antifreeze protein reveals a new member of the lectin family. *Biochemistry* **1998**, *37*, 4712–4721. Doi: 10.1021/bi972788c.
 72. Liu, Y.; Li, Z.; Lin, Q.; Kosinski, J.; Seetharaman, J.; Bujnicki, J.M.; Sivaraman, J.; Hew, C-L. Structure and evolutionary origin of Ca²⁺-dependent herring type II antifreeze protein. *PLoS One* **2007**, *6*, e548. Doi: 10.1371/journal.pone.0000548.
 73. Li, X-M.; Trinh, K-Y.; Hew, C.L.; Buettner, B.; Baenziger, J.; Davies, P.L. Structure of an antifreeze polypeptide and its precursor from the ocean pout, *Macrozoarces americanus*. *J Biol Chem* **1985**, *260*, 12904–12909. Doi: 10.1016/S0021-9258(17)38811-7.
 74. Sönnichsen, F.D.; Sykes, B.D.; Chao, H.; Davies, P.L. The nonhelical structure of antifreeze protein type III. *Science* **1993**, *259*, 1154–1157. Doi: 10.1126/science.8438165.
 75. Antson, A.A.; Smith, D.J.; Roper, D.I.; Lewis, S.; Caves, L.S.D.; Verma, C.S.; Buckley, S.L.; Lillford, P.J.; Hubbard, R.E. Understanding the mechanism of ice binding by type III antifreeze proteins. *J Mol Biol* **2001**, *305*, 875–889. Doi: 10.1006/jmbi.2000.4336.
 76. Sönnichsen, F. D.; DeLuca, C.I.; Davies, P.L.; Sykes, B.D. Refined solution structure of type III antifreeze protein: hydrophobic groups may be involved in the energetics of the protein–ice interaction. *Structure* **1996**, *4*, 1325–1337. Doi: 10.1016/S0969-2126(96)00140-2.
 77. Jia, Z.; DeLuca, C.I.; Chao, H.; Davies, P.L. Structural basis for the binding of a globular antifreeze protein to ice. *Nature* **1996**, *384*, 285–288. Doi: 10.1038/384285a0.
 78. Nishimiya, Y.; Sato, R.; Takamichi, M.; Miura, A.; Tsuda, S. Co-operative effect of the isoforms of type III antifreeze protein expressed in Notched-fin eelpout, *Zoarces elongatus* Kner. *FEBS J.* **2005**, *272*, 482–492. Doi: 10.1111/j.1742-4658.2004.04490.x.
 79. Deng, G.; Andrews, D.W.; Laursen, R.A. Amino acid sequence of a new type of antifreeze protein, from the longhorn sculpin *Myoxocephalus octodecimspinosis*. *FEBS Lett.* **1997**, *402*, 17–20. Doi: 10.1016/S0014-5793(96)01466-4.
 80. Gauthier, S.Y.; Scotter, A.J.; Lin, F.-H.; Baardsnes, J.; Fletcher, G.L. and Davies, P.L. A re-evaluation of the role of type IV antifreeze protein. *Cryobiology* **2008**, *57*, 292–296. Doi:

10.1016/j.cryobiol.2008.10.122.

81. Graether, S.P.; Sykes, B.D. Cold survival in freeze-intolerant insects: The structure and function of β -helical antifreeze proteins. *Eur. J. Biochem.* **2004**, *271*, 3285-3296. Doi: 10.1111/j.1432-1033.2004.04256.x.
82. Graham, L.A.; Liou, Y.-C.; Walker, V.K.; Davies, P.L. Hyperactive antifreeze protein from beetles. *Nature* **1997**, *388*, 727–728. Doi: 10.1038/41908.
83. Liou, Y.-C.; Thibault, P.; Walker, V.K.; Davies, P.L.; Graham, L.A. A complex family of highly heterogeneous and internally repetitive hyperactive antifreeze proteins from the beetle *Tenebrio molitor*. *Biochemistry* **1999**, *38*, 11415–11424. Doi: 10.1021/bi990613s.
84. Liou, Y.-C.; Tocij, A.; Davies, P.L.; Jia, Z. Mimicry of ice structure by surface hydroxyls and water of a β -helix antifreeze protein. *Nature* **2000**, *406*, 322–324. Doi: 10.1038/35018604.
85. Kristiansen, E.; Ramløv, H.; Højrup, P.; Pedersen, S.A.; Hagen, L.; Zachariassen, K.E. Structural characteristics of a novel antifreeze protein from the longhorn beetle *Rhagium inquisitor*. *Insect Biochem. Mol. Biol.* **2011**, *41*, 109–117. Doi: 10.1016/j.ibmb.2010.11.002.
86. Zachariassen, K.E.; Li, N.G.; Laugsand, A.E.; Kristiansen, E.; Pedersen, S.A. Is the strategy for cold hardiness in insects determined by their water balance? A study on two closely related families of beetles: Cerambycidae and Chrysomelidae. *J. Comp. Physiol. B* **2008**, *178*, 977–984. Doi: 10.1007/s00360-008-0284-6.
87. Hakim, A.; Nguyen, J.B.; Basu, K.; Zhu, D.F.; Thakral, D.; Davies, P.L.; Isaacs, F.J.; Modis, Y.; Meng, W. Crystal structure of an insect antifreeze protein and its implications for ice binding. *J. Biol. Chem.* **2013**, *288*, 12295–12304. Doi: 10.1074/jbc.M113.450973.
88. Lin, F.-H.; Davies, P.L.; Graham, L.A. The Thr- and Ala-rich hyperactive antifreeze protein from Inchworm folds as a flat silk-like β -helix. *Biochemistry* **2011**, *50*, 4467–4478. Doi: 10.1021/bi2003108.
89. Graham, L.A.; Davies, P.L. Glycine-rich antifreeze proteins from snow fleas. *Science* **2005**, *310*, 461. Doi: 10.1126/science.1115145.
90. Pentelute, B.L.; Gates, Z.P.; Tereshko, V.; Dashnau, J.L.; Vanderkooi, J.M.; Kossiakoff, A.A.; Kent, S.B. X-ray structure of snow flea antifreeze protein determined by racemic crystallization of synthetic protein enantiomers. *J. Am. Chem. Soc.* **2008**, *130*, 9695–9701. Doi: 10.1021/ja8013538.
91. Mok, Y.F.; Lin, F.H.; Graham, L.A.; Celik, Y.; Braslavsky, I.; Davies, P.L. Structural basis for the superior activity of the large isoform of snow flea antifreeze protein. *Biochemistry* **2010**, *49*, 2593–2603. Doi: 10.1021/bi901929n.
92. Scholl, C.L.; Tsuda, S.; Graham, L.A.; Davies, P.L. Crystal waters on the nine polyproline type II helicalbundle springtail antifreeze protein from *Granisotoma rainieri* match the ice lattice. *FEBS.J* **2021**, *288*, 15717. Doi: 10.1111/febs.15717.

93. Urrutia, M.E.; Duman, J.G.; Knight, C.A. Plant thermal hysteresis proteins. *Biochim Biophys Acta*. **1992**, *1121*, 199–206. Doi: 10.1016/0167-4838(92)90355-h.
94. Middleton, A.J.; Marshall, C.B.; Faucher, F.; Bar-Dolev, M.; Braslavsky, I.; Campbell, R.L.; Walker, V.K.; Davies, P.L. Antifreeze protein from freeze-tolerant grass has a beta-roll fold with an irregularly structured ice-binding site. *J. Mol. Biol.* **2012**, *416*, 713–724. Doi: 10.1016/j.jmb.2012.01.032.
95. Wang, Y.; Graham, L.A.; Han, Z.; Eves, R.; Gruneberg, A.K.; Campbell, R.L.; Zhang, H.; Davies, P.L. Carrot ‘antifreeze’ protein has an irregular ice-binding site that confers weak freezing point depression but strong inhibition of ice recrystallization. *Biochemical Journal* **2020**, *477*, 2179–2192. Doi: 10.1042/BCJ20200238.
96. Lee, J. H.; Park, A.K.; Do, H.; Park, K.S.; Moh, S.H.; Chi, Y.M.; Kim, H.J. Structural basis for antifreeze activity of ice-binding protein from arctic yeast. *J Biol Chem* **2012**, *287*, 11460–11468. Doi: 10.1074/jbc.M111.331835.
97. Kondo, H.; Hanada, Y.; Sugimoto, H.; Hoshino, T.; Garnham, C.P.; Davies, P.L.; Tsuda, S. Ice-binding site of snow mold fungus antifreeze protein deviates from structural regularity and high conservation. *Proc. Natl. Acad. Sci. USA* **2012**, *109*, 9360–9365. Doi: 10.1073/pnas.1121607109.
98. Raymond J.A.; Fritsen, C.; Shen, K. An ice-binding protein from an Antarctic sea ice bacterium. *FEMS Microbiol Ecol* **2007**, *61*, 214–221. Doi: 10.1111/j.1574-6941.2007.00345.x.
99. Lee, J.K.; Park, K.S.; Park, S.; Park, H.; Song, Y.H.; Kang, S-H.; Kim, H.J. An extracellular ice-binding glycoprotein from an Arctic psychrophilic yeast. *Cryobiology* **2010**, *60*, 222–228 Doi: 10.1016/j.cryobiol.2010.01.002.
100. Hoshino, T.; Kiriaki, M.; Ohgiya, S.; Fujiwara, M.; Kondo, H.; Nishimiya, Y.; Yumoto, I.; Tsuda, S. Antifreeze proteins from snow mold fungi. *Can J Bot* **2003**, *81*, 1175–1181. Doi: 10.1139/b03-116.
101. Janech, M.G.; Krell, A.; Mock, T.; Kang, J.S.; Raymond, J.A. Ice-binding protein from sea ice diatoms. *J phycol* **2006**, *42*, 410–416. Doi: 10.1111/j.1529-8817.2006.00208.x.
102. Kiko, R. Acquisition of freeze protection in a sea-ice crustacean through horizontal gene transfer? *Polar Biol.* **2010**, *33*, 543–556, Doi: 10.1007/s00300-009-0732-0.
103. Vance, T.D.R.; Bayer-Giraldi, M.; Davies, P.L.; Mangiagalli, M. Ice-binding proteins and the ‘domain of unknown function’ 3494 family. *FEBS J.* **2019**, *286*, 855–873. Doi: 10.1111/febs.14764.
104. Wang, C.; Oliver, E.E.; Christner, B.C.; Luo, B-H. Functional Analysis of a Bacterial Antifreeze Protein Indicates a Cooperative Effect between Its Two Ice-Binding Domains. *Biochemistry* **2016**, *55*, 3975–3983. Doi: 10.1021/acs.biochem.6b00323.

105. Wang, C.; Pakhomova, S.; Newcomer, M.E.; Christner, B.C.; Luo, B.H. Structural basis of antifreeze activity of a bacterial multi-domain antifreeze protein. *PLoS ONE* **2017**, *12*, e0187169. Doi: 10.1371/journal.pone.0187169.
106. Garnham, C.P.; Campbell, R.L.; Davies, P.L. Anchored clathrate waters bind antifreeze proteins to ice. *Proc. Natl. Acad. Sci. USA* **2011**, *108*, 7363–7367. Doi: 10.1073/pnas.1100429108.
107. Sharp, K.A. The remarkable hydration of the antifreeze protein Maxi: A computational study. *J. Chem. Phys.* 2014, *141*, 22D510, doi:10.1063/1.4896693.
108. Arai, T.; Nishimiya, Y.; Ohyama, Y.; Kondo, H.; Tsuda, S. Calcium-binding generates the semi-clathrate waters on a type II antifreeze protein to adsorb onto an ice crystal surface. *Biomolecules* 2019, *9*, 162. Doi:10.3390/biom9050162.
109. Mahatabuddin, S.; Fukami, D.; Arai, T.; Nishimiya, Y.; Shimizu, R.; Shibazaki, C.; Kondo, H.; Adachi, M.; Tsuda, S. Polypentagonal ice-like water networks emerge solely in an activity-improved variant of ice-binding protein. *Proc. Natl. Acad. Sci. USA* 2018, *115*, 5456–5461. Doi:10.1073/pnas.1800635115.
110. Sun, T.; Gauthier, S.Y.; Campbell, R.L.; Davies, P.L. Revealing Surface Waters on an Antifreeze Protein by Fusion Protein Crystallography Combined with Molecular Dynamic Simulations. *J. Phys. Chem. B* **2015**, *119*, 12808–12815. Doi: 10.1021/acs.jpcc.5b06474.
111. Stchigel, A.M.; Cano, J.; Cormack W.M.; Guarro, J. *Antarctomyces psychrotrophicus* gen. et sp. nov., a new ascomycete from Antarctica. *Mycol Res* **2001**, *105*, 377–382. Doi: 10.1017/S0953756201003379.
112. Gonçalves, V.N.; Vaz, A.B.; Rosa, C.A.; Rosa, L.H. Diversity and distribution of fungal communities in lakes of Antarctica. *FEMS Microbiol Ecol* **2012**, *82*, 459–471. Doi: 10.1111/j.1574-6941.2012.01424.x.
113. Loque, C.P.; Medeiros, A.O.; Pellizzari, F.M.; Oliveira, E.C.; Rosa, C.A.; Rosa, L.H. Fungal community associated with marine macroalgae from Antarctica. *Polar Biol* **2010**, *33*, 641–648. Doi: 10.1007/s00300-009-0740-0.
114. Xiao, N.; Suzuki, K.; Nishimiya, Y.; Kondo, H.; Miura, A.; Tsuda, S.; Hoshino, T. Comparison of functional properties of two fungal antifreeze proteins from *Antarctomyces psychrotrophicus* and *Typhula ishikariensis*. *FEBS J.* **2010**, *277*, 394–403. Doi: 10.1111/j.1742-4658.2009.07490.x.
115. Arai, T.; Fukami, D.; Hoshino, T.; Kondo, H.; Tsuda, S. Ice-binding proteins from the fungus *Antarctomyces psychrotrophicus* possibly originate from two different bacteria through horizontal gene transfer. *FEBS J.* **2018**, *286*, 946–962. Doi: 10.1111/febs.14725.
116. Asahina, E.; Ohyama, Y. Cold Resistance in insects wintering in decayed wood. *Low Temperature Science (Hokkaido University Library)* **1969**, *27*, 143–152.

(<http://hdl.handle.net/2115/17760>).

117. Duman, J.G.; Verleye, N.L.-D.; Goetz, F.W.; Wu, D.W.; Andorfer, C.A.; Benjamin, T.; Parmelee, D.D. Molecular characterization and sequencing of antifreeze proteins from larvae of the beetle *Dendroides canadensis*. *J. Comp. Physiol. B* **1998**, *168*, 225–232. Doi: 10.1007/s003600050140.
118. Ma Y.; Hou, F.; Ma, J. Seasonal changes in cold tolerance of desert beetle *Anatolica polita borealis* (Coleoptera: Tenebrionidae) and their physiological mechanisms. *Acta Entomol. Sin.* **2009**, *52*, 372–379.
119. Qiu, L.; Wang, Y.; Wang, J.; Zhang, F.; Ma, J. Expression of biologically active recombinant antifreeze protein His-MpAFP149 from the desert beetle (*Microdera punctipennis dzungarica*) in *Escherichia coli*. *Mol. Biol. Reports*, **2010**, *37*, 1725–1732. Doi: 10.1007/s11033-009-9594-3.
120. Kim, S.I.; Kim, J.I. Review of family Lucanidae (Insecta: Coleoptera) in Korea with the description of one new species. *Entomol. Res.* **2010**, *40*, 55-81. Doi: 10.1111/j.1748-5967.2009.00263.x.
121. Brown's Beetles. Available online: <https://abrowntks.weebly.com/dorcus-hopei.html> (accessed on 14 March 2021).
122. Ball, P. Water as an active constituent in cell biology. *Chem. Rev.* 2008, *108*, 74–108, Doi: 10.1021/cr068037a. Ball, P. Water as an active constituent in cell biology. *Chem. Rev.* **2008**, *108*, 74–108, doi:10.1021/cr068037a.
123. Levy, Y.; Onuchic, J.N. Water mediation in protein folding and molecular recognition. *Annu. Rev. Biophys. Biomol. Struct.* **2006**, *35*, 389–415. Doi: 10.1146/annurev.biophys.35.040405.102134.
124. Andorfer, C.A.; Duman, J.G. Isolation and characterization of cDNA clones encoding antifreeze proteins of the pyrochroid beetle *Dendroides canadensis*. *J. Insect Physiol.* **2000**, *46*, 365–372. Doi: 10.1016/S0022-1910(99)00189-4.
125. Hanada, Y.; Nishimiya, Y.; Miura, A.; Tsuda, S.; Kondo, H. Hyperactive antifreeze protein from an Antarctic sea ice bacterium *Colwellia* sp. has a compound ice-binding site without repetitive sequence. *FEBS J.* **2014**, *281*, 3576–3590. Doi: 10.1111/febs.12878.
126. McPherson, A. Current approaches to macromolecular crystallization. *Eur. J. Biochem.* 1990, *189*, 1–23. Doi: 10.1111/j.1432-1033.1990.tb15454.x.
127. Igarashi, N.; Ikuta, K.; Miyoshi, T.; Matsugaki, N.; Yamada, Y.; Yousef, M.S.; Wakatsuki, S. X-ray beam stabilization at BL-17A, the protein microcrystallography beamline of the Photon Factory. *J. Synchrotron Rad.* **2008**, *15*, 292–295. Doi: 10.1107/S0909049507067118.
128. Kabsch, W. Automatic processing of rotation diffraction data from crystals of initially unknown symmetry and cell constants. *J. Appl. Cryst.* **1993**, *26*, 795–800, Doi:

- 10.1107/S0021889893005588.
129. Winn, M.D.; Ballard, C.C.; Cowtan, K.D.; Dodson, E.J.; Emsley, P.; Evans, P.R.; Keegan, R.M.; Krissinel, E.B.; Leslie, A.G.; McCoy, A. Overview of the CCP4 suite and current developments. *Acta Crystallogr. D Biol. Crystallogr.* **2011**, *67*, 235–242, Doi: 10.1107/S0907444910045749.
130. Adams, P.D.; Afonine, P.V.; Bunkoczi, G.; Chen, V.B.; Davis, I.W.; Echols, N.; Headd, J.J.; Hung, L.W.; Kapral, G.J.; Grosse-Kunstleve, R.W. PHENIX: A comprehensive Python-based system for macromolecular structure solution. *Acta Crystallogr. D Biol. Crystallogr.* **2010**, *66*, 213–221. Doi: 10.1107/S0907444909052925.
131. Murshudov, G.N.; Vagin, A.A.; Dodson, E.J. Refinement of macromolecular structures by the maximum-likelihood method. *Acta Crystallogr. D Biol. Crystallogr.* **1997**, *53*, 240–255, Doi: 10.1107/S0907444996012255.
132. Emsley, P.; Lohkamp, B.; Scott, W.G.; Cowtan, K. Features and development of Coot. *Acta Crystallogr. D Biol. Crystallogr.* **2010**, *66*, 486–501. Doi: 10.1107/S0907444910007493.
133. Brunger, A.T. Free R value: A novel statistical quantity for assessing the accuracy of crystal structures. *Nature* **1992**, *355*, 472–475 Doi: 10.1038/355472a0.
134. Mahatabuddin, S.; Hanada, Y.; Nishimiya, Y.; Miura, A.; Kondo, H.; Davies, P.L.; Tsuda, S. Concentration-dependent oligomerization of an alpha-helical antifreeze polypeptide makes it hyperactive. *Sci. Rep.* **2017**, *7*, 42501 Doi: 10.1038/srep42501.
135. Tsuda, S.; Yamauchi, A.; Moffiz Uddin Khan, N.M.; Arai, T.; Mahatabuddin, S.; Miura, A.; Kondo, H. Fish-derived antifreeze proteins and antifreeze glycoprotein exhibit a different ice-binding property with increasing concentration. *Biomolecules* **2020**, *10*, 423, Doi: 10.3390/biom10030423.
136. Cheng, J.; Hanada, Y.; Miura, A.; Tsuda, S.; Kondo, H. Hydrophobic ice-binding sites confer hyperactivity of an antifreeze protein from a snow mold fungus. *Biochem. J.* **2016**, *473*, 4011–4026. Doi: 10.1042/BCJ20160543.
137. Vance, T.D.R.; Graham, L.A.; Davies, P.L. An ice-binding and tandem beta-sandwich domain-containing protein in *Shewanella frigidimarina* is a potential new type of ice adhesin. *FEBS J.* **2018**, *285*, 1511–1527. Doi: 10.1111/febs.14424.
138. Do, H.; Kim, S.J.; Kim, H.J.; Lee, J.H. Structure-based characterization and antifreeze properties of a hyperactive ice-binding protein from the Antarctic bacterium *Flavobacterium frigoris* PS1. *Acta Crystallogr. Sect D Biol. Crystallogr.* **2014**, *70*, 1061–1073. Doi: 10.1107/S1399004714000996.
139. Mangiagalli, M.; Sarusi, G.; Kaleda, A.; Dolev, M.B.; Nardone, V.; Vena, V.F.; Lotti, M.; Nardini, M. Structure of a bacterial ice binding protein with two face of interaction with ice. *FEBS J.* **2018**, *285*, 1635–1666. Doi: 10.1111/febs.14434.

140. Leinala, E.K.; Davies, P.L.; Jia, Z. Crystal structure of beta-helical antifreeze protein points to a general ice binding model. *Structure* **2002**, *10*, 619–627. Doi: 10.1016/S0969-2126(02)00745-1.
141. Jeffrey, G.A. *An Introduction to Hydrogen Bonding*; Oxford University, Oxford, NY, USA, 1997.
142. Luzar, A.; Chandler, D. Effect of environment on hydrogen bond dynamics in liquid water. *Phys. Rev. Lett.* **1996**, *76*, 928–931. Doi: 10.1103/PhysRevLett.76.928.
143. Mantz, Y.A.; Geiger, F.M.; Molina, L.T.; Molina, M.J.; Trout, B.L. First-principles molecular-dynamics study of surface disordering of the (0001) face of hexagonal ice. *J. Chem. Phys.* **2000**, *113*, 10733–10743. Doi: 10.1063/1.1323959.
144. Hayward, J.A.; Haymet, A.D.J. The ice/water interface: Molecular dynamics simulations of the basal, prism, {2021}, and {2110} Interfaces of Ice Ih. *J. Chem. Phys.* **2001**, *114*, 3713–3726. Doi: 10.1063/1.455363.
145. Gallagher, K.R.; Sharp, K.A. Analysis of thermal hysteresis protein hydration using the random network model. *Biophys. Chem.* **2003**, *105*, 195–209. Doi: 10.1016/S0301-4622(03)00087-5.
146. Yang, C.; Sharp, K.A. The mechanism of the type III antifreeze protein action: A computational study. *Biophys Chem.* **2004**, *109*, 137–148. Doi: 10.1016/j.bpc.2003.10.024.
147. Kim, S.I.; Farrel, B.D. Phylogeny of world stag beetles (Coleoptera: Lucanidae) reveals a Gondwanan origin of Darwin's stag beetle. *Mol. Phylogenet. Evol.* **2015**, *86*, 35–48. Doi: 10.1016/j.ympev.2015.02.015.
148. Tournant, P.; Joseph, L.; Goka, K.; Couchamp, F. The rarity and overexploitation paradox: Stag beetle collections in Japan. *Biodivers. Conserv.* **2012**, *21*, 1425–1440. Doi: 10.1007/s10531-012-0253-y.
149. Goka, K.; Kojima, H.; Okabe, K. Biological invasion caused by commercialization of stag beetles in Japan. *Global Environ. Res.* **2004**, *8*, 67–74. ISSN: 1343-8808.
150. Kristiansen, E.; Zachariassen, K.E. The mechanism by which fish antifreeze proteins cause thermal hysteresis. *Cryobiology* **2005**, *51*, 262–280. Doi: 10.1016/j.cryobiol.2005.07.007.
151. Duman, J.G.; Newton, S. S. Insect Antifreeze Proteins. In *Antifreeze Proteins Volume 1* (Eds: H. Ramløv, D. S. Eriis), Springer Nature, Switzerland, **2020**; pp. 131–188. Doi: 10.1007/978-3-030-41929-5_6.
152. Hosoya, T.; Honda, M.; Araya, K. Genetic variation of 16S rRNA gene observed in *Ceruchus lignarius* and *Dorcus rectus rectus* (Coleoptera; Lucanidae). *Entomol. Sci.* **2001**, *4*, 335–344. ISSN: 13438786.
153. Chen, Y.; Liu, J.; Cao, Y.; Zhou, S.; Wan, X. Two new complete mitochondrial genomes of *Dorcus* stag beetles (Coleoptera, Lucanidae). *Gens Genom.* **2018**, *40*, 873–880. Doi:

- 10.1007/s13258-018-0699-8.
154. Bar-Dolev, M.; Celik, Y.; Wettlaufer, J.S.; Davies, P.L.; Braslavsky, I. New insights into ice growth and melting modifications by antifreeze proteins. *J. R. Soc. Interface* **2012**, *9*, 3249-3259. Doi: 10.1098/rsif.2012.0388.
155. Graham, L. A.; Walker, V. K.; Davies, P. L. Developmental and environmental regulation of antifreeze proteins in the mealworm beetle *Tenebrio molitor*. *Eur. J. Biochem.* **2000**, *267*, 6452-6458. Doi: 10.1046/j.1432-1327.2000.01734.x.
156. Wang, L.; Duman, J.G. Antifreeze proteins of the beetle *Dendroides canadensis* enhance one another's activities. *Biochemistry* **2005**, *44*, 10305-10312. Doi: 10.1021/bi050728y.
157. Graham, L.A.; Qin, W.; Lougheed, S.C.; Davies, P.L.; Walker, V.K. Evolution of hyperactive, repetitive antifreeze proteins in beetles. *J. Mol. Evol.* **2007**, *64*, 387-398. Doi: 10.1007/s00239-005-0256-3.
158. Qin, W; Walker, V.K. *Tenebrio molitor* antifreeze protein gene identification and regulation. *Gene*, *376*, 1423-149 (2006). Doi: 10.1016/j.gene.2005.10.003.
159. Wang, S.; Amornwittawat, N.; Juwita, V.; Kao, Y.; Duman, J.G.; Pascal, T. A.; Goddard III, W.A.; Wen, X. Arginine, a key residue for the enhancing ability of an antifreeze protein of the beetle *Dendroides canadensis*. *Biochemistry* **2009**, *48*, 9696-9703. Doi: 10.1021/bi901283p.
160. LaVallie, E.R.; Lu, Z.E.; Diblasio-Smith, A.; Collins-Racie, L.A.; McCoy, J.M. Thioredoxin as a fusion partner for production of soluble recombinant proteins in *Escherichia coli*. *Methods. Enzymol.* **2000**, *326*, 322-340. Doi: 10.1016/s0076-6879(00)26063-1.
161. Liou, Y.-C.; Daley, M.E.; Graham, L.A.; Kay, C.M.; Walker, V.K.; Sykes, B.D.; Davies, P.L. Folding and structural characterization of highly disulfide-bonded beetle antifreeze protein produced in bacteria. *Protein Expr. Purif.* **2000**, *19*, 148-157. Doi: 10.1006/prev.2000.1219.
162. Marshall, C.B.; Daley, M.E.; Sykes, B.D.; Davies, P.L. Enhancing the activity of a β -helical antifreeze protein by the engineered addition of Coils. *Biochemistry* **2004**, *43*, 11637-11646. Doi: 10.1021/bi0488909.
163. Emmanuel, F.A.; Toussaint, A.; Seidel, M.; Arriaga-Varela, E.; Hájek, J.; Král, D.; Sekerka, L.; Short, A.E.Z.; Fikáček, M. The peril of dating beetles. *Syst. Entomol.* **2017**, *42*, 1-10. Doi: 10.1111/syen.12198.
164. Henderson C.M.; Shen, S.Z.; Gradstein, F.M.; Agterberg, F.P. The Permian Period. In *The Geologic Time Scale 2020*; Gradstein, F.M, Ogg, J.G., Schmitz, M.D., Ogg, G.M. Eds; Elsevier, Amsterdam, Holland, 2012; pp. 653-679. Doi: 10.1016/B978-0-12-824360-2.00024-3.
165. Graham, L.A.; Boddington, M.E.; Holmstrup, M.; Davies, P.L. Antifreeze protein complements cryoprotective dehydration in the freeze-avoiding springtail *Megaphorura*

- arctica. Sci. Rep.* **2010**, 10, 3047. Doi: 10.1038/s41598-020-60060-z.
166. Stayton, C.T. What does convergent evolution mean? The interpretation of convergence and its implications in the search for limits to evolution. *Interface Focus* **2015**, 5, 20150039. Doi: 10.1098/rsfs.2015.0039.
167. Chen, L.; DeVries, A.L.; Cheng, C.-H.C. Evolution of antifreeze glycoprotein gene from a trypsinogen gene in Antarctic notothenioid fish. *Proc. Natl. Acad. Sci. USA* **1997**, 94, 3811-3816. Doi: 10.1073/pnas.94.8.3811.
168. Chen, L.; DeVries, A.L.; Cheng, C.-H.C. Convergent evolution of antifreeze glycoproteins in Antarctic notothenioid fish and Arctic cod. *Proc. Natl. Acad. Sci. USA* **1997**, 94, 3817-3822. Doi: 10.1073/pnas.94.8.3817.
169. Keeling, P.J.; Palmer, J.D. Horizontal gene transfer in eukaryotic evolution. *Nat. Rev. Genet.* **2008**, 9, 605-618. Doi: 10.1038/nrg2386.
170. Drezen, J.-M.; Josse T.; Bézier A.; Gauthier, J.; Huguet, E.; Herniou, E.A. Impact of lateral transfers on the genomes of Lepidoptera. *Genes* **2017**, 8, 315. Doi: 10.3390/genes8110315.
171. Zakharoc, I.A. Horizontal Gene Transfer into the Genomes of Insects. *Russ. J. Genet.* **2016**, 52, 702-707. Doi: 10.1134/S1022795416070115.
172. Mao, X.; Liu, Z.; Ma, J.; Pang, H.; Zhang, F. Characterization of a novel β -helix antifreeze protein from the desert beetle *Anatolica polita*. *Cryobiology* **2011**, 62, 91-99. Doi: 10.1016/j.cryobiol.2011.01.001.
173. Kondo, H.; Mochizuki, K.; Bayer-Giraldi, M. Multiple binding modes of a moderate ice-binding protein from a polar microalga. *Phys. Chem. Chem. Phys.* **2018**, 20, 25295–25303. Doi: 10.1039/C8CP04727H.
174. Moffiz Uddin Khan, N.M.; Arai, T.; Tsuda, S.; Kondo, H. Characterization of microbial antifreeze protein with intermediate activity suggests that a bound-water network is essential for hyperactivity. *Sci. Rep.* **2021**, 11, 5971. Doi: 10.1038/s41598-021-85559-x.
175. Jones, D.; Sneath, P.H. Genetic transfer and bacterial taxonomy. *Bacteriol Rev* **1970**, 34, 40–81. Doi: 10.1128/br.34.1.40-81.1970.
176. Bayer-Giraldi, M.; Uhlig, C.; John, U.; Mock, T.; Valentin, K. Antifreeze proteins in polar sea ice diatoms: diversity and gene expression in the genus *Fragilariopsis*. *Environ Microbiol* **2010**, 12, 1041–1052. Doi: 10.1111/j.1462-2920.2009.02149.x.
177. Raymond, J.A.; Kim, H.J. Possible role of horizontal gene transfer in the colonization of sea ice by algae. *PLoS ONE* **2012**, 7, e35968. Doi: 10.1371/journal.pone.0035968.
178. Raymond, J.A. The ice-binding proteins of a snow alga, *Chloromonas brevispina*: probable acquisition by horizontal gene transfer. *Extremophiles* **2014**, 18, 987–994. Doi: 10.1007/s00792-014-0668-3.
179. Raymond, J.A.; Morgan-Kiss, R. Separate origins of ice-binding proteins in Antarctic

- Chlamydomonas species. *PLoS ONE* **2013**, 8, e59186. Doi: 10.1371/journal.pone.0059186.
180. Fitzpatrick, D.A. Horizontal gene transfer in fungi. *FEMS Microbiol Lett* **2012**, 329, 1–8.
Doi: 10.1111/j.1574-6968.2011.02465.x.

Acknowledgements

In the first place, I would like to sincerely thank my supervisor, Dr. Sakae Tsuda, for his many kinds, patient, considerate advice, excellent supervision given to me. He has been introduced many things, for example, how to write a paper, make beautiful figures, overcome some difficulties in experiments and so on. He has given me many opportunities to grow up as a scientist for the past four years. He always very kind and shows how researcher should be to us. I would also like to thank Dr. Hidemasa Kondo, for his kind, advice, guidance, perspectives given to me. He has been helped me and given new insight kindly. I owe it to his care that I pursued my experiment comfortably.

I am also very thankful to everybody in the Tsuda lab, past and present. I would like to thank Dr. Yasushi Ohyama, for his advice and discussion based on a physical point of view. I would like to thank Mrs. Ai Miura for her fundamental support and sample preparation for years. I would like to thank Dr. Yuji Sasaki, Dr. Tatsuya Arai and Dr. Yoshiyuki Nishimiya for their advice, discussion and tremendous cooperation. I am also very grateful to all students in this lab for their accompanying, supporting and encouraging.

I couldn't proceed with my research without their generous supports. It has been my pleasure to work and study in this laboratory. Finally, I would like to appreciate very much my family for their understanding and many supports in a student life.